2019

Phosphorus-based anode materials for potassium ion batteries

Wenchao Zhang
University of Wollongong

UNIVERSITY
OF WOLLONGONG
AUSTRALIA

Phosphorus-based anode materials for potassium ion batteries

A thesis submitted for fulfilment of the requirements for the award of the degree

DOCTOR of PHILOSOPHY

From the

UNIVERSITY OF WOLLONGONG

By

Wenchao Zhang, B.Sc., M.Sc.

Institute for Superconducting and Electronic Materials

Australian Institute of Innovative Materials

School of Mechanical, Materials, Mechatronic and Biomedical Engineering

Faculty of Engineering Information and Sciences

University of Wollongong, NSW, Australia

January, 2019

Certificate of Originality

This is to certify that the original work presented in this thesis was carried out by the candidate in the laboratories of the Institute for Superconducting and Electronics Materials (ISEM) and the School of Mechanical, Materials, Mechatronic and Biomedical Engineering, Faculty of Engineering Information and Sciences at the University of Wollongong (UOW), New South Wales (NSW), Australia, and has not been submitted for a degree to any other academic institution for higher education.

Wenchao Zhang

January, 2019

To my family and friends who always stand by me

Acknowledgements

First of all, it is a great pleasure to take this opportunity to express my deepest respect and heartiest gratitude to my principal supervisor, Prof. Zaiping Guo, who encouraged me to start my battery career in the initial stages of my PhD studies. She provided me with her continuous strong support, academic guidance, and valuable encouragement throughout my doctoral course. In addition, her very valuable opinions on carrying out experiments from a strategically advantageous position also gave me great benefits and inspiration. These contributions have helped me tremendously to proceed smoothly with my PhD career and complete this thesis.

I am also grateful to my co-supervisor, Dr. Wei Kong Pang, for his contributions and supervision. He also guided and mentored me in the field of crystallographic and *in-operando* XRD analysis. I am also grateful that I was given initial training on chemistry experiments by Dr. Jianfeng Mao. He taught me how to prepare alloy-based materials, and how to characterize the samples and organize figures for paper publication. Besides, I should thank for the support by Dr. Zhixin Chen, who provided the initial guidance to teach me how to use crystallography knowledge to analysis TEM data. He also gave some useful advice on my paper writing and suggestions on my research career. I also want to express my great gratitude to Prof. Qinghong Wang and Prof. Hongqiang Wang, for their helpful discussions and collaboration in research, providing me with an inspiring academic and excellent working environment. My sincere thanks to Prof. Jian Zhang, Prof. Yuanzhen Chen, Prof. Tengfei Zhou, Prof. Guanglin Xia, Prof. Yang Zheng, Dr. Vitor Sencadas, Prof. Dan Li, Dr. Yajie Liu, Dr. Li Li, Dr. Hong Gao, Dr. Shudi Min,

Miss Qing Zhang, Mr. Junnan Hao, Mr. Shilin Zhang, Mr. Zhibin Wu, Mr. Fuhua Yang, Mr. Zhijie Wang, Miss. Sailin Liu, Miss. Hanna He, and Dr. Christophe Didier, who all gave me a great deal of help during my PhD work. I am also grateful to my close friends in ISEM: Prof. Wenping Sun, Prof. Jiantie Xu, Dr. Yuhai Dou, Dr. Lei Zhang, Dr. Long Ren, Dr. Yu Zhang, Dr. Lijuan Zhang, Dr Yunxiao Wang, Dr. Zhe Hu, Dr. Qiannan Liu, Dr. Weijie Li, Dr. Chao Han, Dr. Chandrasekar Mayandi Subramaniyam, Mr. Binwei Zhang, Miss Jingjing Yu, Mr. Mingzhe Chen, Miss Enhui Wang, Mr. Haipeng Guo, Mr Weihong Lai, Miss Qiuran Yang, Mr. Xiaobo Zheng, and Mr. Peng Li for their support and for sharing happy times with me. I would also like to take this opportunity to give special thanks to Miss Yaping Chen and Mrs Qian Zhou for their precious friendship and their great support during my PhD career.

I would like to thank Prof. Liming Dai for affording me the opportunity to work with him and study in his group at Case Western Reserve University (CWRU). During this period, he gave me strict training on critical thinking, experimental design, and paper writing, which was of great significance for my future research work. I really appreciate this special and valuable experience. I would also like to thank Dr. Chuangang Hu, who gave me great guidance and help during my visit to CWRU. He was always ready to discuss experimental results and gave me useful suggestions and ideas. I received continuous support and encouragement from him. I would like to extend my great thanks to Prof. Dapeng Wu, Prof. Mei Yang, Prof. Yongqin Han, Prof. Guanghui Yue, Dr. Zichun Wang, Dr. Kewei Shu, Dr. Xiaofeng Lin, Mr. Yi Liu, Miss Jianing Guo, Mr. Li Song, Mr. Huawei Huang, Miss Wenjing

Deng, Mr. Shixin Yu, Mr. Xiaoyi Chen, Mr. Jun Zhang, Mr. Linjiong Zhang, and Mrs. Ana Maria B. Honorato for their kind help when I was at CWRU.

I would like to express my sincere thanks to A/Prof. Jiazhao Wang, Dr. Gilberto Casillas-Garcia, Dr. David Mitchell, Dr. Tony Romeo, A/Prof. Germanas Peleckis, Dr. Mitchell Nancarrow, A/Prof. Shulei Chou, Dr. Xun Xu, and Dr. Dongqi Shi for the training on equipment, as well as Mr. Paul Scully, Mrs. Narelle Badger, Mrs. Crystal Mahfouz, and Mrs. Naomi Davies for their administrative support, and Mrs. Joanne George and Dr. Candace Gabelish for procurement and safety related support. I am grateful to Mr. Robert Morgan and Mr. Mathew Davies for providing vital and timely mechanical workshop support on the fabrication of devices. I would also like to express great thanks to Dr. Tania Silver for the revision of my manuscripts and thesis, which also helped myEnglish writing.

Finally, I want to express special thanks to my parents for their great support and encouragement throughout my entire PhD career. They always give me plenty of mental support and stand by me whenever I need them. Without their selfless giving and devotion, I could not have been able to complete my PhD successfully and smoothly. For this reason, I owe my hearty thanks and greatest gratitude for my beloved parents.

Finally, the author is grateful for financial support from a scholarship from the University of Wollongong, a Matching Scholarship and an International Postgraduate Tuition Award, an Australian Research Council Discovery Project (DP170102406), Australian Research Council Future Fellowships (FT150100109, FT160100251), and an Australian Research Council Linkage Infrastructure Equipment & Facilities grant (LE180100141).

Abstract

In the past few decades, with the continuously depletion of fossil fuels, developing renewable energy resources has become increasingly necessary. For industrial applications, energy storage devices are urgently needed for meeting the requirements of large-scale commercialization. Among them, alkaline ion batteries, especially lithium ion batteries (LIBs), have attracted great attentions due to their high energy density and comparable volumetric capacities for a variety of applications such as mobile phones and portable electrical devices. Nevertheless, LIBs seemingly cannot meet the requirements for next-stage applications such as electrical vehicles in the long run due to the high cost of lithium mineral resources. Therefore, developing alternative energy storage devices is quite important for scalable applications. Sodium ion batteries (SIBs) and potassium ion batteries (PIBs) have attracted considerable attention due to the abundant Na and K resources in the Earth's crust. SIBs may have lower energy-density than LIBs, however, due to the relatively high standard hydrogen potential (-2.71 V vs. E^{o}) of Na, which is obstructing their potential application. In contrast, K has a low standard hydrogen potential (-2.93 V vs. E^{o}), close to that of lithium (-3.04 V vs. E^{o}), which makes the PIBs a good candidate for low-cost and high-energy-density systems.

In terms of electrode materials, carbon-based materials possess long-term cycling stability and high rate capability, making them promising anodes. Their low theoretical capacities may still be an obstacle, however, for high-energy-density energy storage devices. Among the candidate anode materials, phosphorus-based

anodes for PIBs are attractive due to their competitively high energy-density compared to carbon-based anodes, based on their high theoretical capacity of 2594 mA h g^{-1} (formation of K_3P). Nevertheless, they have poor electrochemical performance caused by relatively large volume expansion, low electrical conductivity, and severe electrolyte decomposition due to the highly reactive phosphide surface, which hinders their potential applications.

Sn_4P_3/C composite was prepared by a ball-milling method as a novel anode material for PIBs. The electrode delivered a reversible capacity of 384.8 mA h g^{-1} at 50 mA g^{-1} and a good rate capability of 221.9 mA h g^{-1}, even at 1 A g^{-1}. Its electrochemical performance is better than that of any other anode material reported so far for PIBs. It was also found that the Sn_4P_3/C electrode displays a discharge potential plateau of 0.1 V in PIBs, slightly higher than for sodium-ion batteries (0.01 V) and well above the plating potential of K metal. This diminishes the formation of dendrites during cycling, and thus, Sn_4P_3 is a relatively safe anode material, especially for application in large-scale energy storage, where large amounts of electrode materials are used. Furthermore, a possible reaction mechanism for the Sn_4P_3/C composite as PIB anode is proposed.

An avenue to confine tin phosphide in N-doped carbon fibres as anode for PIBs was developed, which could significantly enhance the cycling stability, especially the high rate capability (160.7 mA h g^{-1} after 1000 cycles at 500 mA g^{-1}). The reaction mechanism of Sn_4P_3 as anode for PIBs is proposed based on an *in-operando* synchrotron X-ray diffraction study. A sequential conversion (P to K_3P_{11}, K_3P) and alloying (Sn to KSn) reaction mechanism suggest a synergistic K-storage mechanism,

corresponding to a theoretical capacity of 620 mA h g^{-1}.The influence of potassium salts and electrolyte additive on the potassium dendrite growth and formation of solid electrolyte interphase (SEI) was also studied. Potassium bis(fluorosulfonyl)imide (KFSI) electrolyte more effectively suppresses the dendrite growth in K stripping/plating compared to the potassium hexafluorophosphate (KPF_6) electrolyte, and facilitates the formation of a stable SEI layer, which helps to avoid excessive side-reactions in electrolyte decomposition, thus enhancing the electrode stability. This work provides a feasible approach to overcome the durability bottlenecks of K ion batteries through regulating the dendrite growth and SEI formation. The insight obtained from this work will be of benefit to the design of K ion batteries.

Outstanding long-term cycling stability with high retained potassium storage capacity (213.7 mA h g^{-1} over 2000 cycles) was achieved via the introduction of an alternative KFSI salt and by using a layered compound (GeP_5) with a high phosphorus concentration as anode material. Fourier transform infrared spectroscopic mapping results suggest that KFSI salt helps to form an uniform SEI layer and reduces the side-reactions at the electrode/electrolyte interface, thus enhancing the cycling performance. *In-operando* synchrotron X-ray diffraction analysis has revealed the synergistic reaction mechanisms of the K-P and K-Ge reactions. These findings indicate the enormous potential of phosphorus-based anodes for high-performance potassium ion batteries and can attract broad interest for regulating the SEI layer formation through manipulating the salt chemistry.

All in all, based on this doctoral thesis, high-performance and high-energy-density phosphorus-based anodes for PIBs could be achieved by nanostructural

designing, the use of a carbon matrix, and electrolyte engineering. It is believed, following from this thesis work, which phosphorus-based anode materials would be of great benefit for applications in other alkaline ion batteries for energy storage devices.

Table of Contents

List of Figures

List of Tables

Nomenclature

Abbreviations

ESS	Energy storage system
PIBs	Potassium ion batteries
CE	Coulombic efficiency
CV	Cyclic voltammetry
E^{o}	Standard hydrogen potential
DFT	Density functional theory
PVDF	Polyvinylidene difluoride
EDS	Energy dispersive X-ray spectroscopy
EC	Ethylene carbonate
EIS	Electrochemical impedance spectroscopy
FFT	Fast Fourier Transform
DEC	Diethyl carbonate
PC	Propylene carbonate
EMC	Ethylmethyl carbonate
$NaPF_6$	Sodium hexafluorophosphate
KPF_6	Potassium hexafluorophosphate
KFSI	Potassium bis(fluoroslufonyl)imide
FEC	Fluoroethylene carbonate
GGA	Generalized gradient approximation
DME	Dimethoxyethane

DMF	Dimethylformamide
DI	Deionized
CMC	Carboxymethyl cellulose
PAA	Poly(acrylic acid)
PAN	Polyacrylonitrile
CV	Cyclic voltammetry
HRTEM	High resolution transmission electron microscopy
LIBs	Lithium-ion batteries
CC	Constant current
PBE	Perdew-Burke-Ernzerhof
DNP	Double numerical basis with polarized orbital
SAED	Selected area electron diffraction
SEI	Solid electrolyte interphase
SEM	Scanning electron microscopy
SIBs	Sodium-ion batteries
STEM	Scanning transmission electron microscopy
TEM	Transmission electron microscopy
TGA	Thermogravimetric analysis
XRD	X-ray diffraction
SXRPD	Synchrotron X-ray powder diffraction
MCT	Mercury cadmium tellurium
ATR	Average true range
PCA	Principal component analysis
FTIR	Fourier-transform infrared

TXM	Transmission X-ray microscopy
XPS	X-ray photoelectron spectroscopy
HEBM	High-energy ball-milling

List of Organizations

MMMB	Mechanical, Materials, Mechatronic and Biomedical Engineering
EIS	Engineering and Information Sciences
ISEM	Institute for Superconducting and Electronic Materials
EMC	Electron Microscopy Centre
AIIM	Australian Institute of Innovative Materials
UOW	University of Wollongong
ARC	Australian Research Council
CWRU	Case Western Reserve University
NSRRC	National Synchrotron Radiation Research Center
ANSTO	Australian Nuclear Science and Technology Organisation

Chapter 1
1 Introduction

1.1. Research Background

With the continuous consumption of fossil fuels such as petrol, the associated emissions of pollutants and the limited nature of fossil fuel resources have generated great concerns for future development and environmental problems [1-4]. In recent decades, an abundance of alternative energy systems have been developed, such as wind and solar power, to overcome above the concerns to some extent. They are still limited, however, by natural environmental conditions and the low efficiency of these systems[5]. In 1991, lithium ion batteries (LIBs) were commercialized by the Sony Company and brought in a new paradigm for the energy storage market [6-8]. It is undoubtable that lithium ion batteries (LIBs) have facilitated the rapid development of portable devices such as mobile phones and promoted enormous economy growth during the last nearly 20 years [9-16].

Nevertheless, in terms of the grid-scale applications, the costs of making a successful battery are considered to be the first priority for the long run [17-19]. In view of this, sodium and potassium, from the same group as lithium, have deserved tstudy for sodium ion batteries (SIBs) and potassium ion batteries (PIBs)[20]. Owing to the big benefits of the abundant resources of sodium and potassium in the Earths' crust (2.3 wt. % and 1.8 wt. %, respectively), SIBs and PIBs could have competitive prices compared to LIBs due to the rarity of lithium in the Earths' crust (0.0017 wt. %)[21]. In

addition, the energy density should also be taken into consideration for the development of electrical vehicles. As is well known, lithium has the lowest standard hydrogen potential (-3.04 V vs. E^o), which will lead its potentially having the highest energy density among all the alkaline ion batteries. Although great efforts have been made on the study of SIBs, their low energy density due to the high standard hydrogen potential (-2.71 V vs. E^o) has impeded their future applications. Since potassium has a similar standard hydrogen potential (-2.93 V vs. E^o) to lithium, PIBs could have higher energy density than SIBs[22-27].

Therefore, it is meaningful to develop suitable electrode materials towards the practical application of PIBs. In 2004, the first potassium secondary half-cell was designed by Ali Eftekhari based on Prussian blue cathode, which could deliver reasonable cycling performance[28]. After that, researchers barely studied PIBs, due to their difficult operating conditions and obscure reaction mechanisms. In contrast, the researchers focused on studies of various electrode materials for SIBs. Unfortunately, as graphite is the regular commercial anode material for LIBs, graphite anode was shown to only be capable of reacting with sodium to form NaC_{64}, which has very limited capacity and low energy density [29-31]. Staggering advances on PIBs have emerged since 2015, however, when Ji et al [32] and Hu et al. [33] demonstrated the possibility of potassiation into commercial graphite to form KC_8 compound, which has a high theoretical capacity of 279 mA h g^{-1}. Since then, there has been an abundance of research work focused on designing carbon-based electrode materials

for PIBs, which have achieved promising electrochemical performance. In spite of their ultra-long cycling performance and high rate capability, practical applications for PIBs are still hindered by their low capacity due to the large pseudocapacitance and the limited theoretical capacity offered by the reaction of KC_8. On the basis of the research history of LIBs and SIBs, alloy-based electrode materials deserved to be considered for development due to the high theoretical capacity of elements such as Sn[34-37], Sb [38-40], Si[41-42], P[43], and their derived alloy compounds. Among them, P could react with Li, Na, and K to form Li_3P[43], Na_3P[44-46], and K_3P[47-49], respectively, to offer the high theoretical capacity (2596 mA g^{-1}), which have attracted great interest in the past few years. Nevertheless, the large volume variations during cycling, low electrical conductivity of red phosphorus, and unstable interface due to the formation of phosphides are hindering their developments [50-51].

1.2. Objectives of the Research

Herein, in this thesis, two kinds of phosphorus-based materials (Sn_4P_3 and GeP_5) were prepared for exploration as potential anodes for high-performance PIBs. Furthermore, to improve their electrochemical performance, alternative electrolyte-systems were also studied. In addition, PIBs are relatively new systems compared to LIBs and SIBs, so an understanding of the reaction mechanisms is needed to help understand the discharge/charge products and the corresponding volume expansions. As a key component in the battery, the solid electrolyte interphase (SEI) layer is essential to

help increase the cycle life and improve the interfacial kinetics, and suitable characterization techniques needed to be applied to study this interface. As a result, high-performance phosphorus-based anodes for PIBs were obtained in this doctoral work, and the relevant SEI layer, electrolyte effects, and reaction mechanism were subjected to systematic studies. This doctoral thesis could provides a comprehensive understanding of phosphorus-based anode materials for PIBs and offer a feasible approach to overcome the durability bottlenecks of K-ion batteries through regulating dendrite growth and SEI formation.

1.3. Thesis Structure

For the purpose of developing a scalable way to fabricate phosphorus-based compounds that could be used as anode for PIBs, the ball-milling method and electrospinning method were applied in order to produce pure phases. The electrochemical reaction mechanism was also investigated by ex-situ and *in-operando* methods. Moreover, in order to optimize the electrochemical performance, an alternative potassium salt was introduced and studied for its effects on the solid electrolyte interphase (SEI) layer. The structure of this thesis work is briefly outlined as follows:

Chapter 1 introduces the research background for PIBs in the energy storage field and explains the importance and significance of this work.

Chapter 2 presents a literature review on recent progress on anode materials and electrolyte engineering for PIBs.

Chapter 3 presents the detailed preparation methods, as well as the structural and electrochemical characterization techniques used in this thesis work.

Chapter 4 investigates Sn_4P_3/C composite as a novel anode material for PIBs and explores the possible reaction mechanisms of the Sn_4P_3/C composite as PIB anode.

Chapter 5 discusses the confinement of Sn_4P_3 in nitrogen-doped carbon fibres as anode for PIBs to improve the cycling performance, with the further involvement of *in-operando* X-ray diffraction to reveal synergistic K-storage mechanisms. By using potassium bis(fluorosulfonyl)imide (KFSI) salt, dendrite growth in K stripping/plating could be suppressed, and the solid-electrolyte interphase (SEI) layer could be stabilized, thus enhancing the electrode stability.

Chapter 6 is devoted to a layered compound (GeP_5) with a high phosphorus concentration as anode material for PIBs. Fourier transform infrared spectroscopic mapping was introduced to further study the effect of KFSI salt. *In-operando* synchrotron X-ray diffraction analysis has revealed the synergistic reaction mechanisms of the K-P and K-Ge reactions.

Chapter 7 summarizes the work in this thesis and provides some prospects for developing high-performance phosphorus-based anode materials for PIBs.

1.4. References

[1] M. Armand, J.-M. Tarascon, *Nature* **2008**, 451, 652.

[2] D. Larcher, J.-M. Tarascon, *Nat. Chem.* **2015**, 7, 19.

[3] B. Dunn, H. Kamath, J.-M. Tarascon, *Science* **2011**, 334, 928.

[4] H. Chen, T. N. Cong, W. Yang, C. Tan, Y. Li, Y. Ding, *Progress in Natural Science* **2009**, 19, 291.

[5] H. Sun, Y. Zhang, J. Zhang, X. Sun, H. Peng, *Nature Reviews Materials* **2017**, 2, 17023.

[6] P. G. Bruce, S. A. Freunberger, L. J. Hardwick, J.-M. Tarascon, *Nat. Mater.* **2012**, 11, 19.

[7] G. Ceder, *MRS Bulletin* **2010**, 35, 693.

[8] J.-M. Tarascon, M. Armand, in *Materials For Sustainable Energy: A Collection of Peer-Reviewed Research and Review Articles from Nature Publishing Group*, World Scientific **2011**, p. 171. Edited by Dusastre, Vincent. Published by Macmillan Publishers Ltd, London.

[9] M. Park, J. Ryu, W. Wang, J. Cho, *Nature Reviews Materials* **2017**, 2, 16080.

[10] N. Nitta, F. Wu, J. T. Lee, G. Yushin, *Materials Today* **2015**, 18, 252.

[11] D. Yang, H. Ren, D. Wu, W. Zhang, X. Lou, D. Wang, K. Cao, Z. Gao, F. Xu, K. Jiang. *Journal of colloid and interface science* **2019**, 542, 81.

[12] L. Lu, X. Han, J. Li, J. Hua, M. Ouyang, *J. Power Sources* **2013**, 226, 272.

[13] P. Poizot, S. Laruelle, S. Grugeon, L. Dupont, J. Tarascon, *Nature* **2000**, 407, 496.

[14] Y. Liu, Y.-K. Tzeng, D. Lin, A. Pei, H. Lu, N. A. Melosh, Z.-X. Shen, S. Chu, Y. Cui, *Joule* **2018**, 2, 1595.

[15] D. Lin, Y. Liu, Y. Cui, *Nat. Nanotechnol.* **2017**, 12, 194.

[16] D. Wu, Y. Wang, N. Ma, K. Cao, W. Zhang, J. Chen, D. Wang, Z. Gao, F. Xu, K. Jiang. *Electrochimica Acta*. **2019**, 305, 474.

[17] M. D. Slater, D. Kim, E. Lee, C. S. Johnson, *Adv. Funct. Mater.* **2013**, 23, 947.

[18] S. W. Kim, D. H. Seo, X. Ma, G. Ceder, K. Kang, *Adv. Energy Mater.* **2012**, 2, 710.

[19] B. L. Ellis, L. F. Nazar, *Current Opinion in Solid State and Materials Science* **2012**, 16, 168.

[20] J. W. Choi, D. Aurbach, *Nature Reviews Materials* **2016**, 1, 16013.

[21] J. C. Pramudita, D. Sehrawat, D. Goonetilleke, N. Sharma, *Adv. Energy Mater.* **2017**.

[22] I. Sultana, M. M. Rahman, Y. Chen, A. M. Glushenkov, *Adv. Funct. Mater.* **2018**, 28, 1703857.

[23] X. Wu, D. P. Leonard, X. Ji, *Chem. Mater.* **2017**, 29, 5031.

[24] Q. Zhang, Z. Wang, S. Zhang, T. Zhou, J. Mao, Z. Guo, *Electrochemical Energy Reviews* **2018**, 1,625

[25] K. Kubota, M. Dahbi, T. Hosaka, S. Kumakura, S. Komaba, *Chem. Rec.* **2018**, 18, 459.

[26] H. Kim, J. C. Kim, M. Bianchini, D. H. Seo, J. Rodriguez‐Garcia, G. Ceder, *Adv. Energy Mater.* **2018**, 8, 1702384.

[27] A. Eftekhari, Z. Jian, X. Ji, *ACS Appl. Mater. Interfaces* **2016**, 9, 4404.

[28] A. Eftekhari, *J. Power Sources* **2004**, 126, 221.

[29] W. Zhang, Y. Liu, Z. Guo, *Sci. Adv.* **2019**, 5, eaav7412.

[30] K. Beltrop, S. Beuker, A. Heckmann, M. Winter, T. Placke, *Energy Environ. Sci.* **2017**, 10, 2090.

[31] P. Ge, M. Fouletier, *Solid State Ionics* **1988**, 28, 1172.

[32] Z. Jian, W. Luo, X. Ji, *Journal of the American Chemical Society* **2015**, 137, 11566.

[33] W. Luo, J. Wan, B. Ozdemir, W. Bao, Y. Chen, J. Dai, H. Lin, Y. Xu, F. Gu, V. Barone, *Nano Lett.* **2015**, 15, 7671.

[34] W. Zhang, J. Mao, W. K. Pang, Z. Guo, Z. Chen, *Electrochim. Acta* **2017**, 235, 107.

[35] G. Derrien, J. Hassoun, S. Panero, B. Scrosati, *Adv. Mater.* **2007**, 19, 2336.

[36] Y. Liu, N. Zhang, L. Jiao, Z. Tao, J. Chen, *Adv. Funct. Mater.* **2015**, 25, 214.

[37] Y. Xu, Y. Zhu, Y. Liu, C. Wang, *Adv. Energy Mater.* **2013**, 3, 128.

[38] W. Zhang, J. Mao, W. K. Pang, X. Wang, Z. Guo, *Nano Energy* **2018**, 49, 549.

[39] W. D. McCulloch, X. Ren, M. Yu, Z. Huang, Y. Wu, *ACS Appl. Mater. Interfaces* **2015**, 7, 26158.

[40] Y. Zhu, X. Han, Y. Xu, Y. Liu, S. Zheng, K. Xu, L. Hu, C. Wang, *ACS Nano* **2013**, 7, 6378.

[41] U. Kasavajjula, C. Wang, A. J. Appleby, *J. Power Sources* **2007**, 163, 1003.

[42] Y. Liu, Z. Tai, T. Zhou, V. Sencadas, J. Zhang, L. Zhang, K. Konstantinov, Z. Guo, H. K. Liu, *Adv. Mater.* **2017**, 29, 1703028.

[43] L. Wang, X. He, J. Li, W. Sun, J. Gao, J. Guo, C. Jiang, *Angew. Chem.* **2012**, 124, 9168.

[44] J. Sun, H.-W. Lee, M. Pasta, H. Yuan, G. Zheng, Y. Sun, Y. Li, Y. Cui, *Nat. Nanotechnol.* **2015**, 10, 980.

[45] T. Ramireddy, T. Xing, M. M. Rahman, Y. Chen, Q. Dutercq, D. Gunzelmann, A. M. Glushenkov, *Journal of Materials Chemistry A* **2015**, 3, 5572.

[46] Y. Zhu, Y. Wen, X. Fan, T. Gao, F. Han, C. Luo, S.-C. Liou, C. Wang, *ACS Nano* **2015**, 9, 3254.

[47] W. Zhang, Z. Wu, J. Zhang, G. Liu, N.-H. Yang, R.-S. Liu, W. K. Pang, W. Li, Z. Guo, *Nano Energy* **2018**, 53, 967.

[48] W. Zhang, W. K. Pang, V. Sencadas, Z. Guo, *Joule* **2018**, 2, 1534.

[49] W. Zhang, J. Mao, S. Li, Z. Chen, Z. Guo, *J. Am. Chem. Soc.* **2017**, 139, 3316.

[50] Q. Wang, X. Zhao, C. Ni, H. Tian, J. Li, Z. Zhang, S. X. Mao, J. Wang, Y. Xu, *J. Phys. Chem. C* **2017**, 121, 12652.

[51] T. Ramireddy, R. Kali, M. K. Jangid, V. Srihari, H. K. Poswal, A. Mukhopadhyay, *J. Electrochem. Soc.* **2017**, 164, A2360.

Chapter 2

2.1 Introduction of PIBs

Potassium ion batteries (PIBs) first emerged in 2004 [1] and have attracted wide attentions since 2015 [2-4]. Since potassium belongs to the same group as lithium and sodium, PIBs possess some similar physicochemical properties and reaction mechanisms to lithium ion and sodium ion batteries (LIBs and SIBs)[5-6]. Hence, it is reasonable to introduce the electrode materials accepted for LIBs and SIBs into this new system. In addition to the consideration of low cost as their big benefit, similar to SIBs, PIBs could have great potential to be developed as a higher energy-density system than that of SIBs due to the lower standard hydrogen potential (-2.93 V vs. E^o) of potassium compared to that (-2.71 V vs. E^o) of sodium[7-9].

These considerations have promoted the study of PIBs, not only because of their high energy density and low cost, but also due to the fast transportation of K^+ in electrolyte. Potassium has the largest atomic radius (1.38 Å) compared to lithium (0.68 Å) and sodium (0.97 Å), but K^+ in propylene carbonate (PC) solvents has the smallest Stokes' radius (3.6 Å) compared to Li^+ (4.8 Å) and Na^+ (4.6 Å)[5]. Therefore, K^+ could have the fastest ionic mobility and conductivity in organic-based electrolyte. Inspired by this unique property, density functional theory (DFT) calculations were employed to demonstrate that K^+ has the highest diffusion coefficient in ethylene carbonate (EC) electrolyte when compared to Li^+ and Na^+ [10].

The above-mentioned three advantages of PIBs offer huge opportunities for researchers to develop suitable electrode materials and architectures for K ion insertion/extraction. In past years, especially in the last three year, PIBs have scored astounding achievements in terms of electrode materials, electrolyte optimization, electrode design, and advanced devices related to potassium ion storage. As for the anode materials, carbon-based [11-34], sulphur-based [32, 35-50], and alloy-based materials[43, 51-67] have been successfully applied in this system, which has achieved long-term cycling stability and high-rate capability. In terms of electrolytes, various potassium-ion containing salts and organic solvents have been applied and systematically studied. In consideration of functional binders, commonly used binders in LIBs and SIBs, such as polyvinylidene difluoride (PVDF) and carboxymethyl cellulose (CMC), were extended to the research on PIBs. The separator is also important for the stability of the cell, not only because it serves as a medium for the transportation of K^+, but also to avoid dendrite penetration into the separator, thus causing short-circuits.

In the past three years, the growing research effort on PIBs has generally targeted the exploration of suitable electrode materials and electrolyte optimization to improve the electrochemical performance. To provide a possible road map to help design electrode materials for next-generation high-performance PIBs, it is necessary to get a better understanding of the challenges of PIBs.

2.2 Challenges of PIBs

The practical development of PIBs is hindered by not only similar issues to LIBs and SIBs, but also the newly arisen concerns due to the large atomic size of K and the relatively active surface of the K metal. Generally, the main issues could be summarized as follows:

1) **Large volume variations during cycling.** Due to the largest atomic size of the K^+ compared to Li^+ and Na^+, the electrode would suffer huge volume variations during cycling. For example, graphite as the commercial anode for LIBs exhibits a volume expansion of around 10 % during the full discharge process. In terms of graphite as anode for PIBs, over 60 % volume expansion will be achieved after the discharge process[68]. As promising high-energy-density anodes, alloy-based materials possess high theoretical capacity but undergo huge volume expansions. For instance, the conventional Sn_4P_3 anode undergoes over 680 % volume expansion during the potassiation process[53]. The volume expansion would cause a series of problems as arising from the stress that is induced and released. As is well known, the stress concentration would cause electrode pulverization, thus causing the active materials to peel off from the current collector.
2) **Sluggish reaction kinetics.** Although potassium ions possess the smallest Stoke's radius compared to lithium and sodium ions, which might give it the fastest ionic transportation in electrolyte, the large atomic size of K would still induce serious problems relating to its chemical diffusivity in solids and the sluggish diffusion

coefficient along the SEI layer[51]. The rate capability is not only individually dependent on the ionic diffusion coefficient in electrolyte, but also on the diffusion process in solid materials. As is commonly known, the rate is controlled and decided by this relatively slow step. Therefore, developing nanostructured electrode materials is essential to help improve the reaction kinetics.

3) **Severe electrolyte reduction and metal dendrites.** Electrolyte decomposition is always the main concern that limits the cycle life. When the cell goes through electrochemical discharge/charge processes, the electrolyte decomposition generally comes from electrolyte reduction and the consumption of electrolyte in the SEI layer formation. In general, the electrolyte reduction takes place under the reduction potential of different solvents, which are limited by both thermodynamic and kinetic processes. In addition, the consumption of the electrolyte is necessary to form SEI layers on the anode and cathode sides. Under continuous electrochemical cycling, the SEI layer is not only generated at the initial cycle, but also forms during the following cycles due to the newly created interface caused by electrode pulverization and the by-products of electrolyte decomposition. On the other hand, restricting dendrite growth is one of the main research objectives as is true for lithium metal[69]. K is considered to be more reactive than lithium[70]. Hence, K dendrite growth must be taken into consideration based on the research on half-cells and other extended K-S and K-O_2 systems[71-75]. The newly involved interface caused by the dendrite formation

will increase consumption of the electrolyte, thus drying up the electrolyte and boosting the polarization.

The above-mentioned issues should be considered together to aim for high-performance PIBs. During cycling, the large volume expansions may lead to some electrode pulverization, thus further generating cracks and new interfaces. These newly created interfaces are generally chemically inactive and insulated, which will be great obstacles for electron and ion transportation and limit the reaction kinetics. In addition to this, SEI layers would be likely to be form on these newly created interfaces, thus increasing the consumption of electrolyte and stimulating the side reactions, which will decrease the coulombic efficiency during cycling. Meanwhile, the severe growth of K metal dendrites could also be linked to the consumption of electrolyte. All in all, it is essential to develop certain strategies to address the above-mentioned problems and optimize the electrochemical performance of PIBs.

2.3 Anode materials

As one of the key components in PIB cells, high-energy-density anode materials must be developed due to requirements for high specific capacity and low operating voltage. Nowadays, considerable research has focused on studies of carbon-based, sulphur-based, metal oxide-based, and phosphorus-based anode materials, achieving attractive results. Therefore, it is meaningful to summarize the research outcomes in this literature review.

2.3.1 Carbon-based materials

For state-of-the-art rechargeable alkaline ion batteries, carbon-based materials are the most promising anodes due to their high electrical conductivity, low cost, easy modification, and competitive rate performance. Graphite, as the most successful anode materials applied in commercial LIBs, can offer relatively high theoretical capacity (372 mA h g^{-1}) and reasonable cycling stability[76]. Nevertheless, graphite cannot be directly used as anode for SIBs due to the low theoretical capacity arising from the formation of NaC_{64}, whichis limited by thermodynamic considerations[77]. Interestingly, graphite can be directly used as anode for PIBs because it can react with potassium to form KC_8 (Figure 2.1)[2], which possess high theoretical capacity of 279 mA h g^{-1}. The large volume expansion of fully potassiated graphite (61%), however, obviously leads to the severe electrode pulverization. As a result, after only 50 cycles, the graphite electrode delivers very low capacity.

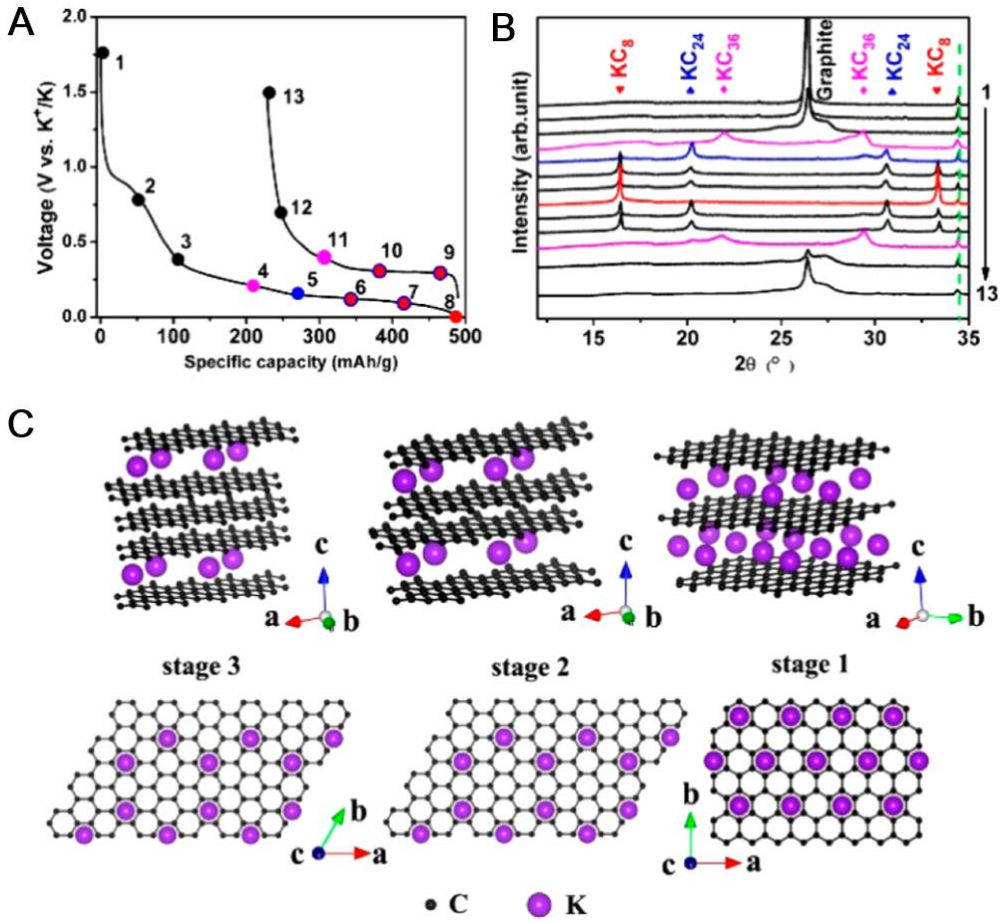

Figure 2.1 (A) The initial cycle of graphite electrode at around 28 mA g^{-1}. (B) X-ray diffraction (XRD) patterns collected at the corresponding points in A. (C) Structure diagrams of different potassium-graphite intercalation compounds, side view (top row) and top view (bottom row)[2].

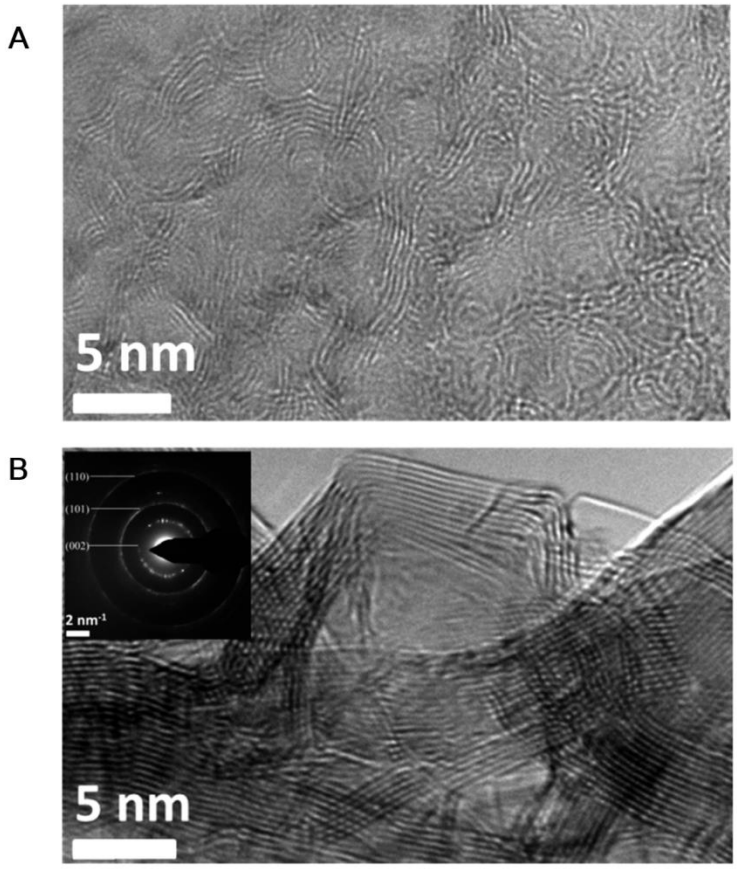

Figure 2.2. High resolution transmission electron microscope (HRTEM) images of (A) nanoporous graphenic carbon (NG) and (B) polynanocrystalline graphite (PG). Inset of B is the selected area electron diffraction (SAED) pattern of PG[78].

To address this problem, polynanocrystalline graphite was prepared because this special structure could maintain its structure of short-range ordered carbon and long-range disordered carbon to enhance the cycling stability (Figure 2.2)[78]. After the researchers optimized the experimental conditions, the optimized electrode could deliver stable cycling performance. Inspired by the expanded graphite used as anode for LIBs and SIBs, it was meaningful to adopt this strategy to accommodate K ions

because K^+ has the largest atomic size[79]. Expanded graphite with a 0.358 nm interplane distance was found to deliver K^+ ions seven times faster than commercial graphite[80]. The volume expansion of the graphite electrode is the main issue that causes capacity fading. Hence, it is essential to develop a stable structure for anode materials with highly graphitic features to accommodate the severe volume expansion. Several pioneering works have been reported on various morphologies. Metal-organic frameworks (MOFs) are widely used as the precursors due to the controllable nature of these structures[81]. Xu et al. used zeolitic imidazolate frameworks (ZIFs) as the precursors to prepare N-doped carbon nanotubes, which could delivered high rate capability of 102 mA h g^{-1} at 2 A g^{-1} and stable cycling performance for 500 cycles with no obvious capacity loss[82]. Hollow structures are also good candidates to accommodate the volume expansion during cycling. In view of this, Cao et al. fabricated hollow carbon nanospheres for K ion storage, which enabled good cycling performance and high capacity retention at a relatively high rate. As shown in Figure 2.3, a high reversible capacity of around 300 mA h g^{-1} at 0.1 C (1 C = 280 mA g^{-1}) and a high capacity of around 210 mA h g^{-1} at 2 C were achieved [83]. From engineering compositional inhomogeneity into single nanoparticles, it was realized that the nanoparticles might be likely to form a platform enabling complicated carbon architectures. In addition to considering high-power potassium ion storage capability, uniform cage-like graphitic carbon was designed to alleviate the volume variations

and induced stress, resulting in very high rate capability, even at around 10000 mA g^{-1} [84].

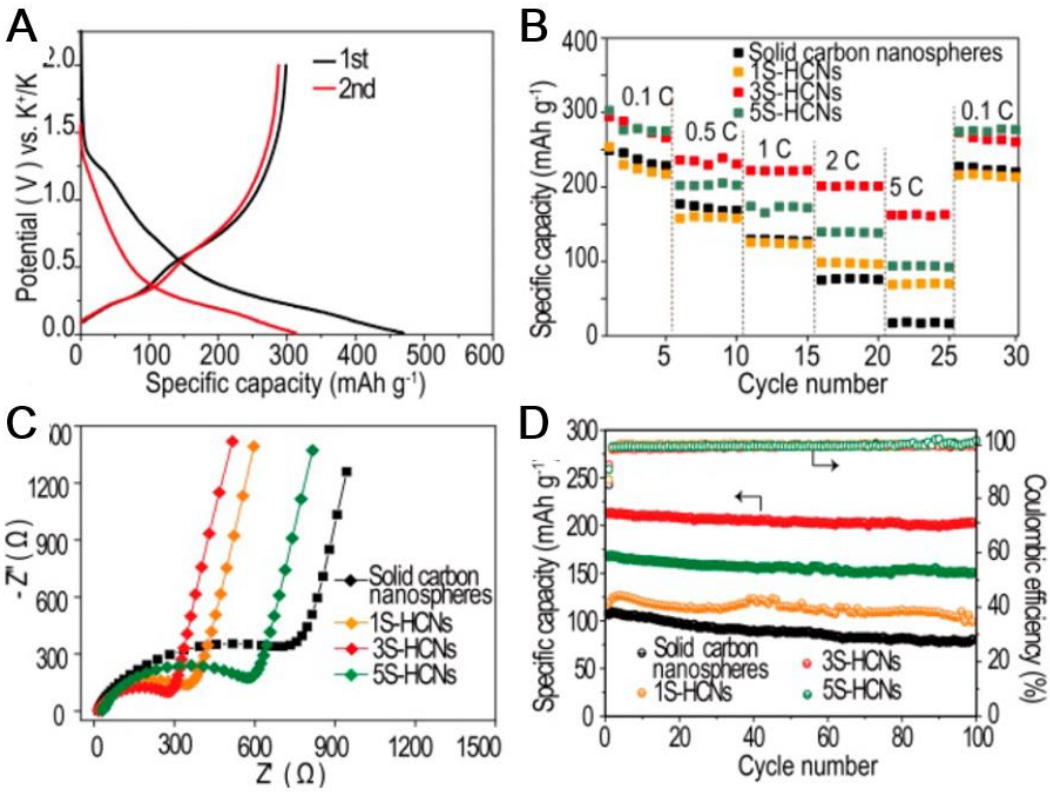

Figure 2.3. (A) Discharge/charge profiles for the hollow carbon nanospheres (HCN) in the first and second cycles at 0.1 C; (B) rate performance for the HCN; (C) electrochemical impedance spectra; and (D) cycling performance of the HCN prepared under various experimental conditions at 2 C[83].

Secondly, it is necessary to develop hard carbon and soft carbon due to their amorphous feature, which allowconsiderable volume variations during cycling. In the early research of Ji et al, their soft carbon electrode clearly revealed good cycling stability and rate capability. Due to the random alignment of graphene layers, hard carbon may offer great porosity for the storage of potassium ions. In comparison, soft carbon with its amorphous feature and low density could also have promising cycling stability and rate performance. Inspired by this, Ji et al. designed electrodes from hard carbon, soft carbon, and their derived composites as anode, which delivered long cycling performance and higher rate performance in PIBs than in SIBs. Through combining the merits of hard carbon and soft carbon, the composite electrodes could exhibit a high reversible capacity with stable cycling, even after 200 cycles.

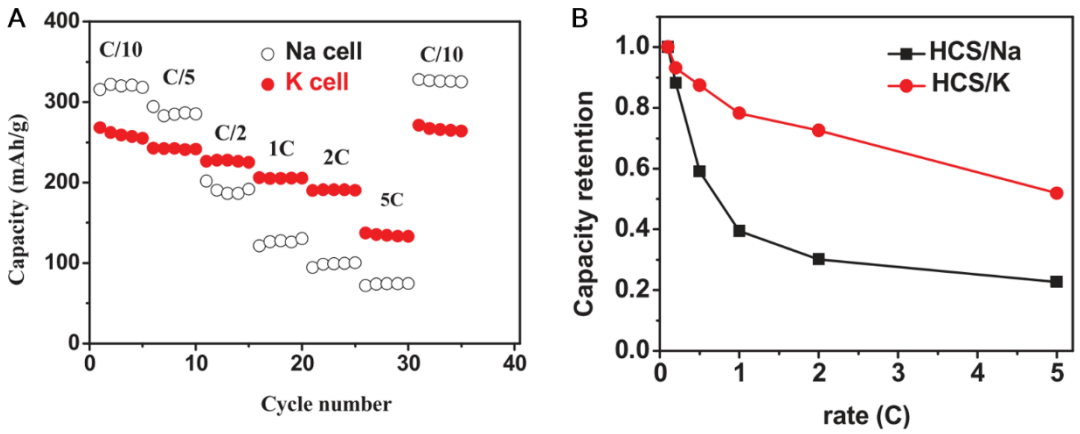

Figure 2.4. (A) Rate performance of hard carbon spheres (HCS)/K and HCS/Na cells. (B) The calculated capacity retention at various current rates for HCS/K and HCS/Na cells[85].

Specifically, in terms of hard carbon spheres, the rate capability of the PIB electrode was around 52% higher than for the SIB (23 %), as shown in Figure 2.4 [85]. In addition, the relatively high potassiated potential above 0.2 V could reduce the risks of K-metal dendrite formation. The rate capability is still not satisfactory, however, due to the limited potassium diffusion kinetics. Recently, their surface-driven storage and capacitance behaviour offered the opportunity to develop high-rate electrodes. The fast storage capability is due to the surface reaction unlike the insertion/deinsertion processes. As the same time, this surface storage could allow fast ion transportations without morphology changes during cycling. Xie et al. prepared Nitrogen-doped hard carbon microspheres as anode for PIBs. Based on simple experimental conditions, this hierarchically porous hard carbon material could be synthesized on a large scale, which is favourable for the development of low-cost PIBs. In addition to the uniform structure of microspheres, their high N-doping level was demonstrated by X-ray photoelectron spectroscopy (XPS) studies, which is of benefit for electron transportation [86].

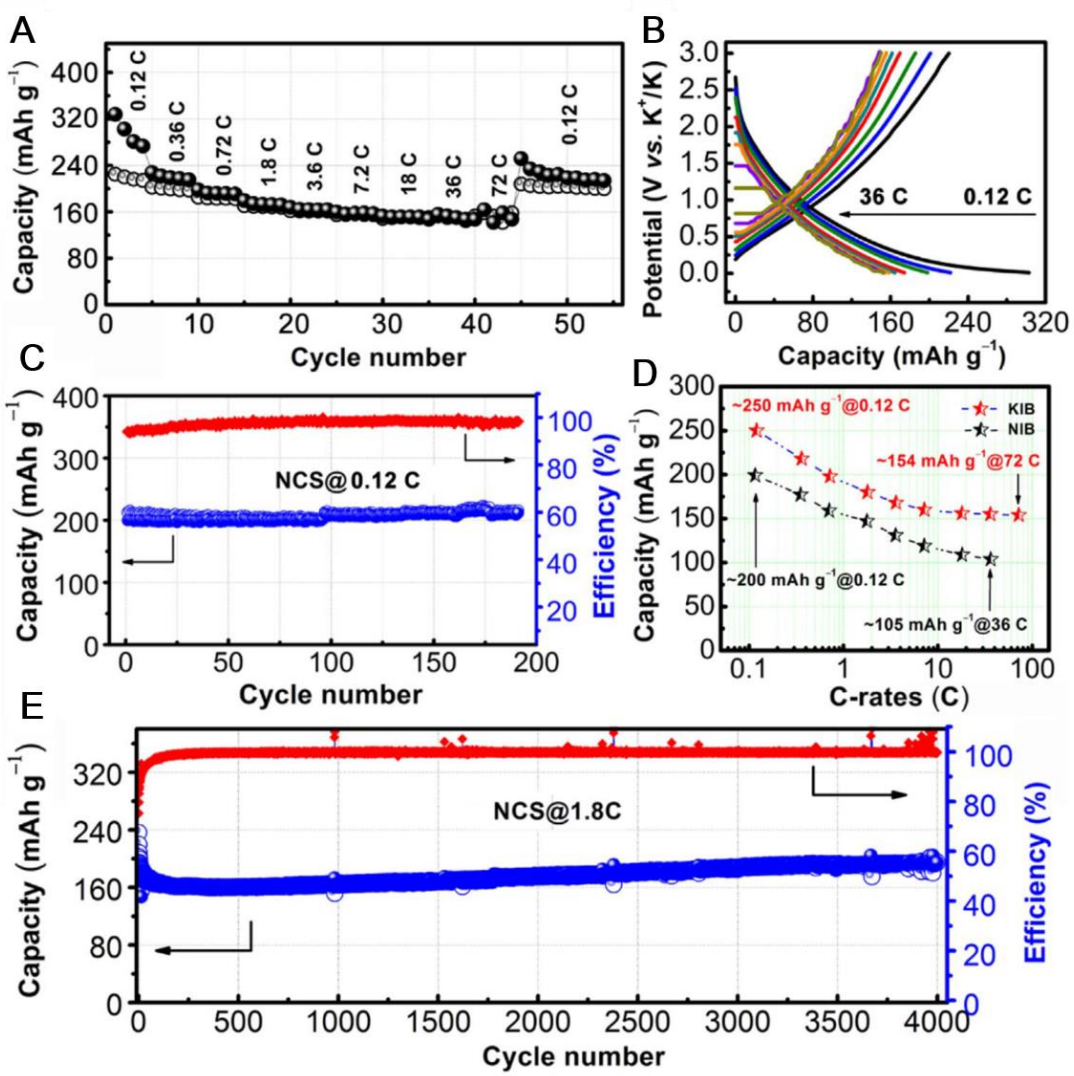

Figure 2.5. (A) Rate performance of nitrogen-rich carbon spheres (NCS) with increasing current; (B) The corresponding discharge/charge curves at various current rates; (C) Cycling performance of the NCS electrode at 0.12 C; (D) Capacity-current density profiles compared with SIB performance of the NCS electrode; (E) Long-term cycling performance of the NCS electrode at 1.8 C for PIBs[86].

As a result, the electrochemical potassium storage performance of the nitrogen-rich carbon spheres (NCS) exhibited a high rate capability of 156 mA h g^{-1} at 18 C (1 C = 280 mA g^{-1}) and ultra-long cycling performance (180 mA h g^{-1} over 4000 cycles), as shown in Figure 2.5. According to a kinetic analysis based on the cyclic voltammetry (CV) results, the charge storage behaviours basically relied on the surface-driven process. This electrode with its fast ionic transportation offers new insight to develop fast charge/discharge potassium ion storage devices.

In terms of soft carbon with its highly amorphous structure, to further improve the cycling stability of carbon-based materials, the amorphous-feature materials such as carbon fibres ought to be explored. Relying on the psedocapacitance reaction mechanism of ion absorption and de-absorption between anode and cathode, nanosized carbon fibres were designed through the electrospinning technique with relatively uniform diameters of around 30-40 nm, as shown in Figure 2.6 [87].

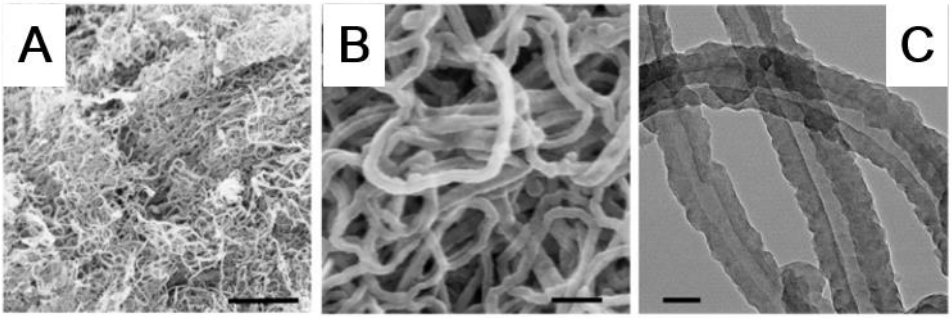

Figure 2.6. Characterizations of N-doped carbon nanofibers (NCNFs). (A, B) Scanning electron microscope (SEM) and (C) TEM images of NCNF[87].

As a result, the carbon electrode could deliver ultra-stable cycling performance (146 mA h g^{-1} at 2 A g^{-1} after 4000 cycles) and rate capability (101 mA h g^{-1} at 20 A g^{-1}). Furthermore, inspired by the large surface area of porous carbon, N-doped porous carbon[27] and ordered mesoporous carbon[88] were also prepared via a facile synthesis method, which delivered long-term cycling stability, although the majority of the capacity contribution was above 0.5 V.

The above mentioned research outcomes offer great opportunity to develop carbon-based anode materials for long-life and high-power potassium ion storage devices. In the next stage, the focus should be on exploring various materials conducive to high-energy-density outputs.

2.3.2 Alloy-based anode materials

Although carbon electrodes deliver long-term cycling stability and high rate capability, they still could not meet the requirements of future high-energy-density devices such as electric vehicles. Therefore, robust anode materials with high specific capacity and long cycle life urgently need to be developed for next-generation high-energy-density applications. It has been demonstrated that Group IVA and VA metals have the potential capability to store X^+ ions (X = Li, Na, and K) by forming MX (M = Metal) alloy compounds[89-90]. For instance, Sn can alloy with Li to form $Li_{22}Sn_5$ [91]and react with Na to form $Na_{15}Sn_4$, respectively. In addition to Sn, phosphorus-based anodes could alloy with X to form X_3P, which has a high theoretical capacity of 2596 mA h g^{-1} and is potentially the highest capacity anode among all the reported electrodes[92].

Despite their high theoretical capacity, the major concern about them is the volume variations during cycling, which would lead to electrode pulverizations and capacity fading[93]. To date, numerous strategies have been employed to address this challenge and notable progress has been achieved on the alloy-based anodes for PIBs.

Silicon is one of the most promising candidates as anode for LIBs due to its very high theoretical capacity (4200 mA h g^{-1}), which is achieved by forming $Li_{4.4}$ Si. In addition, silicon is a well-known earth-abundant element similar to the carbon[94]. As the key element that could act as an alternative anode material to graphite for LIBs, ongoing efforts have been made to develop it, such as by preparing Si/C composites and suitable binders to alleviate the volume expansion. In the case of PIBs, it is promising to study Si as anode due to the thermodynamic prediction of the formation of KSi with a high theoretical capacity of around 950 mA h g^{-1}. Nevertheless, Sultana et al. have tried to employ Si-graphene as anode for PIBs, and it was demonstrated that this composite electrode could only deliver a specific capacity of around 100 mA h g^{-1} at the current density of 50 mA g^{-1} [89]. This leading research may provide evidence of the inert nature of Si alloyed with potassium.

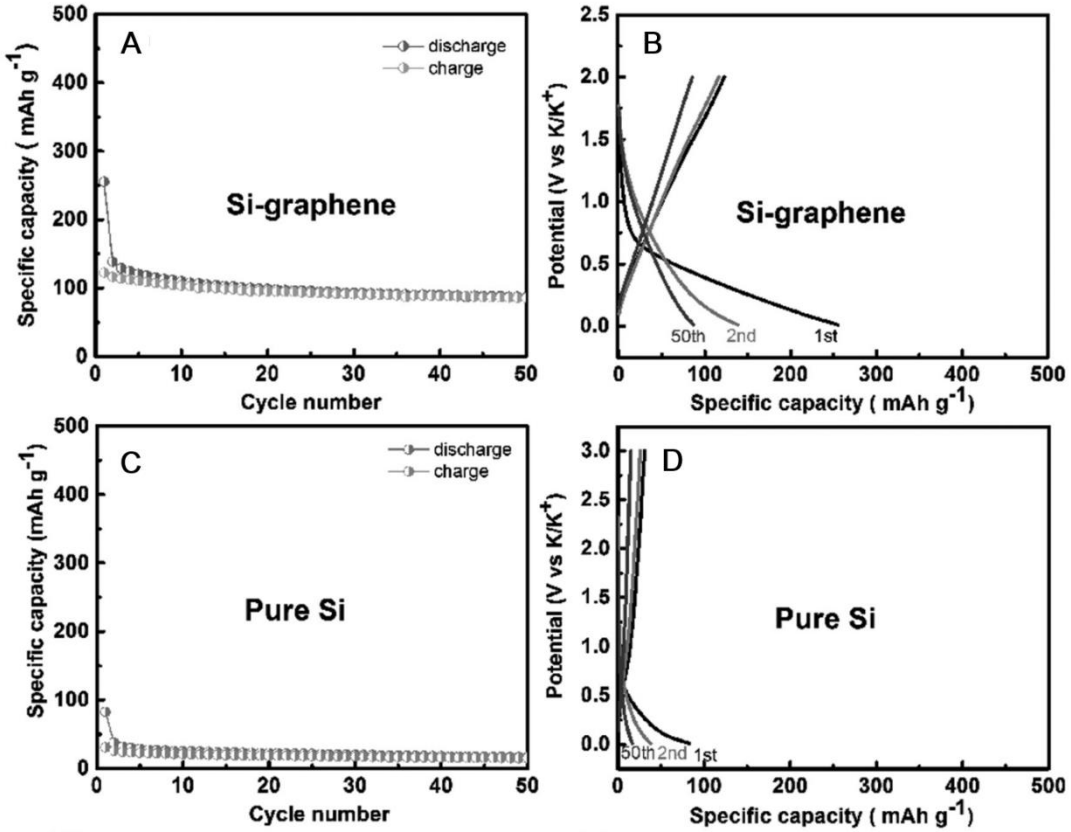

Figure 2.7. A) Cycling performance of Si-graphene anode for PIBs at the current density of 50 mA g^{-1} and B) the corresponding discharge/charge profiles for selected cycles; C) The cycling performance of pure Si anode for PIBs at the current density of 50 mA g^{-1} and D) the corresponding discharge/charge profiles[89].

Bismuth as a proposed high theoretical capacity anode has been well studied for LIBs [95] and SIBs [96]. Although various reaction mechanisms of Bi as anode for SIBs were proposed by the different research groups, its fast ionic transportation enables high rate capability due to the favourable active sites of its unique structure, inspiring many researchers to study this electrode material. On moving to the study of PIBs[60], the

reaction mechanism of Bi anode for PIBs could be evaluated by ex-situ XRD measurements during cycling (Figure 2.8)[97]. As shown in Figure 2.8B, in the first stage, there is a solid-solution reaction that occurs initially with the reaction of K and Bi to form K-Bi alloy solid phases. In the following discharge process, the intercalation of K, unlike the mechanism in SIBs, could take place between the Bi layers due to the R-3m structure. The two-phase reaction stages suggest that K_5Bi_4 and K_3Bi exist during the final discharge process and the initial charge process. Hence, the outcome is that K_3Bi is the final potassiated product of the Bi anode for PIBs.

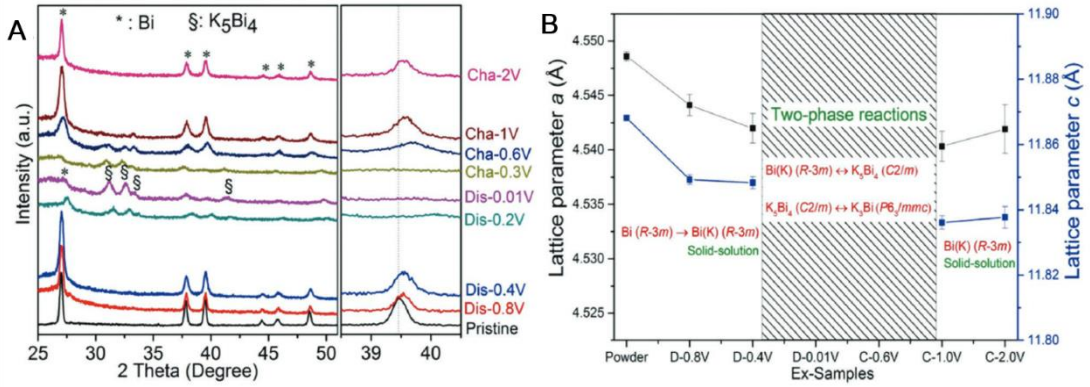

Figure 2.8. A) Ex-situ XRD measurements of Bi anode during the first potassiation/depotassiation process; B) The proposed reaction mechanism[97].

Antimony, which possesses good electrical conductivity, also can be a good candidate anode. Sb can alloy with Li and Na to form Li_3Sb [98] and Na_3Sb [99] respectively, which has high theoretical capacity of 660 mA h g^{-1}. Similar to the other alloy-based anodes, Sb undergoes huge volume variations during cycling. In addition to

considering the use of carbon as a soft matrix to buffer the volume changes in Sb anodes, the Li_3Sb and Na_3Sb are likely to form in the amorphous state, thus decreasing the barrier energies for the the transport of ions. The first attempt to apply Sb as anode for PIBs was in 2015, and a K_3Sb-O_2 battery was constructed to realize the application of a K-O_2 battery[100]. In a half-cell test, Sb/C electrode was used to identify the final discharge product and indicated the presence of K_3Sb alloy. On using K_3Sb as an alternative to conventional K metal as the anode, as shown in Figure 2.9, the overpotential was tested to be much lower than that of Li-O_2 batteries. The first demonstration of K_3Sb inspired numerous works on Sb anode, although the fast capacity fading is still the major problem for this anode. Further improved research should be focused on embedding nano-Sb particles into a uniform carbon matrix.

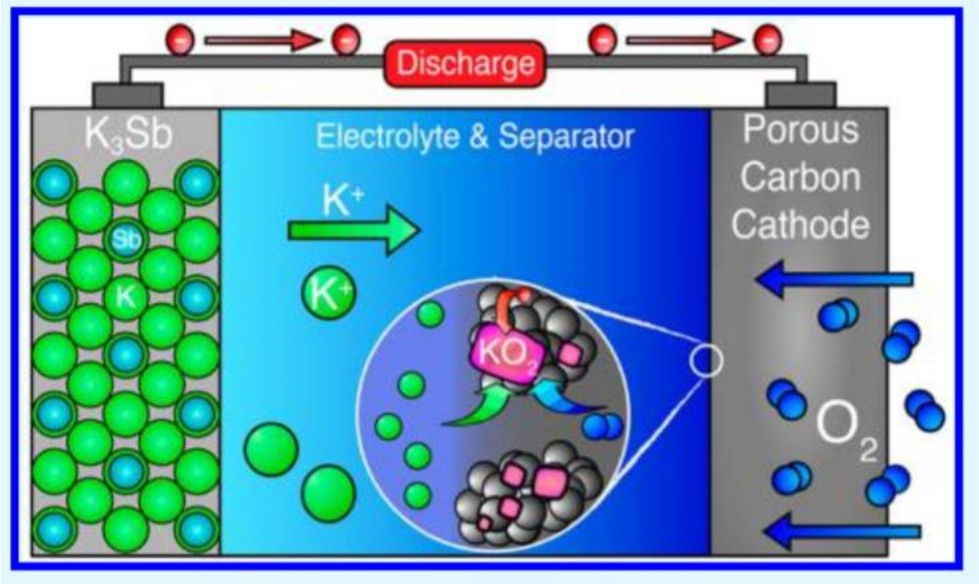

Figure 2.9. Schematic diagram of the concept of K_3Sb-O_2 batteries [100].

In addition, antimony trisulfide (Sb_2S_3) has attracted great attention due to its higher theoretical capacity and smaller volume expansion than for pure Sb anode. Compared to the similar conversion-type reaction mechanism of Sb_2O_3 and Sb_2O_4 as anodes, the possible layered structure of Sb_2S_3 offers great opportunity to develop high-performance PIBs. In a very recent study, two-dimensional (2D) Sb_2S_3 was prepared by mechanical exfoliation triggered by a solution. This unique structure could further ameliorate the large volume variations during cycling and enhance the electrical conductivity of the composite. As a result, the few-layer Sb_2S_3/C electrode exhibited long-term cycling stability and high rate capability (Figure 2.10) [101].

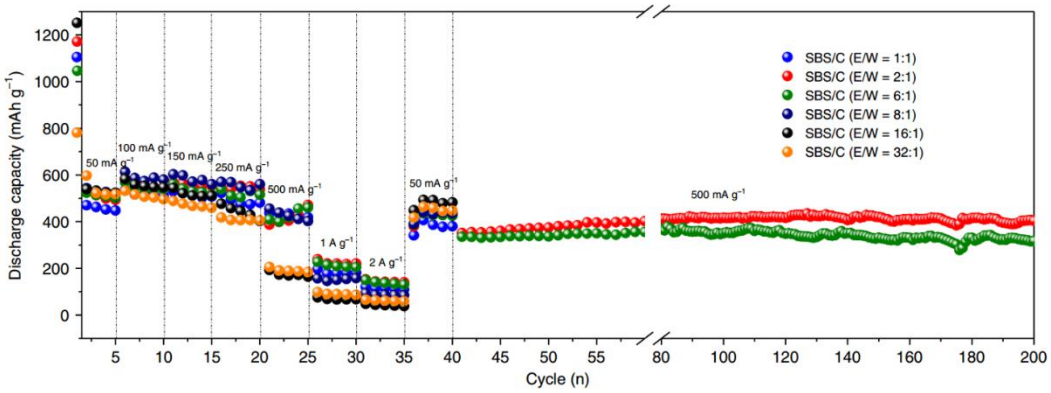

Figure 2.10. Rate capabilities of the as-prepared electrodes and their cycling performances after rate testing at a current density of 500 mA g^{-1} [101].

Germanium (Ge), belonging to the same group of elements as Si and C, also has attracted considerable attentions during the last few decades[102]. In comparison to the

other alloy-based materials, Ge is not commonly used, not only because Ge has low activity towards reaction with Na, but also because it suffers severe large volume changes during cycling. Thanks to the rapid developments of nanotechnology in recent years, amorphous Ge, Ge embedded in various types of carbon, and nanorods and nanowires of Ge [102] have offered new opportunities for Ge in Na storage, with the electrode able to deliver long-term cycling performance. Nevertheless, the huge concern arising from the high cost rose has become the main issue when Ge anode is taken into consideration for future commercial applications.

Tin (Sn) is considered as promising candidate due to its metallic nature and activity towards reaction with alkaline ions. In addition, its low discharge voltage potential offers great opportunity to develop high-energy systems when it is considered with well-matched cathodes. According to the research history of LIBs and SIBs, Sn can alloy with Li to form $Li_{22}Sn_5$ with a theoretical capacity of 990 mA h g^{-1} [103] and alloy with Na to form $Na_{15}Sn_4$ with a theoretical capacity of 847 mA h g^{-1} [104], respectively. The corresponding large volume expansions of 260 % for lithium cells and 420 % for sodium cells have resulted in huge concern, however, and probably need to be addressed with a special strategy. In generally, Sn/C nanocomposite is the best choice for developing high-performance cells due to the enhanced electrical conductivity and buffer matrix offered by soft carbon [105]. In the early research on potassium cells, Sn/graphite composite was fabricated by the ball-milling method.

Through embedding 70 wt. % Sn into 30 wt. % carbon, the composite electrodes could deliver around 150 mA h g^{-1} capacity and maintain their stability for around 30 cycles, as shown in Figure 2.11 [106]. This study was also the first attempt to demonstrate the feasibility of an alloy-based anode for the development of PIBs. In addition, it was revealed by employing ex-situ XRD characterizations that the electrochemical reaction mechanism of Sn-K involved alloying to form K_4Sn_{23} and K_2Sn_5.

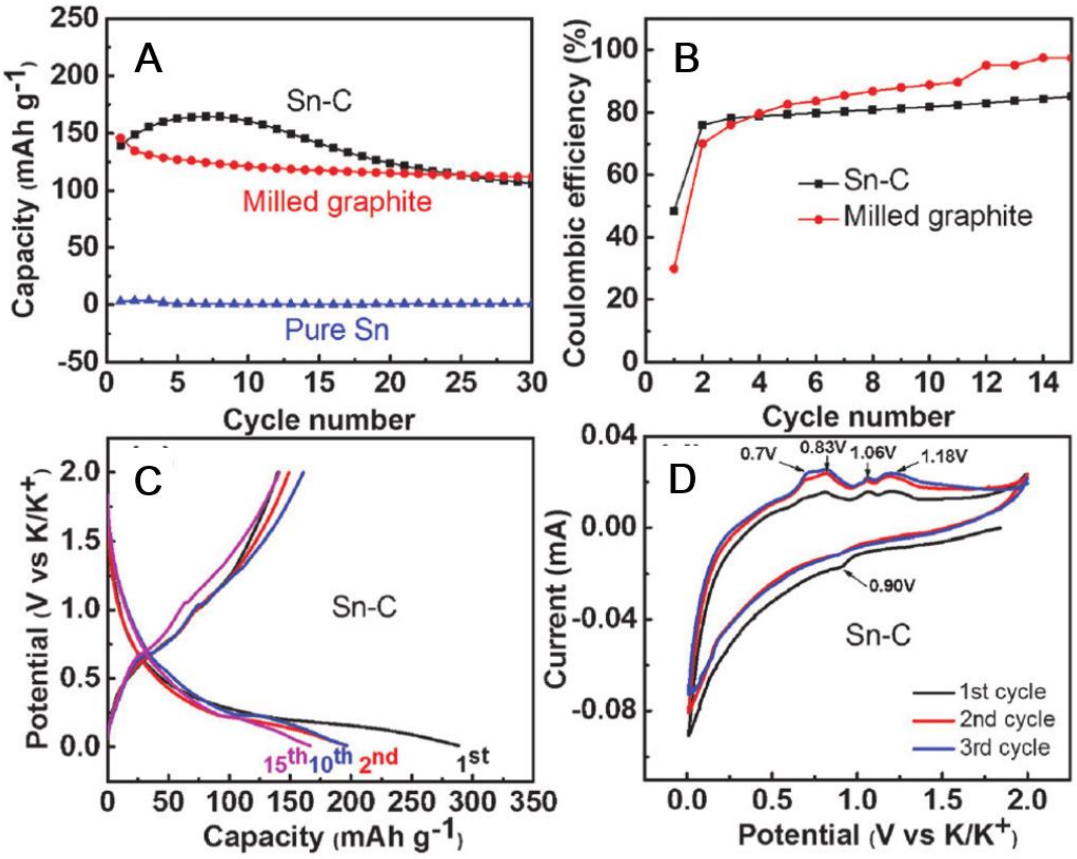

Figure 2.11. (A) Cycling performance, (B) Coulombic efficiency, and (C) galvanostatic discharge–charge profiles of Sn/C anode at the current density of 25 mA g^{-1}; (D) Cyclic voltammograms recorded at a scan rate of 0.05 mV s^{-1} [106].

The results revealed by ex-situ XRD are generally limited by the thermodynamic stability and air sensitivity of the reaction products. In light of the in-situ techniques, Xu et al. studied the reaction mechanism and capacity fading of Sn particles as anode for PIBs via in-situ TEM techniques. As shown in Figure 2.12[107], as revealed by the diffraction patterns, the reaction for the K-Sn alloying process could be identified as having two stages. In the first stage, an obvious volume expansion of 113 % could be observed for the partially potassiation of Sn. After that, it can be seen that a final 197% volume expansion was obtained after the full discharged process. It was also evidenced by the diffraction pattern that KSn phase could be formed after the fully potassiated state. As is well known, the electrochemical insertion of K ions is not only promoted by the thermodynamic process, but also controlled by the kinetic process. Thus, the phase transition during the potassiated process might be slightly different under different current densities. Therefore, the large volume change of Sn anode during potassiation/depotassiation could lead to severe electrode pulverization and capacity fading.

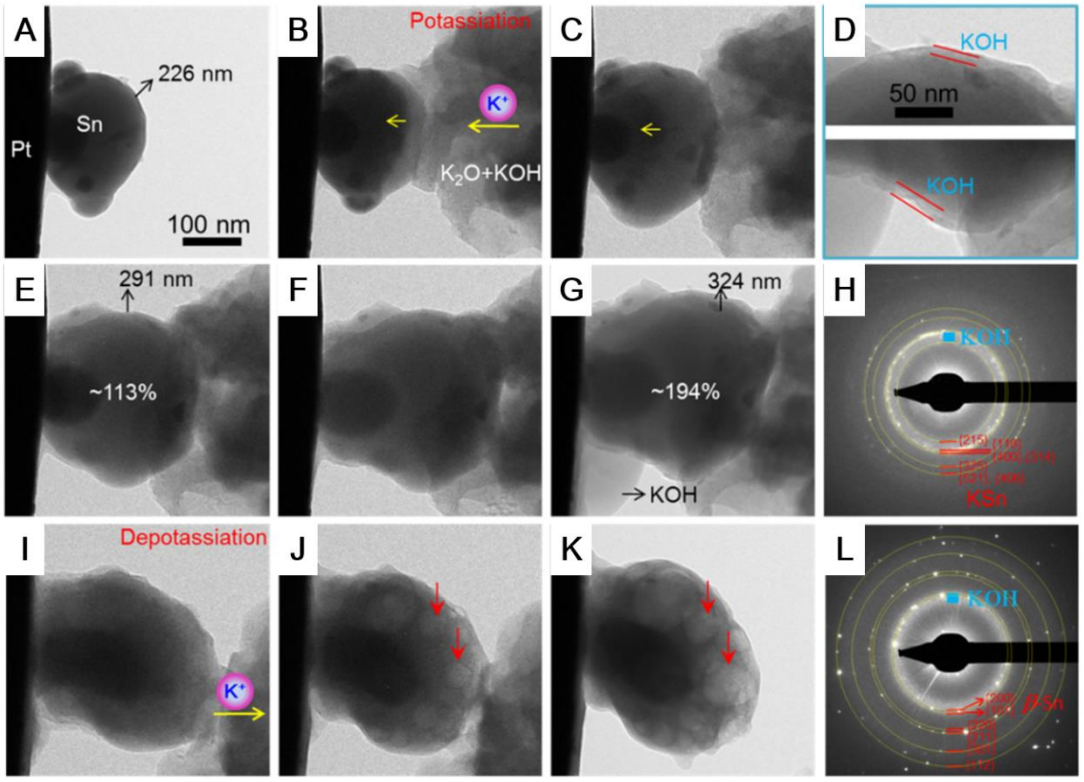

Figure 2.12. In-situ TEM observations of Sn anode. (A) TEM image of Sn particles; (B-C) first-step discharge process of Sn particles; (D−F) second-step discharge process of Sn particles; (G, I) depotassiation-induced nanopores in the nanoparticles. (J-K) Observation of KOH; SAED patterns of the (H) discharge and (L) charge processes [107].

Phosphorus, which has been considered as having the highest theoretical capacity due to the formation of Li_3P [92] and Na_3P [108], has been widely studied in recent years. Phosphorus generally has three allotropes, white, red, and black phosphorus. In terms of future commercial applications, white phosphorus is toxic and flammable at low temperature, so that it cannot be easily handled and operated [109-110]. Black

phosphorus is considered to have a similar structure to graphite, which could possess good electrical conductivity[111]. In an early research work, orthorhombic black phosphorus in a composite electrode with carbon was prepared by a simple ball-milling method [57]. In terms of electrochemical performance, various ratios of black phosphorus and carbon have been tested, but the cycling performance is not satisfactory. It was expected that it could form K_3P during the discharge process but the detected XRD signals only offer evidence of the KP phase with a theoretical capacity of 843 mA h g^{-1}. In spite of the merits of the good electrical conductivity of black phosphorus, it is hard to obtain and not stable when exposed to the air [57]. In addition, red phosphorus features the most abundant resources and is stable in air, so that it could be considered as a potential candidate anode for alkaline ion batteries. As is well known, red phosphorus has low electrical conductivity and is naturally amorphous, which could lead to poor cycling performance and large pesudocapacitance during cycling. In view of the research history of phosphorus for LIBs and SIBs, employing a carbon matrix has been considered as the most effective strategy to both improve the electrical conductivity and accommodate the stress induced by the volume variations [112]. Indeed, carbon is a good choice since it has soft capability for accommodating volume expansion. Inspired by this, Xu et al. have reported a novel method to prepare a red P@carbon nanosheet (CN) composite as anode for PIBs (Figure 2.13) [113]. The phosphorus particles could be distributed evenly throughout the porous carbon framework, which enables fast transport of the K

ions and enhances the electronic conductivity. Carbon, as a good soft matrix, could provide a protective shell to alleviate the volume changes of the phosphorus particles. Even though the volume expansions might lead to the electrode pulverization and cracks, the carbon framework could still act as a benign interconnected electronically conductive network to enable electron and ion transportation. As a result, this composite electrode exhibited high specific capacity of around 650 mA h g^{-1} at 0.1 A g^{-1} and high rate capability with around 320 mA h g^{-1} at 2 A g^{-1}.

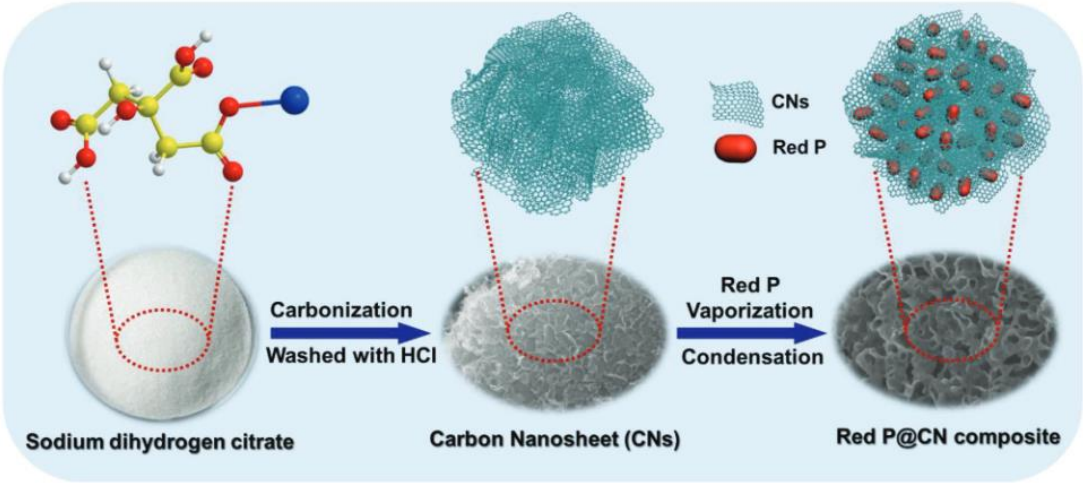

Figure 2.13. Schematic illustration of the synthesis process for red P@CN composite [113].

Along the research lines of LIBs and SIBs, the universal method is introducing a carbon matrix to buffer the volume changes for alloy elements. On the other hand, to further enhance the cycling performance, it is meaningful to include a synergistic element to buffer the volume variations during cycling. The basic design principles are introducing a synergistic element which has the various discharge plateaus that are

different from the P component. The proposed synergistic reaction mechanisms for sodium storage was demonstrated in the Sn_4P_3 system (Figure 2.14) [114]. When P is active towards reaction with the alkaline ions, the Sn will be act as a conductive matrix to protect against excess volume expansion and enhance the electrical conductivity. When Sn is active towards reaction with the alkaline ions, the P and the already formed Na_3P could be treated as a host matrix to alleviate the stress induced by the volume variation.

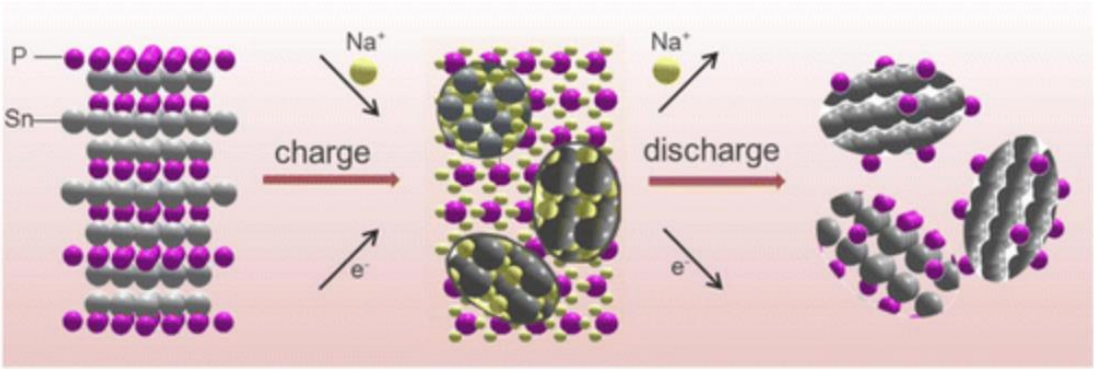

Figure 2.14. Schematic diagram of the reaction mechanism of Sn_4P_3 anode for SIBs [114].

Therefore, how to design a functional matrix is an open research topic for the development of high-performance PIBs. It is therefore necessary to introduce both carbon and Sn as buffer components to enhance the cycling stability and rate capability of phosphorus-based anode for PIBs.

In terms of the expensive cost of Ge as anode, how to reduce the loading amount of Ge in the composite seems to be a major problem. Very recently, Zhai et al. developed a facile method to introduce low-cost phosphorus to alloy with Ge to form

GeP_5 [115]. As a result, GeP_5 possesses a 2D layered structure similar to those of graphite and black phosphorus, as shown in Figure 2.15. In addition, due to the presence of metallic Ge, GeP_5 has 10^4 and 10 times higher electrical conductivity than black phosphorus and graphite, respectively. Therefore, it is also important to study the electrochemical performance of this new class of materials for PIBs.

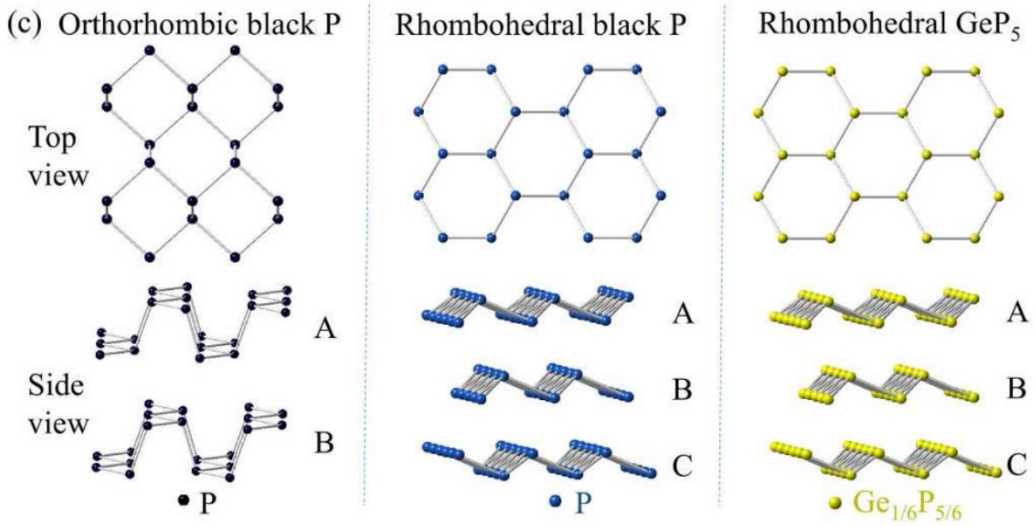

Figure 2.15. Schematic crystal model of orthorhombic black P, rhombohedral black P, and rhombohedral GeP_5 [115].

.

2.4 Electrolyte optimization

In addition to preparing suitable anode materials, electrolyte optimization is also very important to improve the electrochemical performance[116-117]. Desirable electrolytes generally need to meet three criteria: a) high stability during the electrochemical cycling to avoid electrolyte decomposition; b) ability to suppress the side reactions with metal and electrodes; and c) the ability to effectively form a stable SEI layer to facilitate the ion transportation. In the initial research on PIBs, 0.75 M KPF_6 or 0.8 M

KPF_6 in EC/diethyl carbonate (DEC) was often adopted as the electrolyte to test the electrochemical performance of various electrode materials. As was mentioned above in the discussion on graphite anode, the relatively large volume expansion compared with the graphite in LIB cells make K^+ hard to insert into graphite, thus resulting in weak reaction kinetics. Wang et al. compared the cycling performances of graphite in various solvents such as EC/DEC, EC/PC, and EC/dimethyl carbonate (DMC). As a result, they found that graphite electrode in EC/PC electrolyte could deliver over 220 mA h g^{-1} after 200 cycles, as shown in Figure 2.16 [68].

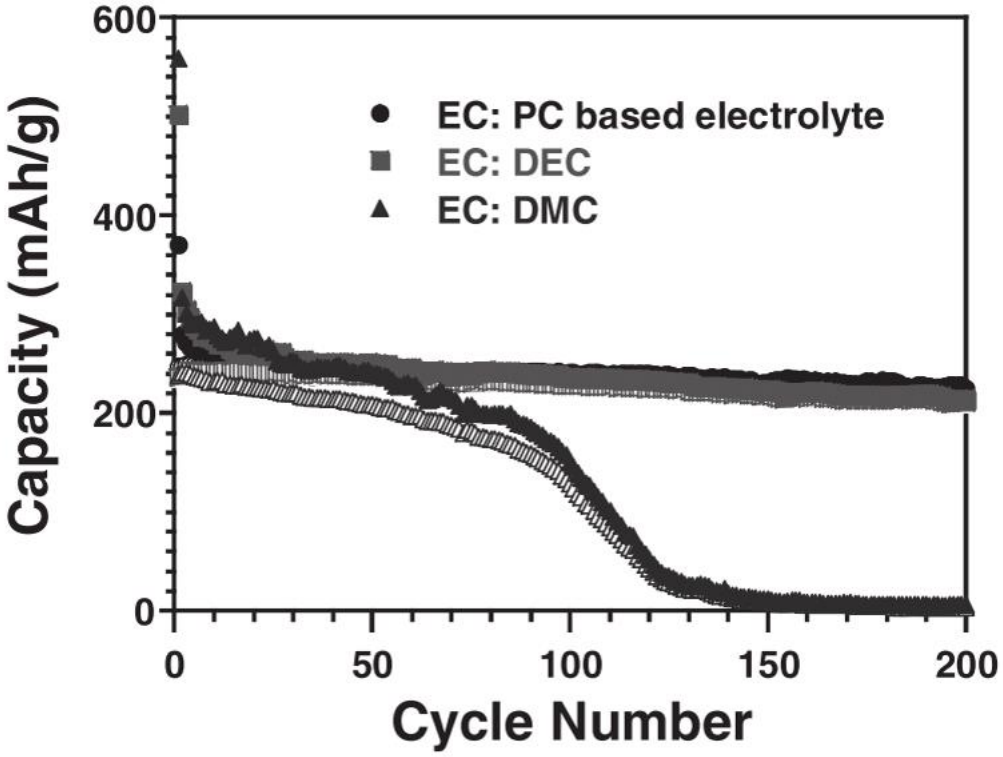

Figure 2.16 Cycling performance of graphite in electrolytes with various solvents [68].

For PIBs, conventional carbonate electrolytes are easily reduced due to the active surface of K metal, thus producing hazardous gases such as CO_2 and also some organic compounds, leading to sluggish reaction kinetics. Therefore, it is desirable to introduce ether-based electrolyte,s because it has been demonstrated that they are helpful for improving the coulombic efficiency and facilitating the transport of ions [118-119]. In recent studies, researchers found that Bi electrode in diglyme electrolyte could deliver long-term cycling stability and high rate capability [60]. In addition, Wu et al. compared dimethoxyethane (DME) with conventional carbonate electrolytes. It was proved that the DME containing electrolyte could offer small polarization and fast charge-transfer ability. As a further demonstration, TiS_2 electrode was studied, and it was found that it could deliver high rate capability[120] and that Bi in ether-based electrolyte could exhibit over 85% capacity retention even after 300 cycles, respectively.

The alloy-based electrodes generally undergo huge volume expansions and cracks during cycling, and thus will rapidly consume the electrolyte. Hence, it is expected the electrolyte should help the electrode to form a stable SEI layer. Wu et al. reported that potassium bis(fluorosulfonyl)imide (KFSI) salt in electrolyte could effectively suppress dendrite growth and avoid the excess side-reactions thus enhancing the cycling stability (Figure 2.17)[69]. It will help to form a uniform and stable SEI layer on the surface of K metal, which would help to increase the coulombic efficiency, thus enhancing the cycling stability.

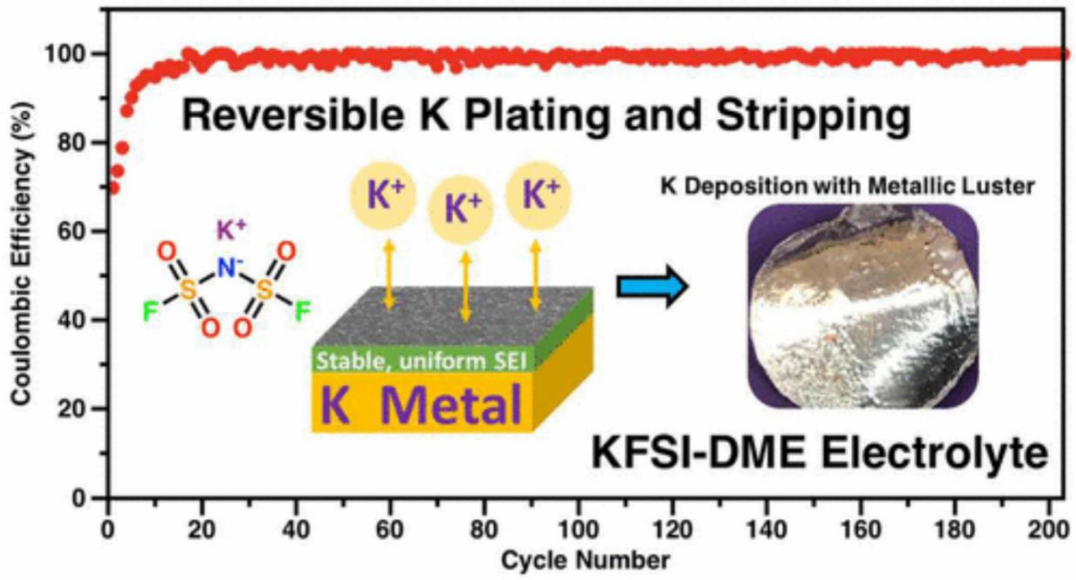

Figure 2.17. The coulombic efficiency during cycling of K metal in KFSI-DME electrolyte[69]

As is well-known in the research on SIBs, the introduction of fluoroethylene carbonate (FEC) additive generally leads to greatly improved electrochemical performance for the cell [121-124]. In this case, some researchers did pioneering work on studying the effects of the introduction of the FEC additive. With 3 wt. % addition of FEC, Bi electrode undergoes large polarization and slow reaction kinetics, so that the capacity dropped very quickly, as shown in Figure 2.18[60].

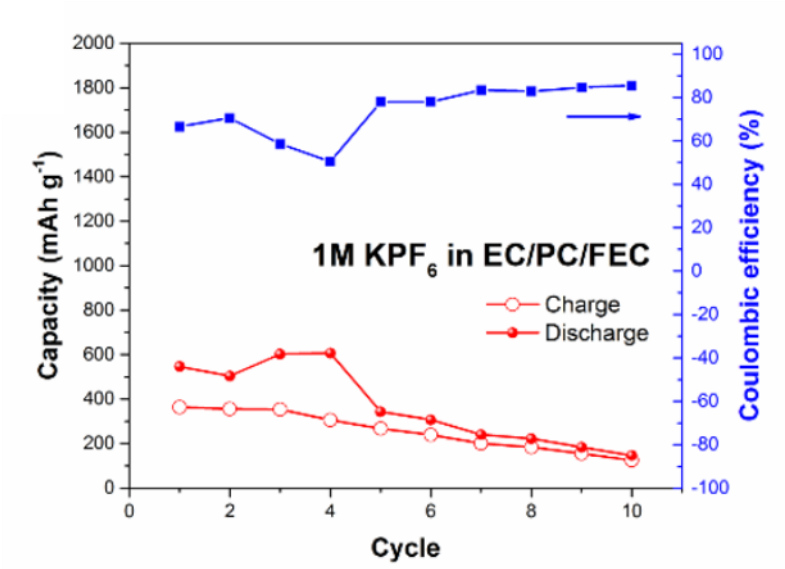

Figure 2.18. Cycling stability and coulombic efficiency of Bi electrodes in 1 M KPF_6/EC/PC/FEC electrolyte [60].

It seems that FEC may not be compatible with good cycling performance of PIBs. It has been demonstrated, however, that $K_{1.92}Fe[Fe(CN)_6]_{0.94}$ cathode with 2% FEC additive shows low interfacial resistance, and FEC could be of benefit for improving the coulombic efficiency of this cathode material [125]. Therefore, the effects of the introduction of FEC still remain open to debate.

In summary, electrolyte engineering plays an important role in regulating the formation of SEI layer and stabilizing the cycling performance of the cell. The successful application of a suitable electrolyte could finally address to the concerns relating to the SEI layer, sid- reactions, and dendrite growth. Hence, it is necessary to investigate the effects on the electrochemical performance of various electrolytes with additives.

2.5 Preparation of phosphorus-based alloy materials

Finally, to meet the requirements of future practical applications, the scalable synthesis methods are quite important. To date, several dominant synthesis routes have been reported, including ball milling[126], the hydrothermal method[127], and solid-state[128-129] processes. The phosphide anode materials prepared via the hydrothermal method exhibit good electrochemical performance, although the synthesis is relatively complicated and it is hard to obtain the pure phase, which makes it difficult to scale the synthesis up for industrial applications. Solid state processes normally depend on the diffusion speed and temperature [130-131]. Due to the high temperature treatment, solid state synthesis will unavoidably produce white phosphorus, which is chemically unstable at room temperature. Therefore, ball milling is still the most practical technique for the mass production of phosphides with high purity.

In terms of the most efficient method to produce scalable materials, ball-milling is provides direct activation to mix substances and synthesize new phases [132]. In ball milling as a typical synthesized method, a ball-milling jar to mix and grind materials together. In general, the working principles basically depend on the energy and heat produced by the friction of balls and materials themselves. Ball-milling apparatus consists of a cylinder, steel or ZrO_2 balls, and the specific milling machine [133]. When the materials are settled into a ball-milling jar with the corresponding media (balls),

the grinding process will take place at a critical speed. For industrial application, ball milling is widely used for the refinement of particles. In conventional chemical synthesis procedures, the energy dispersions are used to transport the energy into chemicals and solids to complete the solid diffusion and the mechanical alloying. In addition to the usual ball-milling technique, high-energy ball-milling was developed to grind the materials, even to below 10 nm by increasing the surface area and reaction rates[134-135]. It can be also be used to prepare substances which are generally not easy to obtain.

On the other hand, the ball-milling method could be used because it is a solvent-free routine compared with other chemical synthesis procedures. Indeed, the hydrothermal and other solution-based methods may produce more uniform morphology than ball-milling methods, although dealing with the solutions after treatment will lead to additional costs for the collection of chemical waste and may further pollute the environment to some extent[39, 136].

Most importantly, chemical reactions during ball milling are challenging, since various variables will lead to different purities, particle sizes, agglomerations, etc. The controllable variables generally include reaction time, rotation speed, type of ball-milling (wet or dry), sizes of balls, and even the material itself. Before we start to explore the experimental conditions for the various chemical synthesis procedures, it is necessary to consider the above operation conditions to achieve the most uniform and pure phases, as expected.

2.6 References

[1] A. Eftekhari, *Journal of Power Sources* **2004**, 126, 221.

[2] Z. Jian, W. Luo, X. Ji, *J. Am. Chem. Soc.* **2015**, 137, 11566.

[3] S. Komaba, T. Hasegawa, M. Dahbi, K. Kubota, *Electrochemistry Communications* **2015**, 60, 172.

[4] W. Luo, J. Wan, B. Ozdemir, W. Bao, Y. Chen, J. Dai, H. Lin, Y. Xu, F. Gu, V. Barone, *Nano Letters* **2015**, 15, 7671.

[5] K. Kubota, M. Dahbi, T. Hosaka, S. Kumakura, S. Komaba, *The Chemical Record* **2018**, 18, 459.

[6] A. Eftekhari, Z. Jian, X. Ji, *ACS Applied Materials & Interfaces* **2016**, 9, 4404.

[7] J. C. Pramudita, D. Sehrawat, D. Goonetilleke, N. Sharma, *Advanced Energy Materials* **2017**, 7, 1602911.

[8] H. Kim, J. C. Kim, M. Bianchini, D. H. Seo, J. Rodriguez‐Garcia, G. Ceder, *Adv. Energy Mater.* **2018**, 8, 1702384.

[9] W. Zhang, Y. Liu, Z. Guo, *Sci. Adv.* **2019**, 5, eaav7412.

[10] T. A. Pham, K. E. Kweon, A. Samanta, V. Lordi, J. E. Pask, *J. Phys. Chem. C* **2017**, 121, 21913.

[11] K. Share, A. P. Cohn, R. Carter, B. Rogers, C. L. Pint, *ACS Nano* **2016**, 10, 9738.

[12] K. Share, A. P. Cohn, R. E. Carter, C. L. Pint, *Nanoscale* **2016**, 8, 16435.

[13] A. P. Cohn, N. Muralidharan, R. Carter, K. Share, L. Oakes, C. L. Pint, *Journal of Materials Chemistry A* **2016**, 4, 14954.

[14] Z. Ju, S. Zhang, Z. Xing, Q. Zhuang, Y. Qiang, Y. Qian, *ACS Appl. Mater. Interfaces* **2016**, 8, 20682.

[15] Y. Li, R. A. Adams, A. Arora, V. G. Pol, A. M. Levine, R. J. Lee, K. Akato, A. K. Naskar, M. P. Paranthaman, *J. Electrochem. Soc.* **2017**, 164, A1234.

[16] R. A. Adams, J.-M. Syu, Y. Zhao, C.-T. Lo, A. Varma, V. G. Pol, *ACS Appl. Mater. Interfaces* **2017**, 9, 17872.

[17] S. Gong, Q. Wang, *J. Phys. Chem. C* **2017**, 121, 24418.

[18] G. Ma, K. Huang, J.-S. Ma, Z. Ju, Z. Xing, Q.-c. Zhuang, *Journal of Materials Chemistry A* **2017**, 5, 7854.

[19] X. Wang, K. Han, D. Qin, Q. Li, C. Wang, C. Niu, L. Mai, *Nanoscale* **2017**, 9, 18216.

[20] J. Yang, Z. Ju, Y. Jiang, Z. Xing, B. Xi, J. Feng, S. Xiong, *Adv. Mater.* **2018**, 30, 1700104.

[21] H. Yamamoto, S. Muratsubaki, K. Kubota, M. Fukunishi, H. Watanabe, J. Kim, S. Komaba, *Journal of Materials Chemistry A* **2018**, 6, 16844.

[22] K. Beltrop, S. Beuker, A. Heckmann, M. Winter, T. Placke, *Energy Environ. Sci.* **2017**, 10, 2090.

[23] L. Fan, Q. Liu, S. Chen, K. Lin, Z. Xu, B. Lu, *Small* **2017**, 13, 1701011.

[24] B. Ji, F. Zhang, X. Song, Y. Tang, *Adv. Mater.* **2017**, 29, 1700519.

[25] B. Ji, F. Zhang, N. Wu, Y. Tang, *Adv. Energy Mater.* **2017**, 7, 1700920.

[26] Z. Jian, S. Hwang, Z. Li, A. S. Hernandez, X. Wang, Z. Xing, D. Su, X. Ji, *Adv. Funct. Mater.* **2017**, 27, 1700324.

[27] Y. Xie, Y. Chen, L. Liu, P. Tao, M. Fan, N. Xu, X. Shen, C. Yan, *Adv. Mater.* **2017**, 29, 1702268.

[28] X. Zhao, P. Xiong, J. Meng, Y. Liang, J. Wang, Y. Xu, *Journal of Materials Chemistry A* **2017**, 5, 19237.

[29] P. Bhauriyal, A. Mahata, B. Pathak, *J. Phys. Chem. C* **2018**, 122, 2481.

[30] R. Hao, H. Lan, C. Kuang, H. Wang, L. Guo, *Carbon* **2018**, 128, 224.

[31] X. Jiang, B. Song, D. Tománek, *Physical Review Applied* **2018**, 9, 044015.

[32] J. Li, W. Qin, J. Xie, H. Lei, Y. Zhu, W. Huang, X. Xu, Z. Zhao, W. Mai, *Nano Energy* **2018**, 53, 415.

[33] Y. Liu, C. Yang, Q. Pan, Y. Li, G. Wang, X. Ou, F. Zheng, X. Xiong, M. Liu, Q. Zhang, *Journal of Materials Chemistry A* **2018**, 6, 15162.

[34] X. Qi, K. Huang, X. Wu, W. Zhao, H. Wang, Q. Zhuang, Z. Ju, *Carbon* **2018**, 131, 79.

[35] Y. Liu, Z. Tai, Q. Zhang, H. Wang, W. K. Pang, H. K. Liu, K. Konstantinov, Z. Guo, *Nano Energy* **2017**, 35, 36.

[36] X. Ren, Q. Zhao, W. D. McCulloch, Y. Wu, *Nano Research* **2017**, 10, 1313.

[37] K. Xie, K. Yuan, X. Li, W. Lu, C. Shen, C. Liang, R. Vajtai, P. Ajayan, B. Wei, *Small* **2017**, 13, 1701471.

[38] M. Mao, C. Cui, M. Wu, M. Zhang, T. Gao, X. Fan, J. Chen, T. Wang, J. Ma, C. Wang, *Nano Energy* **2018**, 45, 346**.**

[39] H. Gao, T. Zhou, Y. Zheng, Q. Zhang, Y. Liu, J. Chen, H. Liu, Z. Guo, *Adv. Funct. Mater.* **2017**, 27, 1702634.

[40] V. Lakshmi, Y. Chen, A. A. Mikhaylov, A. G. Medvedev, I. Sultana, M. M. Rahman, O. Lev, P. V. Prikhodchenko, A. M. Glushenkov, *Chem. Commun.* **2017**, 53, 8272.

[41] J. Zhou, L. Wang, M. Yang, J. Wu, F. Chen, W. Huang, N. Han, H. Ye, F. Zhao, Y. Li, *Adv. Mater.* **2017**, 29.

[42] M. Chen, W. Wang, X. Liang, S. Gong, J. Liu, Q. Wang, S. Guo, H. Yang, *Adv. Energy Mater.* **2018**.

[43] Z. Chen, D. Yin, M. Zhang, *Small* **2018**.

[44] H. Wang, W. Zhang, H. Liu, Z. Guo, *Angewandte Chemie International Edition* **2016**, 55, 3992.

[45] H. Wang, W. Zhang, J. Xu, Z. Guo, *Adv. Funct. Mater.* **2018**, 1707520.

[46] Y. Lu, J. Chen, *Science China Chemistry* **2017**, 60, 1533.

[47] B. Tian, W. Tang, K. Leng, Z. Chen, S. J. R. Tan, C. Peng, G.-H. Ning, W. Fu, C. Su, G. W. Zheng, *ACS Energy Letters* **2017**, 2, 1835.

[48] J. Ge, L. Fan, J. Wang, Q. Zhang, Z. Liu, E. Zhang, Q. Liu, X. Yu, B. Lu, *Adv. Energy Mater.* **2018**, 1801477.

[49] B. Jia, Q. Yu, Y. Zhao, M. Qin, W. Wang, Z. Liu, C. Y. Lao, Y. Liu, H. Wu, Z. Zhang, *Adv. Funct. Mater.* **2018**, 1803409.

[50] J. Xie, Y. Zhu, N. Zhuang, H. Lei, W. Zhu, Y. Fu, M. S. Javed, J. Li, W. Mai, *Nanoscale* **2018**.

[51] W. Zhang, J. Mao, S. Li, Z. Chen, Z. Guo, *J. Am. Chem. Soc.* **2017**, 139, 3316.

[52] W. Zhang, Z. Wu, J. Zhang, G. Liu, N.-H. Yang, R.-S. Liu, W. K. Pang, W. Li, Z. Guo, *Nano Energy* **2018**.

[53] W. Zhang, W. K. Pang, V. Sencadas, Z. Guo, *Joule* **2018**, 2, 1534.

[54] D. Liu, X. Huang, D. Qu, D. Zheng, G. Wang, J. Harris, J. Si, T. Ding, J. Chen, D. Qu, *Nano Energy* **2018**, 52, 1.

[55] S. Mukherjee, L. Kavalsky, C. V. Singh, *ACS Appl. Mater. Interfaces* **2018**, 10, 8630.

[56] T. Ramireddy, R. Kali, M. K. Jangid, V. Srihari, H. K. Poswal, A. Mukhopadhyay, *J. Electrochem. Soc.* **2017**, 164, A2360.

[57] I. Sultana, M. M. Rahman, T. Ramireddy, Y. Chen, A. M. Glushenkov, *Journal of Materials Chemistry A* **2017**, 5, 23506.

[58] Z. Huang, Z. Chen, S. Ding, C. Chen, M. Zhang, *Mater. Lett.* **2018**, 219, 19.

[59] A. Y. Galashev, A. S. Vorob'ev, *J. Solid State Electrochem.* **2018**, 1.

[60] J. Huang, X. Lin, H. Tan, B. Zhang, *Adv. Energy Mater.* **2018**, 8, 1703496.

[61] K. Huang, Z. Xing, L. Wang, X. Wu, W. Zhao, X. Qi, H. Wang, Z. Ju, *Journal of Materials Chemistry A* **2018**, 6, 434.

[62] Z. Huang, Z. Chen, S. Ding, C. Chen, M. Zhang, *Solid State Ionics* **2018**, 324, 267.

[63] N. Li, F. Zhang, Y. Tang, *Journal of Materials Chemistry A* **2018**.

[64] H. Wang, L. Wang, L. Wang, Z. Xing, X. Wu, W. Zhao, X. Qi, Z. Ju, Q. Zhuang, *Journal of Materials Chemistry A* **2018**, 6, 434.

[65] W. Wang, B. Jiang, C. Qian, F. Lv, J. Feng, J. Zhou, K. Wang, C. Yang, Y. Yang, S. Guo, *Adv. Mater.* **2018**, 1801812.

[66] Y. Liu, X.-Y. Yu, Y. Fang, X. Zhu, J. Bao, X. Zhou, X. W. D. Lou, *Joule* **2018**, 2, 725.

[67] C. Yan, X. Gu, L. Zhang, L. Yan, D. Liu, L. Li, P. Dai, X. Zhao, *Journal of Materials Chemistry A* **2018**, 6, 17371.

[68] J. Zhao, X. Zou, Y. Zhu, Y. Xu, C. Wang, *Adv. Funct. Mater.* **2016**, 26, 8103.

[69] N. Xiao, W. D. McCulloch, Y. Wu, *J. Am. Chem. Soc.* **2017**, 139, 9475.

[70] R. A. Adams, A. Varma, V. G. Pol, *J. Power Sources* **2018**, 375, 131.

[71] X. Ren, Y. Wu, *J. Am. Chem. Soc.* **2013**, 135, 2923.

[72] W. Wang, N. C. Lai, Z. Liang, Y. Wang, Y. C. Lu, *Angew. Chem.* **2018**, 130, 5136.

[73] W. Yu, K. C. Lau, Y. Lei, R. Liu, L. Qin, W. Yang, B. Li, L. A. Curtiss, D. Zhai, F. Kang, *ACS Appl. Mater. Interfaces* **2017**, 9, 31871.

[74] S. Sankarasubramanian, V. K. Ramani, *J. Phys. Chem. C* **2018**.

[75] N. Xiao, R. T. Rooney, A. A. Gewirth, Y. Wu, *Angew. Chem.* **2018**, 130, 1241.

[76] P. G. Bruce, B. Scrosati, J. M. Tarascon, *Angewandte Chemie International Edition* **2008**, 47, 2930.

[77] P. Ge, M. Fouletier, *Solid State Ionics* **1988**, 28, 1172.

[78] Z. Xing, Y. Qi, Z. Jian, X. Ji, *ACS Appl. Mater. Interfaces* **2016**, 9, 4343.

[79] Y. An, H. Fei, G. Zeng, L. Ci, B. Xi, S. Xiong, J. Feng, *J. Power Sources* **2018**, 378, 66.

[80] Z. Tai, Q. Zhang, Y. Liu, H. Liu, S. Dou, *Carbon* **2017**, 123, 54.

[81] H. Zhang, J. Nai, L. Yu, X. W. D. Lou, *Joule* **2017**, 1, 77.

[82] P. Xiong, X. Zhao, Y. Xu, *ChemSusChem* **2018**, 11, 202.

[83] D.-S. Bin, Z.-X. Chi, Y. Li, K. Zhang, X. Yang, Y.-G. Sun, J.-Y. Piao, A.-M. Cao, L.-J. Wan, *J. Am. Chem. Soc.* **2017**, 139, 13492.

[84] B. Cao, Q. Zhang, H. Liu, B. Xu, S. Zhang, T. Zhou, J. Mao, W. K. Pang, Z. Guo, A. Li, *Adv. Energy Mater.* **2018**, 1801149.

[85] Z. Jian, Z. Xing, C. Bommier, Z. Li, X. Ji, *Adv. Energy Mater.* **2016**, 6.

[86] C. Chen, Z. Wang, B. Zhang, L. Miao, J. Cai, L. Peng, Y. Huang, J. Jiang, Y. Huang, L. Zhang, J. Xie, *Energy Storage Materials* **2017**, 8, 161.

[87] Y. Xu, C. Zhang, M. Zhou, Q. Fu, C. Zhao, M. Wu, Y. Lei, *Nat. Commun.* **2018**, 9, 1720.

[88] W. Wang, J. Zhou, Z. Wang, L. Zhao, P. Li, Y. Yang, C. Yang, H. Huang, S. Guo, *Adv. Energy Mater.* **2017**.

[89] I. Sultana, M. M. Rahman, Y. Chen, A. M. Glushenkov, *Adv. Funct. Mater.* **2018**, 28, 1703857.

[90] W. Zhang, J. Mao, W. K. Pang, Z. Guo, Z. Chen, *Electrochim. Acta* **2017**, 235, 107.

[91] Y. Yu, L. Gu, C. Wang, A. Dhanabalan, P. A. Van Aken, J. Maier, *Angew. Chem.* **2009**, 121, 6607.

[92] L. Wang, X. He, J. Li, W. Sun, J. Gao, J. Guo, C. Jiang, *Angew. Chem.* **2012**, 124, 9168.

[93] Y. Kim, Y. Park, A. Choi, N. S. Choi, J. Kim, J. Lee, J. H. Ryu, S. M. Oh, K. T. Lee, *Adv. Mater.* **2013**, 25, 3045.

[94] U. Kasavajjula, C. Wang, A. J. Appleby, *J. Power Sources* **2007**, 163, 1003.

[95] O. Crosnier, T. Brousse, X. Devaux, P. Fragnaud, D. Schleich, *J. Power Sources* **2001**, 94, 169.

[96] C. Wang, L. Wang, F. Li, F. Cheng, J. Chen, *Adv. Mater.* **2017**, 29, 1702212.

[97] Q. Zhang, J. Mao, W. K. Pang, T. Zheng, V. Sencadas, Y. Chen, Y. Liu, Z. Guo, *Adv. Energy Mater.* **2018**, 8, 1703288.

[98] H. Lv, S. Qiu, G. Lu, Y. Fu, X. Li, C. Hu, J. Liu, *Electrochim. Acta* **2015**, 151, 214.

[99] W. Zhang, J. Mao, W. K. Pang, X. Wang, Z. Guo, *Nano Energy* **2018**, 49, 549.

[100] W. D. McCulloch, X. Ren, M. Yu, Z. Huang, Y. Wu, *ACS Appl. Mater. Interfaces* **2015**, 7, 26158.

[101] Y. Liu, Z. Tai, J. Zhang, W. K. Pang, Q. Zhang, H. Feng, K. Konstantinov, Z. Guo, H. K. Liu, *Nat. Commun.* **2018**, 9, 3645.

[102] D. Li, H. Wang, T. Zhou, W. Zhang, H. K. Liu, Z. Guo, *Adv. Energy Mater.* **2017**, 7, 1700488.

[103] G. Derrien, J. Hassoun, S. Panero, B. Scrosati, *Adv. Mater.* **2007**, 19, 2336.

[104] Y. Liu, N. Zhang, L. Jiao, Z. Tao, J. Chen, *Adv. Funct. Mater.* **2015**, 25, 214.

[105] Y. Xu, Y. Zhu, Y. Liu, C. Wang, *Adv. Energy Mater.* **2013**, 3, 128.

[106] I. Sultana, T. Ramireddy, M. M. Rahman, Y. Chen, A. M. Glushenkov, *Chem. Commun.* **2016**, 52, 9279.

[107] Q. Wang, X. Zhao, C. Ni, H. Tian, J. Li, Z. Zhang, S. X. Mao, J. Wang, Y. Xu, *J. Phys. Chem. C* **2017**, 121, 12652.

[108] Y. Zhu, Y. Wen, X. Fan, T. Gao, F. Han, C. Luo, S.-C. Liou, C. Wang, *ACS Nano* **2015**, 9, 3254.

[109] W.-J. Li, S.-L. Chou, J.-Z. Wang, H.-K. Liu, S.-X. Dou, *Nano Lett.* **2013**, 13, 5480.

[110] T. Ramireddy, T. Xing, M. M. Rahman, Y. Chen, Q. Dutercq, D. Gunzelmann, A. M. Glushenkov, *Journal of Materials Chemistry A* **2015**, 3, 5572.

[111] J. Sun, H.-W. Lee, M. Pasta, H. Yuan, G. Zheng, Y. Sun, Y. Li, Y. Cui, *Nat. Nanotechnol.* **2015**, 10, 980.

[112] X. Wu, W. Zhao, H. Wang, X. Qi, Z. Xing, Q. Zhuang, Z. Ju, *J. Power Sources* **2018**, 378, 460.

[113] P. Xiong, P. Bai, S. Tu, M. Cheng, J. Zhang, J. Sun, Y. Xu, *Small* **2018**, 1802140.

[114] J. Qian, Y. Xiong, Y. Cao, X. Ai, H. Yang, *Nano Lett.* **2014**, 14, 1865.

[115] W. Li, H. Li, Z. Lu, L. Gan, L. Ke, T. Zhai, H. Zhou, *Energy Environ. Sci.* **2015**, 8, 3629.

[116] V. A. Nikitina, S. M. Kuzovchikov, S. S. Fedotov, N. R. Khasanova, A. M. Abakumov, E. V. Antipov, *Electrochim. Acta* **2017**, 258, 814.

[117] T. Yamamoto, K. Matsumoto, R. Hagiwara, T. Nohira, *J. Phys. Chem. C* **2017**, 121, 18450.

[118] S. Jiao, X. Ren, R. Cao, M. H. Engelhard, Y. Liu, D. Hu, D. Mei, J. Zheng, W. Zhao, Q. Li, *Nat. Energy* **2018**.

[119] P. Lian, Y. Dong, Z.-S. Wu, S. Zheng, X. Wang, W. Sen, C. Sun, J. Qin, X. Shi, X. Bao, *Nano Energy* **2017**, 40, 1.

[120] L. Wang, J. Zou, S. Chen, G. Zhou, J. Bai, P. Gao, Y. Wang, X. Yu, J. Li, Y.-S. Hu, *Energy Storage Materials* **2018**, 12, 216.

[121] Q. Wang, W. Zhang, C. Guo, Y. Liu, C. Wang, Z. Guo, *Adv. Funct. Mater.* **2017**, 27, 1703390.

[122] M. D. Slater, D. Kim, E. Lee, C. S. Johnson, *Adv. Funct. Mater.* **2013**, 23, 947.

[123] J. Chen, A. Pan, Y. Wang, X. Cao, W. Zhang, X. Kong, Q. Su, J. Lin, G. Cao, S. Liang, *Energy Storage Materials* **2018**.

[124] Q. Wang, J. Xu, W. Zhang, M. Mao, Z. Wei, L. Wang, C. Cui, Y. Zhu, J. Ma, *Journal of Materials Chemistry A* **2018**, 6, 8815.

[125] J. Liao, Q. Hu, Y. Yu, H. Wang, Z. Tang, Z. Wen, C. Chen, *Journal of Materials Chemistry A* **2017**, 5, 19017.

[126] Y. Kim, Y. Kim, A. Choi, S. Woo, D. Mok, N. S. Choi, Y. S. Jung, J. H. Ryu, S. M. Oh, K. T. Lee, *Advanced Materials* **2014**, 26, 4139.

[127] J. Liu, P. Kopold, C. Wu, P. A. van Aken, J. Maier, Y. Yu, *Energy & Environmental Science* **2015**, 8, 3531.

[128] J. Fullenwarth, A. Darwiche, A. Soares, B. Donnadieu, L. Monconduit, *Journal of Materials Chemistry A* **2014**, 2, 2050.

[129] J. Hao, J. Zhang, G. Xia, Y. Liu, Y. Zheng, W. Zhang, Y. Tang, W. K. Pang, Z. Guo, *ACS Nano* **2018**, 12, 10430.

[130] W.-c. Zhang, L.-b. Liu, M.-t. Zhang, G.-x. Huang, J.-s. Liang, L. Xian, L.-g. Zhang, *Transactions of the Nonferrous Metals Society of China* **2015**, 25, 3700.

[131] H. Bo, L. Liu, J. Hu, W. Zhang, Z. Jin, *Thermochim. Acta* **2015**, 609, 36.

[132] B. Kang, G. Ceder, *Nature* **2009**, 458, 190.

[133] W. Zhao, M. Fang, F. Wu, H. Wu, L. Wang, G. Chen, *J. Mater. Chem.* **2010**, 20, 5817.

[134] A. S. Arico, P. Bruce, B. Scrosati, J.-M. Tarascon, W. Van Schalkwijk, in *Materials For Sustainable Energy: A Collection of Peer-Reviewed Research*

and Review Articles from Nature Publishing Group, World Scientific **2011**, p. 148. Edited by Dusastre, Vincent. Published by Macmillan Publishers Ltd, London.

[135] S. Indris, R. Amade, P. Heitjans, M. Finger, A. Haeger, D. Hesse, W. Grünert, A. Börger, K. D. Becker, *The Journal of Physical Chemistry B* **2005**, 109, 23274.

[136] C. Zeng, F. Xie, X. Yang, M. Jaroniec, L. Zhang, S. Z. Qiao, *Angew. Chem. Int. Ed. Engl.* **2018**, 57, 8540.

Chapter 3
3. Experimental Procedures

3.1. Overview

The general procedures in this thesis work were to prepare the electrode active materials for assembling into batteries, testing their electrochemical performance, and investigating the reaction mechanisms during cycling. Two kinds of phosphides (Sn_4P_3 and GeP_5) were prepared via ball-milling and high-energy ball-milling methods, respectively. To improve the electrochemical performance of agglomerated microsized Sn_4P_3 particles produced by the ball-milling procedure, the Sn_4P_3 particles were confined in carbon fibres produced via a further electrospinning process. Then, the physical and microscopic properties were characterized by a series of techniques, such as X-ray diffraction (XRD), Raman spectroscopy, X-ray photoelectron spectroscopy (XPS), thermogravimetric analysis (TGA), scanning electron microscopy (SEM), and transmission electron microscopy (TEM). Finally, their electrochemical performances were evaluated in half-cell tests for PIB applications, and the reaction mechanisms were revealed by ex-situ or *in-operando* XRD measurements.

.

3.2. Chemicals and Materials

The chemicals and materials used in this work are listed in Table 3.1.

Table 3.1 Chemicals and materials used in this work.

Chemicals	Formula	Purity (%)	Supplier
Tin	Sn	99.8	Sigma Aldrich
Red phosphorus	P	99%	Sigma Aldrich
Germanium	Ge	99.99%	Sigma Aldrich
Ethanol	C_2H_5OH	Reagent	Chem-Supply Pty. Ltd.
***N,N*-Dimethylformamide**	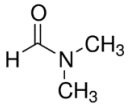	99^+	Sigma-Aldrich
Polyacrylonitrile	$(C_3H_3N)n$	99	Sigma-Aldrich
Carboxymethyl cellulose	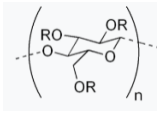	99	Sigma-Aldrich
Carbon black	C	Super P	Timcal Belgium
Polyvinylidene difluoride (PVDF)	$(CH_2CF_2)_n$	N/A	Sigma-Aldrich
N-methyl-2-pyrrolidone (NMP)	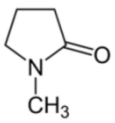	99.5^+	Sigma-Aldrich
Copper foil	Cu	N/A	Vanlead Tech
CR2032 type coin cells	N/A	N/A	China

Ethylene carbonate (EC)	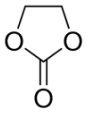	99^{+}	Sigma-Aldrich
Diethyl carbonate (DEC)	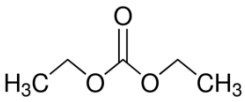	99^{+}	Sigma-Aldrich
Fluoroethylene carbonate (FEC)	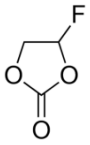	99	Sigma-Aldrich
Potassium metal	K	99.9	Sigma-Aldrich
Potassium hexafluorophosphate	KPF_6	99.99	Sigma-Aldrich
Lithium hexafluorophosphate	$LiPF_6$	99.99	Sigma-Aldrich
Sodium hexafluorophosphate	$NaPF_6$	99.99	Sigma-Aldrich
Potassium bis(fluorosulfonyl)imide	$F_2KNO_4S_2$		
Sodium metal	Na	99.9	Sigma-Aldrich
Lithium foil	Li	99	Sigma-Aldrich
Copper foil	Cu	N/A	China

3.3. Materials Preparation

In this research work, the experimental procedures could be mainly divided into three parts, as mentioned in section 3.1. The first part was focused on the preparation of active materials. The preparation methods used in this work mainly include the ball-milling method for the preparation of various pure phosphide phases and afterwards the electrospinning procedure.

3.3.1. Ball-milling method

Ball milling was conducted in a planetary QM-1SP2 ball mill for 30 h, and the elemental mixture was milled at 500 rpm using stainless steel balls 10 mm in diameter and with a powder-to-ball weight ratio of 1:30. All sample storage and handling were performed in an Ar filled glove box (MBraun Unilab).

3.3.2. High-energy ball-milling method

GeP_5 powder was obtained by a high-energy ball-milling (HEBM, Fritsch Pulverisette-6. Germany) process using commercial Ge and red phosphorus as the raw materials in the mole ratio of Ge: P = 1: 5. The HEBM was conducted at 500 rpm for 10 h, and the elemental mixture was milled using ball-mill beads 10 mm in diameter with a powder-to-ball weight ratio of 1:20. All sample storage and handling were performed in an Ar filled glove box (MBraun Unilab).

3.3.3. Electrospinning procedure

Polyacrylonitrile (PAN) (Sigma, Mn = 100 kDa) was dissolved in dimethyl formamide (DMF) at a concentration of 10 % (w/v), and the desired amount of Sn_4P_3 (10, 20, 30, and 40 wt. %, relative to the polymer content) was added into the solution, which was placed in an ultrasound bath (Bandelin, Sonorex Super RK106) for 6 hr to disperse clusters and enhance the homogeneous dispersion of the filler in the polymer solution. Afterwards, the solution was transferred to a magnetic stirrer to achieve complete polymer dissolution. The nanocomposite solution was then placed in a glass syringe fitted with a steel needle with an inner diameter of 0.5 mm. Electrospinning

was conducted with an electric field of 1.75 kV cm^{-1}, applied with a high voltage power supply from Gamma High Voltage. A syringe pump (from KD Scientific) was used to feed the polymer solutions into the needle tip at 0.5 mL h^{-1}. The electrospun non-woven meshes were collected on a static aluminium plate placed at 15 cm from the needle tip.

3.4. Characterization Techniques

3.4.1. Thermogravimetric Analysis (TGA)

TGA is a common method for analyzing the mass composition in specific samples. It relies on mass changes over time as the temperature increases. For instance, the phase transitions, including absorption and desorption, could be identified via this method. Generally, it is conducted on a a specialized thermogravimetric analyzer. As the temperature increased with time, changes in the sample mass could be observed. In this thesis work, a TGA Instruments 2000 in the Institute for Superconducting & Electronic Materials (ISEM) of the University of Wollongong (UOW) was applied to evaluate the carbon contents in the Sn_4P_3@ carbon fibre composites.

3.4.2. X-ray Diffraction (XRD)

XRD is also known as X-ray crystallography, which is a basic technique to determine the crystal structure and phase composition of a specimen in response to a beam of X-rays. The fundamental design principle of XRD is based on Bragg's law ($2d\sin\theta = n$

λ), where *d* is the spacing distance of the diffraction planes, θ is the incident angle, *n* is any integer, and λ is the wavelength of the beam. Gernerally, X-rays are applied to produce the diffraction pattern due to the relationship between the wavelength and the spacing. In principle, the specific crystal planes will reflect the X-rays, producing XRD patterns which can be used to analysis the phase components and crystal structures. In this thesis work, the crystal structures of the as-prepared powders were characterized by powder X-ray diffraction (XRD) on a GBC MMA diffractometer with a Cu Kα source at a scanning rate of 1 °min^{-1}.

3.4.3. Raman Spectroscopy

Raman spectroscopy is a spectroscopic method to help analyze the vibration modes in the samples. It is generally used to obtain chemical and structural information such as with the Disordered (D) or Graphitic (G) bands in the carbon samples. Due to the amorphous features of Super P carbon black and the carbon fibres, XRD could not be used to identify the carbon in this thesis work. Raman spectra of D and G bands of carbon were observed by using a Raman spectrometer (Lab RAM HR, Horiba Jobin Yvon SAS) in the Intelligent Polymer Research Institute (IPRI) of UOW.

3.4.4. X-ray Photoelectron Spectroscopy (XPS)

XPS is considered a form of electron spectroscopy for surface chemistry analysis because it can be used to provide the chemical states of various elements and also offer valuable quantitative information. Generally, XPS could be used to provide surface information ob the sample because it can only reach a 5-10 nm depth from the

top of the material. A typical XPS spectrum includes the binding energies of the corresponding elements and the detected electrons. The characteristic binding energy is directly linked to each specific element in the elemental periodic table. In this case, these peaks could be used to identify the electron configurations of the electrons within the atoms such as 1s, 2p, 2s, 3s, etc. In addition, the collected signals produced by the samples could be applied to calculate the corresponding atomic fraction existing in the sample. In this thesis work, XPS was conducted using a PHOIBOS 100 Analyser from SPECS, which is installed in a high-vacuum chamber with base pressure < 10^{-8} mbar. X-ray excitation was provided by Al K_α radiation with photon energy $h\nu$ = 1486.6 eV at 12 kV and 120 W. The XPS binding energy spectra were collected at the pass energy of 20 eV in the fixed analyser transmission mode. All the XPS data was analyzed using the commercial CasaXPS 2.3.15 software package. Before analysis, the spectra were calibrated by C 1s = 284.6 eV.

3.4.5. Scanning Electron Microscopy (SEM)

An SEM can be referred as an electron microscope, which produces electrons from an electron gun and focuses them into a fine probe which impinges on the surface of a target specimen, where electron-specimen interactions result in a number of distinct emission signals from which images can be derived. The signals that derive from electron-sample interactions reveal information about the sample, including its external morphology, chemical composition, and the crystalline structure and orientation of materials making up the sample[1]. In most applications, data are

collected over a selected area of the surface of the sample, and a 2D image is generated that displays spatial variations in these properties. Areas ranging from approximately 1 cm to 5 microns in width can be imaged in scanning mode using conventional SEM techniques (magnification ranging from 20× to approximately 30,000×, spatial resolution of 50 to 100 nm)[2]. In this thesis work, the morphology of various atomically thin transition metal oxides was detected by a field emission scanning electron microscope (JSM-7500FA, JEOL, Tokyo, Japan) located in the Electron Microscopy Center (EMC) of UOW.

3.4.6. Transmission Electron Microscopy (TEM) and Scanning Transmission Electron Microscopy (STEM)

TEM is a microscopic technique where electrons are transmitted through the sample, thus providing an image that can give detailed morphology information. Because the electrons need to pass through the sample, the specimen is required to be less than 100 nm thick and also loaded on the copper grid. In addition, owing to its having he advantage of higher voltage than that in the SEM technique, TEM is always used to investigate the detailed morphology of a specimen, such as its nanostructures and derived products. In this doctoral work, the TEM observations of the samples were carried out using a JEM-2011F (JEOL, Tokyo, Japan) and a probe-corrected JEOL ARM200F (equipped with a cold field emission gun, a high resolution pole-piece, and a Centurio energy dispersive spectroscopy (EDS) detector) at 200 kV in EMC of UOW.

3.4.7. Fourier-transform infrared spectroscopy (FTIR) mapping

FTIR is a useful tool to investigate the infrared spectrum of adsorption or emission from solid, liquid, or gas. Specially, it can gather high-spectral-resolution signals over a wide spectral range. Therefore, it would offer significantly wider information than a dispersive spectrometer. In this thesis work, FTIR maps were collected using a PerkinElmer Spotlight 400 equipped with a mercury cadmium tellurium (MCT) detector, which consists of single point (point mode) and 16-array (image mode) detectors all in one. Maps of 2 × 8 points (~200 × 100 μm^2 area) in reflectance mode were acquired at 4 cm^{-1} resolution with 16 scans per pixel from 4000 to 400 cm^{-1}. The drop down average true range (ATR) is determined by a Ge crystal 100 μm in diameter. Principal component analysis (PCA) is one of the most widely used methods for data reduction and exploratory analysis. In this work, PCA analyses of the selected FTIR regions corresponding to the 400 - 4000 cm^{-1} range were obtained to reveal the uniformity of the functional groups and solid electrolyte interphase (SEI) layer.

3.4.8. *In-operando* X-ray Diffraction (XRD)

XRD is a useful tool to study the phase structure as mentioned in 3.4.2. The reaction mechanism of the electrode during cycling is very important to help understand the volume changes, phase transitions, and structural stability. Ex-situ XRD could be used to study the discharge or charge products, although the possibly exposure to the air and the uncertain phase stability of the electrode may lead to unreliable results. In

terms of these concerns, *in-operando* measurements are an effective tool which reflects the phase transitions in real time during cycling. In this thesis work, a customized CR2032 coin cell was assembled for use in synchrotron X-ray powder diffraction (SXRPD) experiments, and the details of cell assembly can be found elsewhere[3]. Synchrotron X-ray powder diffraction (SXRPD) experiments were conducted on the Powder Diffraction beamline at the Australian Synchrotron. The wavelength of synchrotron radiation was determined to be 0.68899 Å using LaB_6 (Standard Reference Material SRM 660b).

3.4.9. *In-operando* Transmission X-ray Microscopy (TXM)

The *in-operando* TXM technique is a type of X-ray microscopy which relies on an X-ray beam that is focused down to one small spot and scan the surface of the sample thus offering the detailed information on morphology change during the electrochemical cycling. This characterization method is a combination of spectromicroscopy, imaging with spectral sensitivity, and microspectroscopy, recording spectra from very small spots. In this thesis work, *in-operando* transmission X-ray microscopy (TXM) measurements were carried out at the 01B1 beamline of the National Synchrotron Radiation Research Centre (NSRRC) in Hsinchu City, Taiwan. The light source operates with photon energy ranging between 8 and 11 keV. The X-rays passing through the tested coin cell go through a zone plate optical system and then a phase ring to form the image.

3.5. Theoretical calculations

Since the last century, starting with the 1970s, density functional theory (DFT) was very popular on the basis of solid-state physics. It is a commonly accepted method used to investigate electronic structures, especially in atoms, molecules, and condensed phases in substances, relying on computational quantum mechanical modelling methods. It has its name because it is calculated based on the functional of the electron density. In this thesis work, the calculations were performed based on the density functional theory (DFT) approach [4] using the DMol^3 package. The effects of the exchange correlation interaction were treated according to the Perdew-Burke-Ernzerhof generalized-gradient approximation (GGA-PBE) [5]. All-electron Kohn-Sham wave functions were expanded in a double numerical basis with polarized orbital (DNP) [6]. Sampling of the irreducible wedge of the Brillouin zone was performed with a regular Monkhorst-Pack grid of special k-points [7]. The convergence criteria for relaxation were 1.0×10^{-5} Ha, 0.002 Ha/Å, and 0.005 Å for the energy, gradient, and atomic displacement, respectively.

3.6. Electrochemical Measurements

3.6.1. Electrode Preparation and Half-Cell Assembly for PIBs

Electrodes were prepared by the slurry-mixing method and coated on the appropriate current collector such as copper foil. Briefly, after mixing the active materials,

conductive carbon, and binder with an optimized weight ratio, a compatible solvent is added during the grinding process to make a slurry. Then, the obtained slurry was uniformly coated on copper foil via a doctor blade and transferred into an oven to dry at 120 ℃ for 12 h under vacuum. After that, the electrode materials on the copper were pressed at a fixed pressure of around 2 MPa and cut into small pieces. Finally, the electrodes were transferred into a glove box under argon atmosphere and assembled in CR2032 coin-type cells (Figure 3.1) using potassium foil as the counter electrode. The electrolytes that were used were 0.8 M potassium hexafluorophosphate (KPF_6) or 1 M potassium bis(fluorosulfonyl)imide (KFSI) in a mixture of ethylene carbonate (EC) and diethyl carbonate (DEC) (1:1 by volume). In addition, fluoroethylene carbonate (FEC) was used as the additive (5 wt. %) to study the electrochemical performance in PIBs. For comparison purposes, lithium and sodium hexafluorophosphate ($NaPF_6$) in EC/DEC with sodium foil as counter electrode was adopted in LIBs and SIBs, respectively.

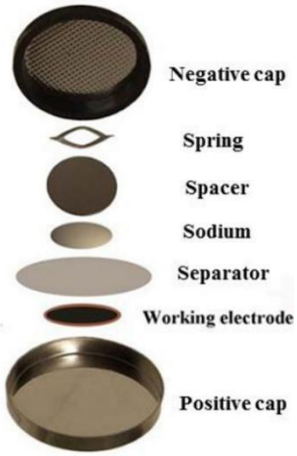

Figure 3.1 Schematic illustration of half-cell assembly using sodium as counter electrode.

3.6.2. Galvanostatic Charge-Discharge

Galvanostatic charge-discharge measurements are used to determine the electrochemical performance via a constant current density to test the specific capacity and cycling performance in a certain voltage window. Through the applied constant current and the test time, the discharge and charge capacity could be estimated in the cycling process. In this thesis work, the measurements were carried out on a Neware and Land battery test systems.

3.6.3. Cyclic Voltammetry (CV)

CV is an important tool to measure the relationship between current and voltage potential to evaluate the electrochemical polarization in cells. In a typical experiment, with a constant scanning rate, the working electrode's potential varies with the

positive and negative scans. Generally, the ramping cycles should be repeated several times to verify the initial changes in the oxidation and reduction peaks. The particular results are always dependent on the kind of solution because CV measurements are conducted on the basis of the electrolyte system. Therefore, this method is not only useful to study the electrode itself, but also a meaningful way to study the polarization and electrochemical behaviour of various electrolytes. In this thesis work, CV tests were conducted on a Biologic VPM3 electrochemical workstation in ISEM of UOW.

3.6.4. Electrochemical Impedance Spectroscopy (EIS)

EIS is normally used to investigate the electrochemical impedance in battery systems, including ohmic resistance and charge transfer resistance. Briefly, the first intercept with the Z'-axis represents the ohmic resistance, which is mainly affected by the electrolyte. The small semicircle at high frequency is regarded as due to the impedance of the solid-electrolyte interphase (SEI) layer (R_f), and the large semicircle at relatively lower frequency is assigned to the impedance generated by the charge transfer resistance (R_{ct}) and the electrical double-layer capacitance. The linear increase in impedance after the semicircles, referred to as the Warburg impedance, is caused by K^+ diffusion inside the particles [1]. In this thesis work, EIS data were collected on a Biologic VPM3 electrochemical workstation in ISEM of UOW.

3.7. References

[1] G. E. Lloyd, *Mineralogical Magazine* **1987**, 51, 3.

[2] J. Goldstein, D. E. Newbury, J.R, Michael, N.W.M. Ritchie, J. H. J. Scott, D. C. Joy, *Scanning electron microscopy and X-ray microanalysis: A text for biologists, materials scientists, and geologists*, Springer Science & Business Media, 2017. Published by Springer Nature.

[3] W. K. Pang, S. Kalluri, V. K. Peterson, N. Sharma, J. Kimpton, B. Johannessen, H. K. Liu, S. X. Dou, Z. Guo, *Chem. Mater.* **2015**, 27, 3150.

[4] P. Hohenberg, W. Kohn, *Physical Review* **1964**, 136, B864.

[5] J. P. Perdew, K. Burke, M. Ernzerhof, *Phys. Rev. Lett.* **1996**, 77, 3865.

[6] B. Delley, *The Journal of Chemical Physics* **1991**, 94, 7245.

[7] H. J. Monkhorst, J. D. Pack, *Physical review B* **1976**, 13, 5188.

Chapter 4
4. Sn_4P_3/C materials for advanced potassium-ion battery anode

4.1. Introduction

The demand for energy storage materials is high and increasing with the rapid development of electronic devices, electric vehicles, and large-scale energy storage system (ESS).[1-4] The widespread use of lithium-ion batteries (LIBs) for these applications is seriously limited by the uneven distribution and the short supplies of lithium minerals (0.0017 wt. %) around the world.[5] Sodium-ion batteries (SIBs) have recently attracted increasing interest due to the natural abundance of sodium.[6-8] Unfortunately, their relatively high standard hydrogen potential (-2.71 V vs. *E*°) compared to LIBs (-3.04 V vs. *E*°) makes the energy density of SIBs relatively low and limits their potential industrial applications.[6, 9-11]

Considering the similar positions of Li, Na, and K in the periodic table and the natural abundance of potassium[12-16], the potassium-ion battery (PIB) system could be considered as well. Since the standard hydrogen potential of K (-2.93 V vs. *E*°) is lower than that of Na and closer to that of Li, PIBs have potential as low-cost batteries with high energy density and high voltage.[17-20] Nevertheless, it is challenge to develop suitable electrodes to accommodate the large size of the K-ions (1.38 Å) compared to Na-ions and Li-ions. Carbonaceous materials have been investigated as

PIB anodes, although the highest reported capacity is 273 mA h g^{-1} for soft carbon at C/40.[13]

Although there have been few investigations of alloy-based anode materials in PIBs, an investigation of Sn/C composite anode in a PIB was recently reported, which delivered only 150 mA h g^{-1} after 30 cycles at a current density of 25 mA g^{-1},[21] not much better than for carbon anode materials. Phosphorus (P) has a high theoretical capacity of 2594 mA h g^{-1}, since it can form K_3P, a binary phase with K.[22]

Herein, the electrochemical performance of P/C and Sn_4P_3/C composites as anode materials for PIBs were investigated. The P/C anode delivered a high capacity, but it decayed very fast. In contrast, the Sn_4P_3/C electrode delivered a reversible capacity of 384.8 mA h g^{-1} at a current density of 50 mA g^{-1} and good rate capability of 221.9 mA h g^{-1}, even at a current density of 1 A g^{-1}, the best electrochemical performance reported so far for any anode material for PIBs. Moreover, the reduction potential of the Sn_4P_3 electrode in the PIBs was measured to be 0.1 V, higher than its 0.01 V in SIBs. The K-alloy reactions thus occur at a higher potential than the Na-alloy reactions, so that the PIBs with the Sn_4P_3/C electrode will have a lower risk of short-circuiting due to dendrite growth.

4.2. Experimental Section

4.2.1. Preparation of Sn_4P_3/C binary composites

Sn_4P_3/C powder was synthesized by a ball-milling process using elemental Sn (Aldrich, ≥ 99.8%), red phosphorus (Aldrich, ≥ 99%), and carbon black as the raw

materials in the weight ratio of Sn: P: C = 73.1: 14.4: 12.5 (with Sn and P in the molar ratio of 4:3, respectively). The ball milling was conducted in a planetary QM-1SP2 ball mill for 30 h, and the elemental mixture was milled at 500 rpm using stainless steel balls of 10 mm in diameter and with a powder-to-ball weight ratio of 1:30. For comparison, Sn/C and P/C were also synthesized under the same conditions with the weight ratios Sn: C = 87.5: 12.5 and P: C = 87.5: 12.5, respectively. All sample storage and handling were performed in an Ar filled glove box (MBraun Unilab).

4.2.2. Materials characterization

The crystal structures of the as-prepared powders were characterized by powder X-ray diffraction (XRD) on a GBC MMA diffractometer with a Cu K_α source at a scanning rate of $1\,^\circ\,min^{-1}$. Raman spectra were collected on a JobinYvon HR800 Raman spectrometer. X-ray photoelectron spectroscopy (XPS) was conducted on a VG Multilab 2000 (VG Inc.) photoelectron spectrometer using monochromatic Al Kα radiation under the vacuum of 2×10^{-6} Pa. The morphology of the synthesized powders was characterized on a JEOL JSM-7500FA field-emission scanning electron microscope (FESEM) and a JEOL ARM-200F cold-field-emission and aberration-corrected transmission electron microscope (TEM).

4.2.3. Electrochemical measurements

Electrodes were fabricated using a slurry-coating method. The synthesized materials (Sn_4P_3/C, Sn/C, and P/C) were mixed with Super P carbon black and carboxymethyl

cellulose (CMC) in the weight ratio of 8:1:1, respectively. Deionized (DI) water was used as the dispersing agent. Then, the slurry was coated on copper foil and dried in a vacuum oven at 80 ℃ overnight. Coin-type (CR2032) cells were assembled in an argon-filled glove box with oxygen and water content lower than 0.1 ppm. K half-cells were assembled with potassium metal and 0.8 M KPF_6 in an ethylene carbonate (EC) − diethyl carbonate (DEC) solution (EC: DEC = 1:1) as electrolyte. Na half-cells were assembled with sodium metal and 0.8 M $NaPF_6$ in EC-DEC solution (EC: DEC = 1:1) as electrolyte. The mass loading of active material (Sn_4P_3) was over 0.78 mg cm^{-2}, corresponding to a total mass loading of 1.11 mg cm^{-2}. Cyclic voltammetry (CV) tests were conducted on a VMP-3 electrochemical workstation at a scan rate of 0.05 mV s^{-1}. The cells were galvanostatically charged-discharged between 0.01 and 2.0 V versus K/K^+ or Na/Na^+ at various current densities on a Land battery tester. The specific capacity was calculated based on the weight of Sn_4P_3. The mass loading of active material was increased to over 1.7 mg cm^{-2} for ex-situ XRD experiments.

4.3. Results and Discussion

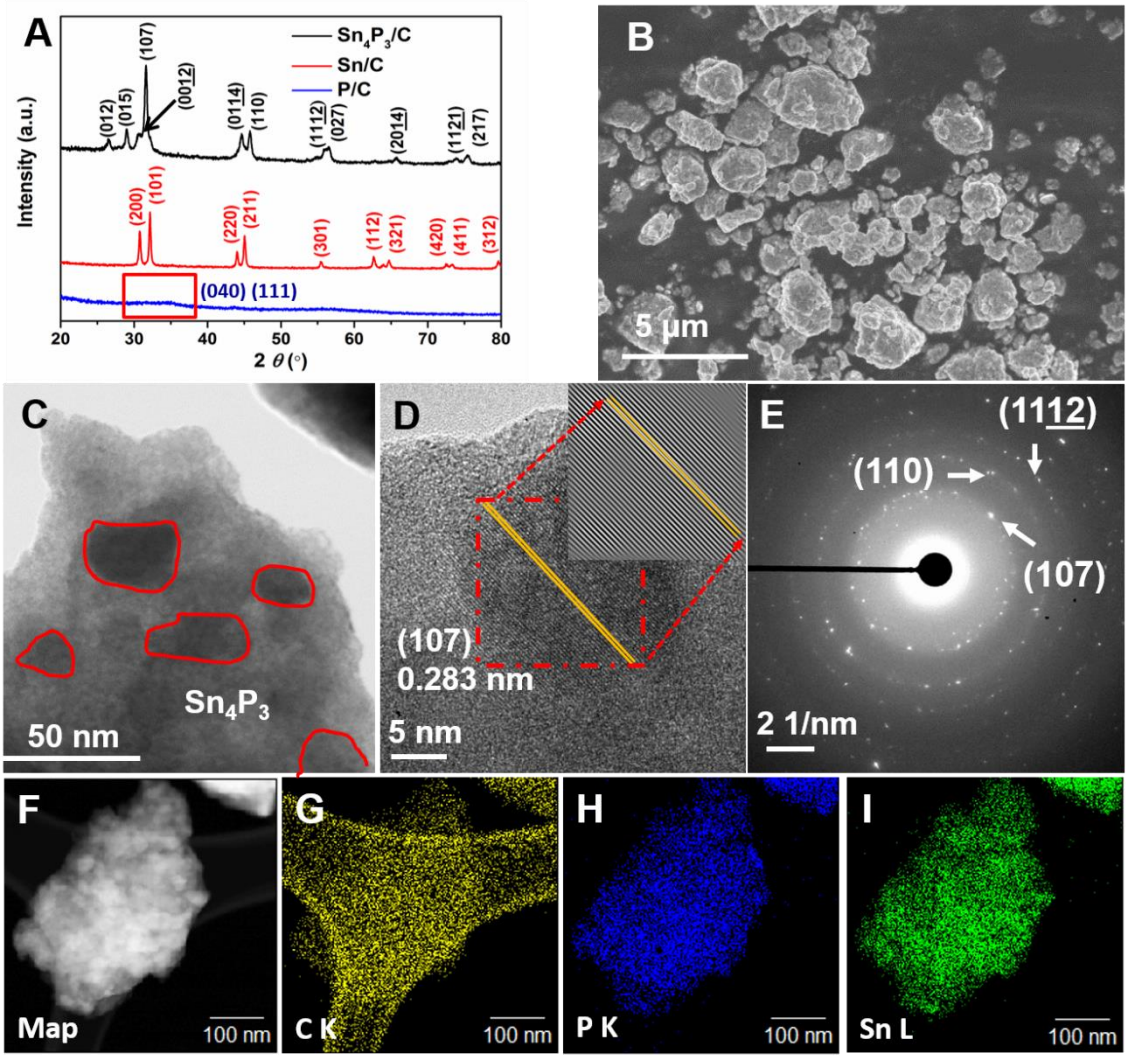

Figure 4.1. Characterization of Sn_4P_3 powder: (A) XRD pattern compared with Sn/C and P/C, (B) FESEM image, (C) TEM image, with the red outlines indicating the Sn_4P_3 nanoparticles, (D) HRTEM image and FFT pattern of the red area (inset), (E) SAED pattern, and (F-I) EDS maps of Sn_4P_3/C powder.

Figure 4.1A shows the X-ray diffraction (XRD) patterns of the as-prepared Sn_4P_3/C,

Sn/C, and P/C powders ball milled under the same conditions. All the diffraction peaks in the XRD pattern of the Sn_4P_3/C composite and the as-prepared sample is virtually pure Sn_4P_3 (ICSD No. 15014). Figures 4.1B-I display field-emission scanning electron microscopic (FESEM) and transmission electron microscopic (TEM) images of the Sn_4P_3/C powder. The powder mainly consists of irregular agglomerated micrometre sized particles, as shown in Figure 4.1B. The agglomerated microparticles consist of many crystalline nanoparticles around 20-50 nm, distributed evenly in the amorphous carbon matrix (Figure 4.1C and D). Figure 4.1D shows the lattice fringes of the (107) planes of Sn_4P_3, and the spacing of the fringes is 0.283 nm, which matches the d_{107} spacing of Sn_4P_3. The selected area electron diffraction (SAED) pattern and high resolution TEM (HRTEM) image clearly demonstrate that the Sn_4P_3 nanoparticles are uniformly distributed in the amorphous carbon matrix, which could act as a buffer to suppress the volume changes during the potassiation/depotassiation. Figure 4.1F-I presents energy dispersive spectroscopy (EDS) elemental mapping images of a nano-Sn_4P_3 particle with uniform distributions of the Sn, P, and C. Raman spectroscopy was used to identify the carbon black in the three samples, as shown in Figure 4.2A. The two peaks at 1355 cm^{-1} and 1580 cm^{-1} correspond to the disordered (D) band and the graphitic (G) band of carbon black, respectively. The X-ray photoelectron spectroscopy (XPS) results for the Sn_4P_3/C composite are presented in Figure 4.2B-D and they show a metallic feature (Sn) and metal phosphide for the P component. This explains the high electrical conductivity of Sn_4P_3 (30.7 S cm^{-1} for

Sn_4P_3 vs. 3.5 × 10^{-5} S cm^{-1} for P/C composite).[23-24] No chemical bonding between carbon and P or Sn is evidenced by the XPS results.

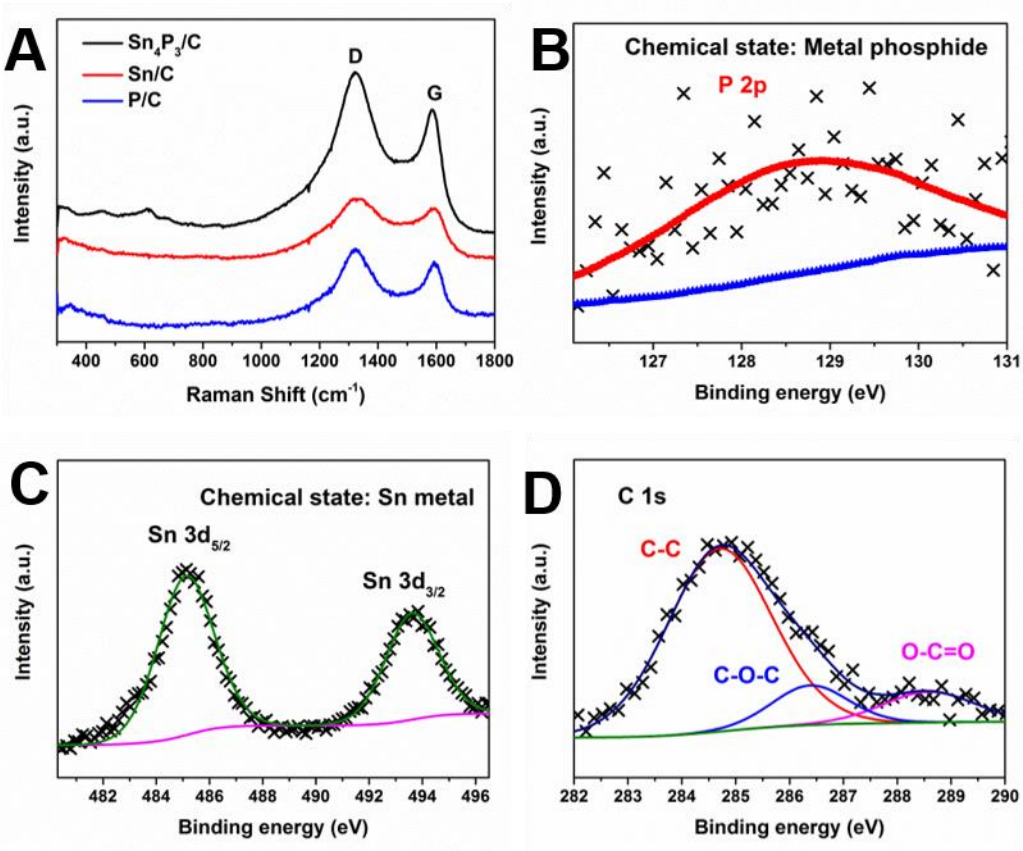

Figure 4.2. **(**A) Raman spectra of the as-prepared Sn_4P_3/C, Sn/C, and P/C powders. XPS analysis of (B) P 2p, (C) Sn 3d, and (D) C 1s peaks from Sn_4P_3/C powder.

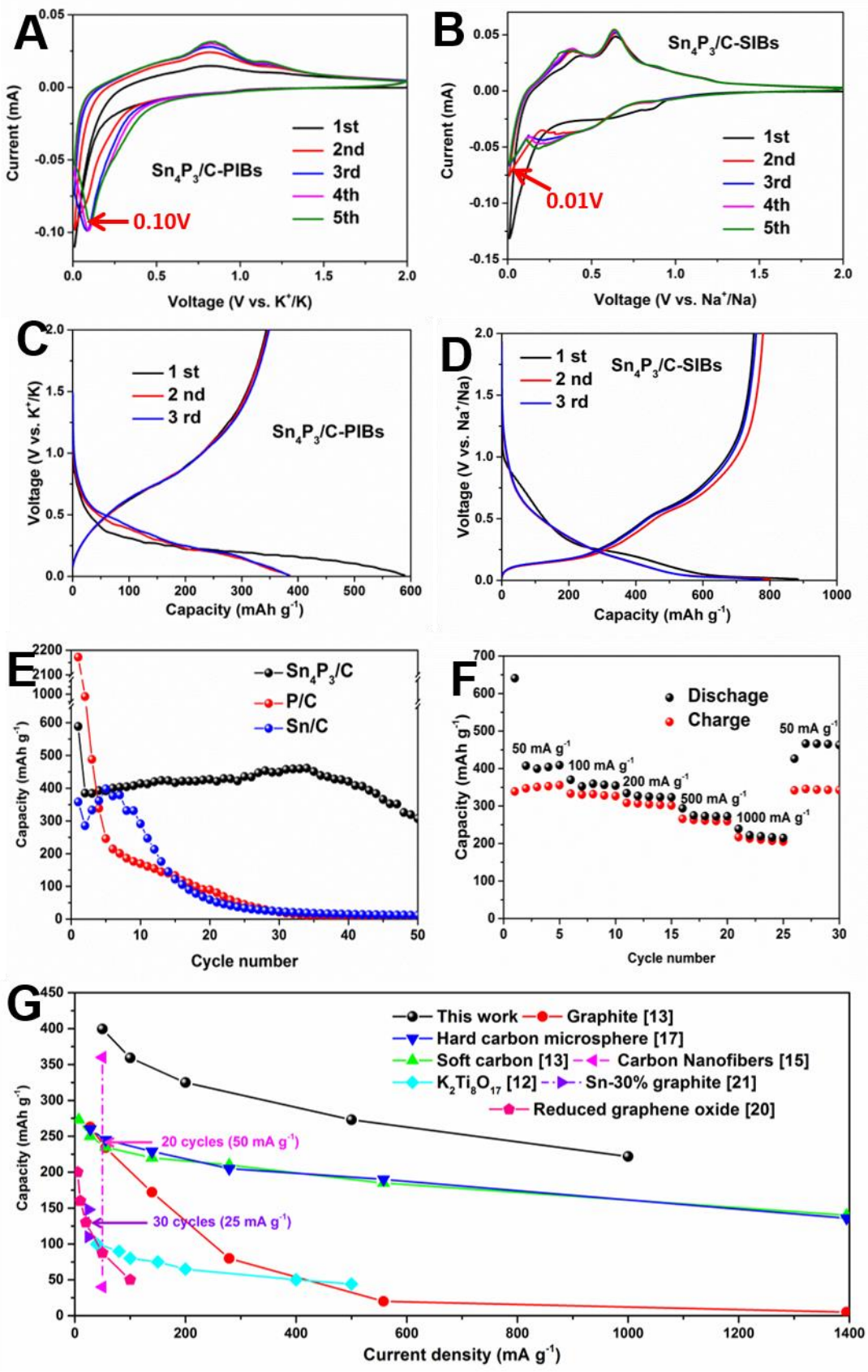
A
Current (mA)
Voltage (V vs. K+/K)
Sn4P3/C-PIBs
0.10V
1st
2nd
3rd
4th
5th
B
Sn4P3/C-SIBs
0.01V
Voltage (V vs. Na+/Na)
C
Voltage (V vs. K+/K)
Capacity (mAh g-1)
1 st
2 nd
3 rd
D
Voltage (V vs. Na+/Na)
E
Sn4P3/C
P/C
Sn/C
Capacity (mAh g-1)
Cycle number
F
Dischage
Charge
50 mA g-1
100 mA g-1
200 mA g-1
500 mA g-1
1000 mA g-1
G
This work
Graphite [13]
Hard carbon microsphere [17]
Soft carbon [13]
Carbon Nanofibers [15]
K2Ti8O17 [12]
Sn-30% graphite [21]
Reduced graphene oxide [20]
20 cycles (50 mA g-1)
30 cycles (25 mA g-1)
Current density (mA g-1)

Figure 4.3. Cyclic voltammograms (CVs) for the first 5 cycles of (A) Sn_4P_3/C in PIBs and (B) Sn_4P_3/C in SIBs at the scanning rate of 0.05 mV s^{-1}. The initial, second, and third discharge/charge profiles of (C) Sn_4P_3/C in PIBs and (D) Sn_4P_3/C in SIBs at the current density of 50 mA g^{-1}. (E) Cycling performance of the Sn_4P_3/C, Sn/C, and P/C electrodes in PIBs at the current density of 50 mA g^{-1}. (F) Rate performance of Sn_4P_3/C electrode in PIBs at various current densities from 50 mA g^{-1} to 1000 mA g^{-1}. (G) Rate capacities of the Sn_4P_3/C anode and the other reported anodes in PIBs.

The K-ion storage behavior of the Sn_4P_3/C electrode was investigated by cyclic voltammetry (CV) and compared with its performance in SIBs (Figure 4.3A and B). For the PIBs (Figure 4.3A) a major peak at around 0.01 V was observed in the initial cathodic scan. During the subsequent cycles, this large reduction band was shifted to 0.1 V. In the anodic scan, two oxidation bands centered at 0.8 and 1.15 V due to the depotassiation processes of K-Sn and K-P can be observed. The lowest reduction peak for the Sn_4P_3/C electrode (Figure 4.3B) is at 0.1 V versus K^+/K and 0.01 V versus Na^+/Na, respectively. Considering the fact that dendrite formation becomes more serious when the reduction potential is close to the plating potential, PIBs could be safer than SIBs when using Sn_4P_3 as anode. The discharge and charge profiles of the Sn_4P_3/C electrodes for PIBs and SIBs are compared and shown in Figures 4.3C and 4.3D. The discharge slopes for the Sn_4P_3/C electrode are around 0.1-0.6 V for the PIBs and 0.01-0.5 V for the SIBs, respectively.

Figure 4.3E displays the cycling performances of the Sn_4P_3/C, P/C, and Sn/C electrodes in PIBs at the current density of 50 mA g^{-1}. The first discharge capacity of the Sn_4P_3/C electrode (588.7 mA h g^{-1}) is higher than that of the Sn/C (358.2 mA h g^{-1}) but lower than that of the P/C (2171.7 mA h g^{-1}). The P/C and Sn/C electrodes only managed to retain 9% and 20%, respectively, of their reversible capacity after 20 cycles. In contrast, the Sn_4P_3/C electrode shows much better cycling performance compared with the P/C and Sn/C electrodes, where the capacity increased gradually up to 30 cycles and faded gradually after that. Nevertheless, the Sn_4P_3/C electrode still retained the capacity of 307.2 mA h g^{-1} after 50 cycles, which is almost 80% of its reversible capacity. Long-term cycling performance was displayed in Figure 4.4. After 50 cycles, the capacity of the Sn_4P_3/C decreases very rapidly. The fast capacity drop is mainly due to the large particle size and the non-uniform distribution of Sn_4P_3 particles in the carbon black due to the limitations of the ball-milling technique. Figure 4.5A and 4.5B present digital photographs of separators after the 1st cycle and the 50th cycle. After 50 cycles, many particles have fallen off the copper foil, which will cause a huge loss of active materials and carbon, as well as leading to capacity loss.

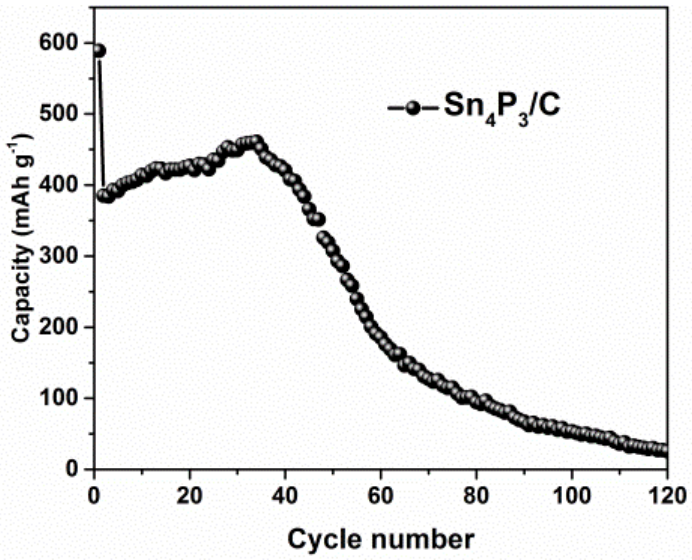

Figure 4.4. Long-term cycling performance of the Sn_4P_3/C electrode in PIBs at the current density of 50 mA g^{-1}.

Figure 4.5. Digital photographs of separator after (A) the 1st cycle and (B) the 50th cycle.

TEM and SEM were carried out on the cycled samples to show the morphology and microstructure changes, as shown in Figures 4.6 and 4.7, respectively. The nano-Sn_4P_3 particles are still intact in the crystalline state (Figure 4.6) but become smaller in size (5-8 nm) after 30 cycles. Their even distribution

within the carbon matrix provides effective electrode/electrolyte contact, short ionic diffusion paths, and improved reaction kinetics, [25] so that they contribute to the gradual capacity rise before the 30th cycle. After the 50th cycle, the original crystalline particles were decrystallized and agglomerated into larger globules, and the cracks in the Sn_4P_3/C electrode become much bigger during the cycling process (Figure 4.7), mostly after 30 cycles, indicating large strain caused by large volume changes in the Sn_4P_3 electrode during cycling, and loss of integrity of the electrode due to particle pulverization leads to decreased capacity.

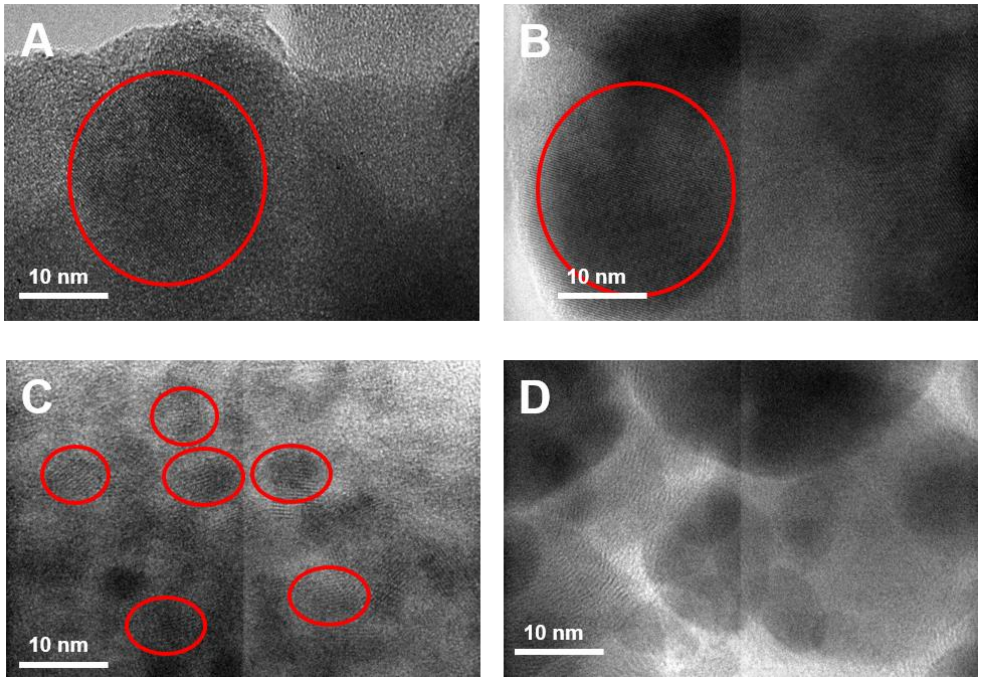

Figure 4.6. Ex-situ TEM images of Sn_4P_3/C electrodes: (A) pristine, and after (B) the 10th cycle, (C) the 30th cycle, and (D) the 50th cycle. The red circles identify the Sn_4P_3 nanoparticles in the carbon matrix.

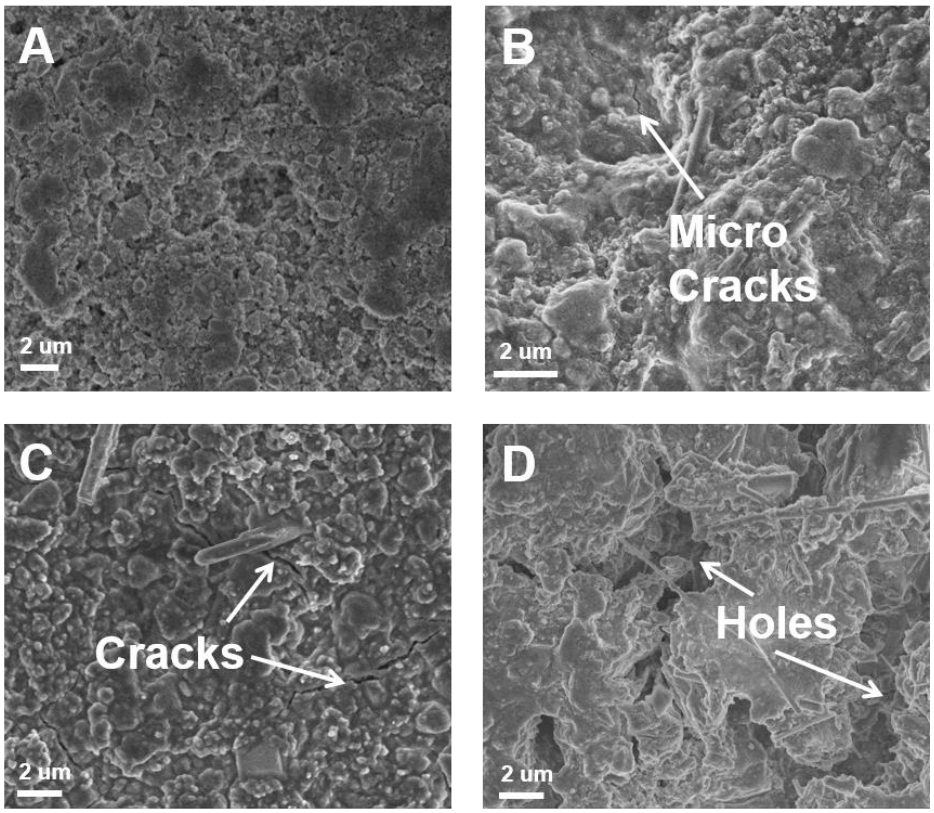

Figure 4.7. Ex-situ FESEM images of Sn_4P_3/C electrodes: A) pristine, and after B) the 10^{th} cycle, C) the 30^{th} cycle, and D) the 50^{th} cycle.

The rate capability of the Sn_4P_3/C electrode in PIBs was also characterized, as shown in Figure 4.3F. The potassiation capacity decreased from 399.4 to 221.9 mA h g^{-1} when the current density increased from 50 mA g^{-1} to 1000 mA g^{-1}. The rate capacities of all the reported anodes used in PIBs (graphite, soft carbon,[13] hard carbon microsphere,[17] carbon nanofibers,[15] Sn/C composite,[21] reduced graphene oxide,[20] and $K_2Ti_8O_{17}$[12]) are presented in Figure 4.3G. It is clear that the rate capability of the Sn_4P_3/C electrode is the best among the reported anode materials.

To understand the possible reaction mechanisms during the discharge and charge

processes, ex-situ XRD was used to identify the possible phases. As shown in Figure 4.8A, after the Sn_4P_3/C electrode was discharged to 0.4 V, XRD signals from the Sn_4P_3 electrode decreased notably, and XRD signals from $K_{3-x}P$ could be detected. When the Sn_4P_3/C electrode was further discharged to 0.2 V, Sn phase appeared and became the main phase at the expense of the Sn_4P_3, indicating a conversion reaction. Meanwhile, several new peaks of K_4Sn_{23} (ICSD No. 25301) were observed. After the Sn_4P_3/C electrode was discharged to 0.01 V, KSn phase (ICSD No. 409435) and minor Sn peaks could be detected, indicating the alloying of potassium with tin. The same results were also obtained in the Sn/C anode, where K_4Sn_{23} and KSn phases were also observed after discharging to 0.2 and 0.01 V, as shown in Figure 4.8B. It is well known that the binary K-P system has the following phases: KP (ICSD No. 14010), K_4P_3 (ICSD No. 64625), K_3P_{11} (ICSD No. 36590), and K_3P (ICSD No. 25550).[22] As for the cycled P/C electrodes, which were discharged to 0.5 or 0.01 V (Figure 4.8C), two new peaks in addition to the peaks of copper were detected at 25.38° and 65.91°, which correspond to the (102) and (116) of the layered structured K_3P phase with space group $P6_3/mmc$ (Figure 4.9). The strongest peak of K_3P is missing, possibly due to partial potassiation, so the final discharge product could be a non-stoichiometric $K_{3-x}P$ compound or amorphous. Based on this discussion, I believe that KSn and $K_{3-x}P$ are the two possible final products after the discharge of the Sn_4P_3/C electrode in PIBs, with the theoretical capacity of Sn_4P_3 as high as 620 mA h g^{-1}, which is more than 2 times the capacity of carbon anode materials. In the charging

process, a new peak at 31.4° was detected after charging to 2.0 V, representing the reformation of the Sn_4P_3. Therefore, the potassiation/depotassiation of Sn_4P_3 via conversion and alloying reactions is partially reversible. The reaction mechanism of Sn_4P_3 as anode material for SIBs was previously thoroughly investigated, and in some cases, the Sn_4P_3 phase was found to be restored as well, even after desodiation at 1.5 V.[26] Accordingly, the potassiation and depotassiation mechanism may be described by the following equations:

$$Sn_4P_3 + (9-3x)\,K \leftrightarrow 4Sn + 3K_{3-x}P \quad (1)$$

$$23Sn + 4K \leftrightarrow K_4Sn_{23} \quad (2)$$

$$K_4Sn_{23} + 19K \leftrightarrow 23KSn \quad (3)$$

To present the reaction products at different potentials clearly, the data are listed in Table 4.1:

Table 4.1. Reaction products of Sn_4P_3 during discharge/charge process.

Sn_4P_3/C electrode	Reaction products
Discharged to 0.4 V	$Sn_4P_3 + Sn + K_{3-x}P$
Discharged to 0.2 V	$Sn_4P_3 + Sn + K_{3-x}P + K_4Sn_{23}$
Discharged to 0.01 V	$Sn + K_{3-x}P + K_4Sn_{23} + KSn$
Charged to 0.6 V	$Sn + K_{3-x}P + K_4Sn_{23} + KSn$
Charged to 2.0 V	$Sn + K_4Sn_{23} + Sn_4P_3$

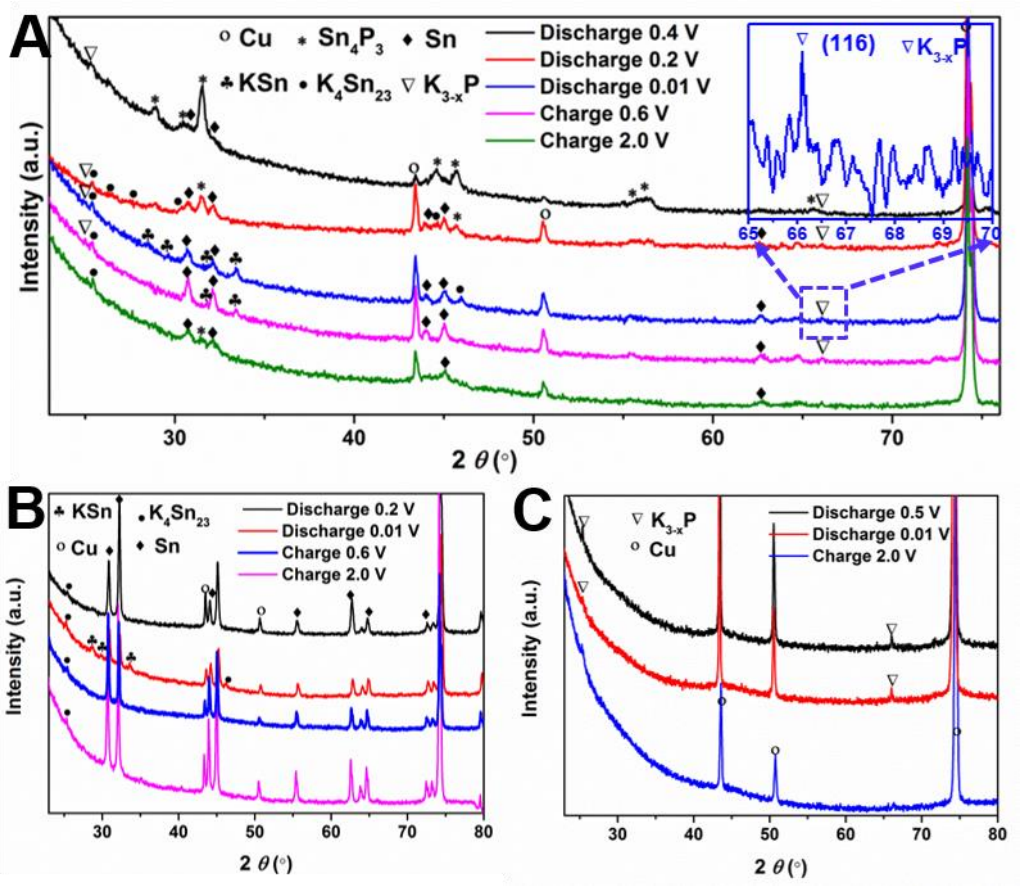

Figure 4.8. Ex-situ XRD patterns of cycled (A) Sn_4P_3/C and enlarged area (65˚-70˚) at 0.01 V at discharged potential (inset), (B) Sn/C, and (C) P/C electrodes in PIBs at different potentials.

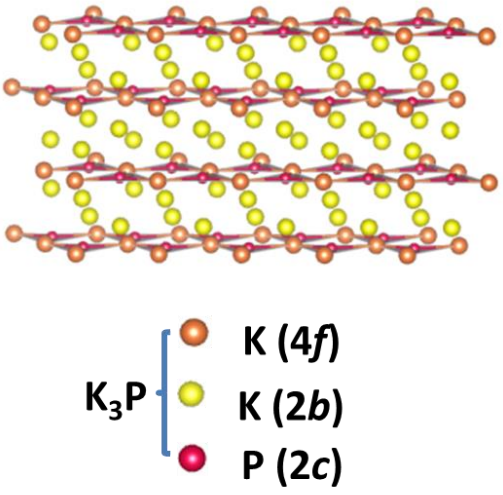

Figure 4.9. Schematic diagrams of the crystal structure of K_3P

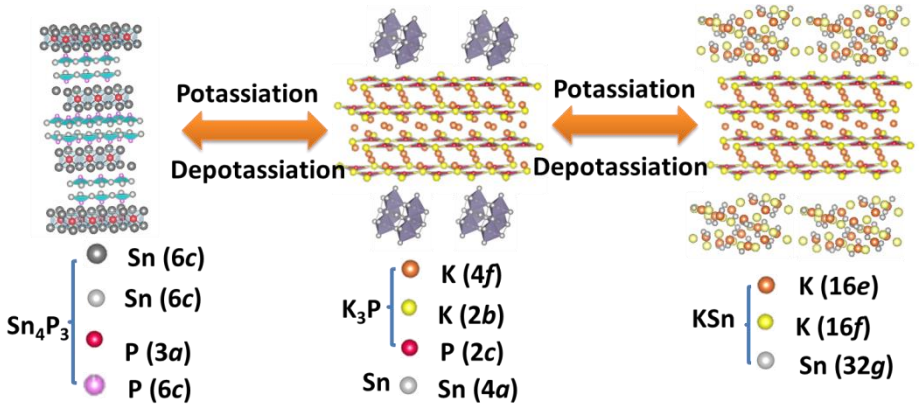

Figure 4.10. The potassiation/depotassiation process in Sn_4P_3/C electrode.

The superior electrochemical performance of the Sn_4P_3/C composite compared to Sn/C and P/C can be firstly understood from the active nature of the Sn_4P_3 itself, where the Sn and P components in the Sn_4P_3/C are combined to give a synergistic K-storage reaction. The reaction mechanism of Sn_4P_3 during potassiation/depotassiation is schematically shown in Figure 4.10. Upon potassiation, a conversion reaction first occurs, where the Sn_4P_3 breaks into small Sn particles and a $K_{3-x}P$ matrix (Reaction (1)). Upon further potassiation, K is inserted into Sn to first form K_4Sn_{23} (Reaction (2)) and finally KSn (Reaction (3)) through the alloying reaction. During the depotassiation, KSn dealloys first to form Sn, and then the Sn reacts with $K_{3-x}P$ to convert it back to Sn_4P_3. Thus, the stepped formation of K-Sn (K_4Sn_{23}, KSn) and K-P alloy ($K_{3-x}P$) phases during the discharge process creates mutual buffers to alleviate

the volume changes during cycling. The conductive carbon matrix provides a further buffering effect against volume changes during cycling, thus maintaining the integrity of the electrode and enhancing the electrical conductivity, leading to improved cycling stability of the electrode.

4.4. Conclusion

In summary, Sn_4P_3/C composite, introduced for the first time as an anode material for the potassium-ion battery was synthesised by a conventional and scalable ball-milling technique. Compared with Sn_4P_3/C in SIBs, Sn_4P_3/C electrode in PIBs could deliver a discharge voltage plateau (0.1 V) that is low enough for an anode, but slightly higher than the plating potential of the corresponding metal (0.01 V), thus avoiding the formation of dendrites and improving the safety of the battery. The investigation of the reaction mechanisms of the Sn_4P_3 indicates that K-Sn (K_4Sn_{23}, KSn) and K-P alloy ($K_{3-x}P$) phases are formed during the discharge process, with these phases acting as mutual buffers to alleviate the volume changes during cycling. The conductive carbon matrix enhances the electrical conductivity of the electrode and works as a buffer matrix to accommodate the volume changes in the active materials during cycling, maintaining the integrity of the electrode and the cycle life. This work may help in the search for a safe, high-energy-density, and low-cost rechargeable K-ion battery for large-scale energy storage applications.

4.5. References

[1] D. P. Dubal, O. Ayyad, V. Ruiz, P. Gomez-Romero, *Chemical Society Reviews* **2015**, 44, 1777.

[2] D. Larcher, J. Tarascon, *Nature chemistry* **2015**, 7, 19.

[3] Y. Xie, M. Naguib, V. N. Mochalin, M. W. Barsoum, Y. Gogotsi, X. Yu, K.-W. Nam, X.-Q. Yang, A. I. Kolesnikov, P. R. Kent, *Journal of the American Chemical Society* **2014**, 136, 6385.

[4] F. Wu, Y. Xing, X. Zeng, Y. Yuan, X. Zhang, R. Shahbazian‐Yassar, J. Wen, D. J. Miller, L. Li, R. Chen, *Advanced Functional Materials* **2016**, 26, 7626.

[5] J. B. Goodenough, K.-S. Park, *Journal of the American Chemical Society* **2013**, 135, 1167.

[6] N. Yabuuchi, K. Kubota, M. Dahbi, S. Komaba, *Chemical reviews* **2014**, 114, 11636.

[7] M. Dahbi, N. Yabuuchi, K. Kubota, K. Tokiwa, S. Komaba, *Physical Chemistry Chemical Physics* **2014**, 16, 15007.

[8] C. Chen, Y. Wen, X. Hu, X. Ji, M. Yan, L. Mai, P. Hu, B. Shan, Y. Huang, *Nature Communications* **2015**, 6, 6929.

[9] D. Kundu, E. Talaie, V. Duffort, L. F. Nazar, *Angewandte Chemie International Edition* **2015**, 54, 3431.

[10] V. Palomares, M. Casas-Cabanas, E. Castillo-Martínez, M. H. Han, T. Rojo, *Energy & Environmental Science* **2013**, 6, 2312.

[11] S. Y. Hong, Y. Kim, Y. Park, A. Choi, N.-S. Choi, K. T. Lee, *Energy & Environmental Science* **2013**, 6, 2067.

[12] J. Han, M. Xu, Y. Niu, G.-N. Li, M. Wang, Y. Zhang, M. Jia, C. ming Li, *Chemical Communications* **2016**, 52, 11274.

[13] Z. Jian, W. Luo, X. Ji, *Journal of the American Chemical Society* **2015**, 137, 11566.

[14] Q. Zhao, J. Wang, Y. Lu, Y. Li, G. Liang, J. Chen, *Angewandte Chemie* **2016**, 128, 12716.

[15] Y. Liu, F. Fan, J. Wang, Y. Liu, H. Chen, K. L. Jungjohann, Y. Xu, Y. Zhu, D. Bigio, T. Zhu, *Nano letters* **2014**, 14, 3445.

[16] C. D. Wessells, S. V. Peddada, R. A. Huggins, Y. Cui, *Nano letters* **2011**, 11, 5421.

[17] Z. Jian, Z. Xing, C. Bommier, Z. Li, X. Ji, *Advanced Energy Materials* **2016**, 6, 1501874.

[18] A. Eftekhari, Z. Jian, X. Ji, *ACS Applied Materials & Interfaces* **2016**, 9, 4404.

[19] J. Zhao, X. Zou, Y. Zhu, Y. Xu, C. Wang, *Advanced Functional Materials* **2016**, 26, 8103.

[20] W. Luo, J. Wan, B. Ozdemir, W. Bao, Y. Chen, J. Dai, H. Lin, Y. Xu, F. Gu, V. Barone, *Nano letters* **2015**, 15, 7671.

[21] I. Sultana, T. Ramireddy, M. M. Rahman, Y. Chen, A. M. Glushenkov, *Chemical Communications* **2016**, 52, 9279.

[22] J. M. Sangster, *Journal of phase equilibria and diffusion* **2010**, 31, 68.

[23] J. Liu, P. Kopold, C. Wu, P. A. van Aken, J. Maier, Y. Yu, *Energy & Environmental Science* **2015**, 8, 3531.

[24] Y. Kim, Y. Park, A. Choi, N. S. Choi, J. Kim, J. Lee, J. H. Ryu, S. M. Oh, K. T. Lee, *Advanced Materials* **2013**, 25, 3045.

[25] X. Li, M. Rui, J. Song, Z. Shen, H. Zeng, *Advanced Functional Materials* **2015**, 25, 4929.

[26] J. Mao, X. Fan, C. Luo, C. Wang, *ACS applied materials & interfaces* **2016**, 8, 7147.

Chapter 5

5. Understanding high-energy density Sn_4P_3 anodes for Potassium Ion Batteries

5.1. Introduction

The increasing development and demands arising from consumer electrical transportation and large-scale energy storage call for high-energy density and low-cost batteries [1-3]. Despite the successful commercial application of lithium ion batteries (LIBs), the high cost of lithium minerals due to short supplies (0.0017 wt. %) makes it impossible to meet global energy requirements in the long run [4-5]. Widespread research interest in sodium ion batteries (SIBs) has recently been growing due to the natural abundance of sodium, but the relatively low energy density caused by the high standard hydrogen potential (-2.71 V vs. E^0) hinders its practical development [6].

Potassium, with abundant resources around the world and a low standard hydrogen potential (-2.93 V vs. E^0), close to that of lithium (-3.04 V vs. E^0), makes the potassium ion battery (PIB) an alternative candidate to replace the lithium ion batteries in large-scale energy storage applications [7-8]. Nevertheless, critical problems related to the large volume changes during electrochemical cycling remain a challenge due to the large size of the potassium ions (1.38 Å)[9]. Although carbon-based electrode materials for the potassium ion battery, especially amorphous carbon,

have recently been reported with outstanding cycling performance, even at high current rates, their low energy density because of their high operating voltage plateau is still a fatal obstacle[10-11]. Considering the non-carbon-based electrode materials, phosphorus-based anode material is an excellent candidate due to its having the highest theoretical capacity among the reported anode materials[12]. To date, several dominant synthesis routes have been reported, including ball-milling[13], hydrothermal[14], and solid-state[15] processes. The phosphide anode materials prepared via the hydrothermal method exhibit good electrochemical performance, although the synthesis is relatively complicated and it is hard to obtain the pure phase, which makes it difficult to scale up for industrial applications. Solid state synthesis will unavoidably produce white phosphorus due to the high temperature treatment, which is chemically unstable at room temperature. Therefore, ball milling is still the most practical technique for the mass production of phosphides with high purity. Guo et al. previously reported a phosphorus-based compound (Sn_4P_3) as anode material, which was synthesized by the ball-milling method and showed very high capacity [16]. It suffered from severe capacity fading after only 35 cycles, however, due to the relatively large particle size and non-uniform distribution of Sn_4P_3 [16]. Meanwhile, the electrolyte employed is still not fully optimized and further study on the electrochemistry, including the reaction mechanisms, solid-electrolyte interphase (SEI) layer formation, and potassium dendrite growth during cycling, is still needed to fully understand the P-based anode materials and design of a full K ion battery for

commercial applications.

To address the above issues, herein, we used carbon fibre to confine ball-milled Sn_4P_3 particles to improve the cycling stability of Sn_4P_3 anode. The carbon fibres can effectively accommodate the expansion of Sn and P during potassiation, and enhance the integrity and stability of the electrode, thereby achieving excellent cycling performance. In addition, the carbon fibres as a conductive matrix provide a large accessible area for the electrolyte and good transport kinetics for both electrons/ions. Potassium bis(fluorosulfonyl)imide (KFSI) and fluoroethylene carbonate (FEC) additive were chosen to optimize the electrochemical performance. The growth of potassium dendrites and the formation of an SEI layer during cycling were also investigated in various electrolytes with different potassium salts and FEC. We found that KFSI can efficiently suppress the growth of potassium dendrites and avoid the excessive side reactions caused by electrolyte decomposition, whereas FEC as additive could slow down the reaction dynamics in PIBs. Sn_4P_3@carbon fibre with KFSI in ethylene carbonate (EC) / diethyl carbonate (DEC) electrolyte delivered a reversible capacity of 403.1 mA h g^{-1} after 200 cycles at 50 mA g^{-1}, achieving high capacity retention of over 80% and long-term cycling capability, with capacity of 160.7 mA h g^{-1} after 1000 cycles at 500 mA g^{-1}. The reaction mechanism of Sn_4P_3 as anode for PIBs was further investigated by *in-operando* synchrotron x-ray diffraction (XRD).

5.2. Experimental Section

5.2.1. Sn_4P_3@carbon fibre fabrication

Sn_4P_3 powder was synthesized by a ball-milling process using elemental Sn (Sigma, ≥ 99.8%) and red phosphorus (Sigma, ≥ 99%) as the raw materials in the weight ratio of Sn:P = 83.6: 16.4 (with Sn and P in the molar ratio of 4:3, respectively). The ball milling was conducted in a planetary QM-1SP2 ball mill for 30 hr, and the elemental mixture was milled at 500 rpm using stainless steel balls 10 mm in diameter and with a powder-to-ball weight ratio of 1:30. PAN (Sigma, Mn = 100 kDa) was dissolved in DMF at a concentration of 10 % (w/v), and the desired amount of Sn_4P_3 (10, 20, 30, and 40 wt. %, relative to the polymer content) was added into the solution, which was placed in an ultrasound bath (Bandelin, Sonorex Super RK106) for 6 hr to promote cluster destruction and enhance the homogeneous dispersion of the filler in the polymer solution. Afterwards, the solution was transferred to a magnetic stirrer to achieve complete polymer dissolution. The nanocomposite solution was then placed in a glass syringe fitted with a steel needle with an inner diameter of 0.5 mm. Electrospinning was conducted with an electric field of 1.75 kV cm^{-1}, applied with a high voltage power supply from Gamma High Voltage. A syringe pump (from KD Scientific) was used to feed the polymer solutions into the needle tip at 0.5 mL h^{-1}. The electrospun non-woven meshes were collected on a static aluminium plate placed at 15 cm from the needle tip. The obtained electrospun membranes were first stabilized in argon at 250℃ for 2 hr with a heating rate of 10℃ min^{-1}, followed by a

carbonization process at 600℃ for 5 hr, with a heating rate of 5℃ min^{-1} under an argon atmosphere.

5.2.2. Characterization

The crystal structures of the as-prepared powders were characterized by XRD on a GBC MMA diffractometer with a Cu K_α source at a scanning rate of 1 °min^{-1}. Raman spectra were collected on a JobinYvon HR800 Raman spectrometer. XPS was conducted on a VG Multilab 2000 (VG Inc.) photoelectron spectrometer using monochromatic Al Kα radiation under vacuum of 2×10^{-6} Pa. The morphology of the synthesized powders was characterized on a JEOL JSM-7500FA field emission SEM (FESEM) and a JEOL ARM-200F aberration-corrected TEM. A customized CR2032 coin cell was made for use in synchrotron X-ray powder diffraction (SXRPD) experiments, and the details of cell assembly can be found elsewhere [17]. The cell was galvanostatically discharged and charged over 0.1–1.5 V vs. K^+/K. Synchrotron X-ray powder diffraction (SXRPD) experiments were conducted on the Powder Diffraction beamline at the Australian Synchrotron, where the collection time for each data point was 180 seconds (including image recording, reading, processing, and erasing), and the time gap between each collection was ~17.5 minutes during discharging and charging using a MYTHEN microstrip detector. The wavelength of synchrotron radiation was determined to be 0.688273 Å using LaB_6 (Standard Reference Material SRM 660b).

5.2.3. Electrochemical measurements

Electrodes were fabricated using a slurry-coating method. The synthesized materials (Sn_4P_3@carbon fibre) were mixed with carboxymethyl cellulose (CMC) in the weight ratio of 9:1. Deionized (DI) water was used as the dispersing agent. Then, the slurry was coated on copper foil and dried in a vacuum oven at 80 ℃ overnight. Coin-type (CR2032) cells were assembled in an argon-filled glove box with oxygen and water content lower than 0.1 ppm. K half-cells were assembled with potassium metal and 0.8 M KPF_6 or 1 M KFSI in an EC/ DEC solution (EC: DEC = 1:1, v/v) as electrolyte. FEC (5 wt. %) as an additive was added into the electrolyte for comparison purposes. Symmetric K foil cells with the same area were tested in various electrolytes at 1 mA cm^{-2} with a fixed amount of areal capacity. Electrochemical impedance and cyclic voltammetry (CV) tests were conducted on a VMP-3 electrochemical workstation. The cells were galvanostatically charged-discharged between 0.01 and 2.0 V versus K/K^+ at various current densities on a Land battery tester. For the specific capacity values, it can be normalized the capacity by the mass of the Sn_4P_3 (after deducting the capacity contribution from carbon fibres). The cells for synchrotron experiments were conducted in KFSI-EC/DEC electrolyte.

5.3. Results and Discussion

5.3.1. Synthesis and structural characterization of the Sn_4P_3@carbon fibre

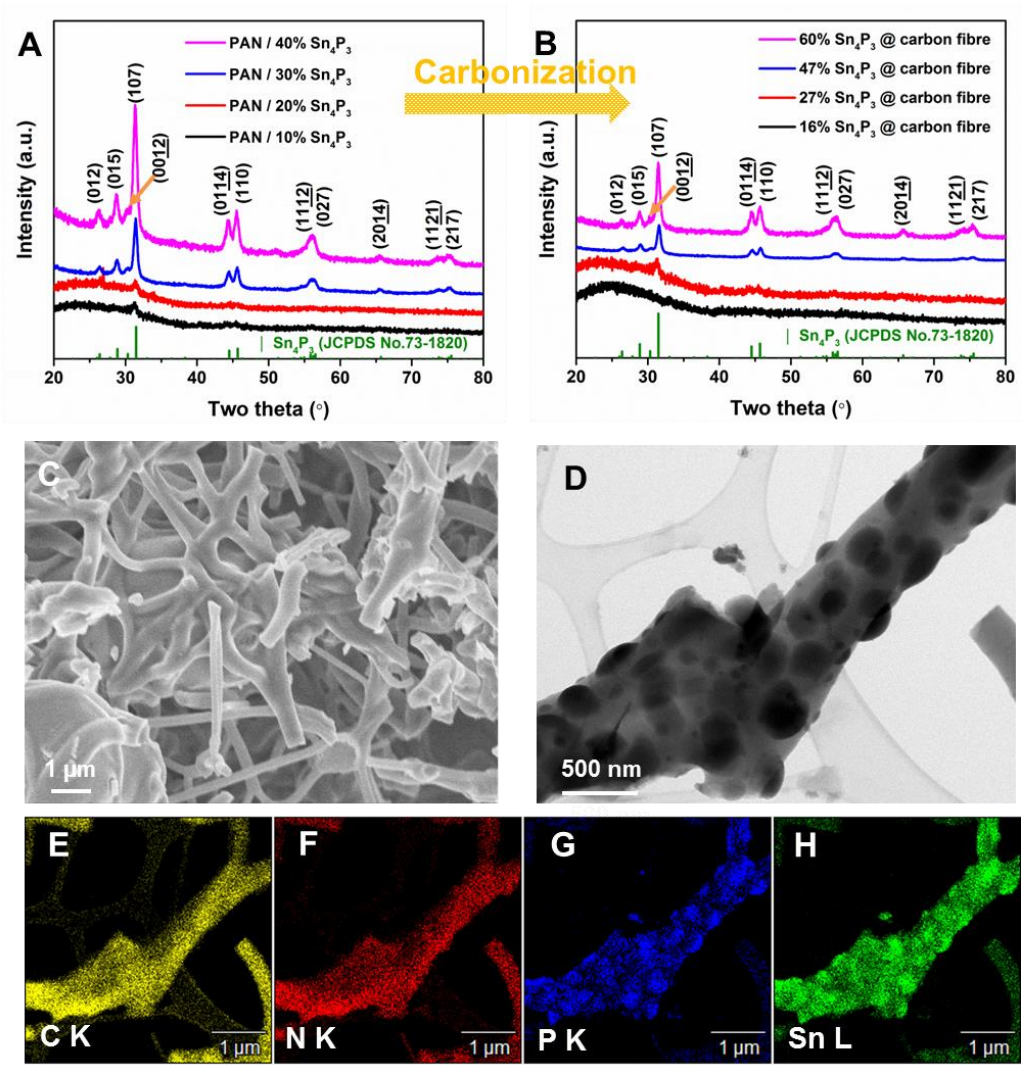

Figure 5.1. Characteration of Sn_4P_3@carbon fibre. XRD patterns of (A) PAN / *x*% Sn_4P_3 and (B) the corresponding Sn_4P_3@carbon fibre. (C) Scanning electron microscope (SEM) image; and (D) STEM image, and (E-H) the corresponding STEM-EDS mapping of Sn_4P_3@carbon fibre (carbonized PAN / 40% Sn_4P_3). (PAN /

x% Sn_4P_3 denotes the PAN/Sn_4P_3 fibre obtained from PAN/DMF solutions containing *x* wt. % Sn_4P_3 via electrospinning.)

The main synthesis strategy to obtain tin phosphide is via ball milling. The electrochemical performance of the as-milled tin phosphide anode is not satisfactory, however, due to the heavy agglomeration of particles and non-uniform morphology, which could cause uneven SEI layer formation. Further treatment of the as-milled particles to enhance their electrochemical performance is urgently needed but barely reported. In this work, a facile, green, and easily scaled up method to confine as-milled Sn_4P_3 particles in N-doped carbon fibres through the electrospinning technique was developed. The carbon fibres have dual functions to improve the cycling performance of Sn_4P_3 anode. Firstly, the porous structure of carbon fibres is helpful for the electrolyte to wet the electrode, thus facilitating the electron and ion transportation. Secondly, stress induced by different volume change ratio between Sn_4P_3 and carbon anodes upon cycling may lead to local dislocation at the interface. The large volume variations of Sn_4P_3 during cycling can be buffered / accommodated by the porous carbon fibres, however, in which the pores provide void spaces for the volume expansion, thus buffering the volume fluctuation of the reactants and preventing the fragmentation and pulverization of the electrode. In this way, the integrity of the electrode is well maintained. As presented in Figure 5.1A and 5.1B, with the addition of 30% and 40% Sn_4P_3 particles to dimethyl formamide (DMF) / poly(acrylonitrile) (PAN) solution as the starting materials, no impurity phases can be

detected and the well-defined peaks in the X-ray diffraction (XRD) patterns can be indexed to the hexagonal $R\bar{3}m$ Sn_4P_3 structure (JCPDS Card No. 73-1820). After the carbonization process, the Sn_4P_3 particles still remain intact. For the samples with 10% and 20% Sn_4P_3 nanoparticles, however, the XRD peaks originating from Sn_4P_3 are hard to distinguish, due to the lower loading amounts of Sn_4P_3 in the carbon fibres.

To determine the loading amount of Sn_4P_3 in the Sn_4P_3@carbon fibre, thermogravimetric analysis (TGA) on the carbonized PAN / (40% and 30%) Sn_4P_3 was performed, as shown in Figure 5.2.

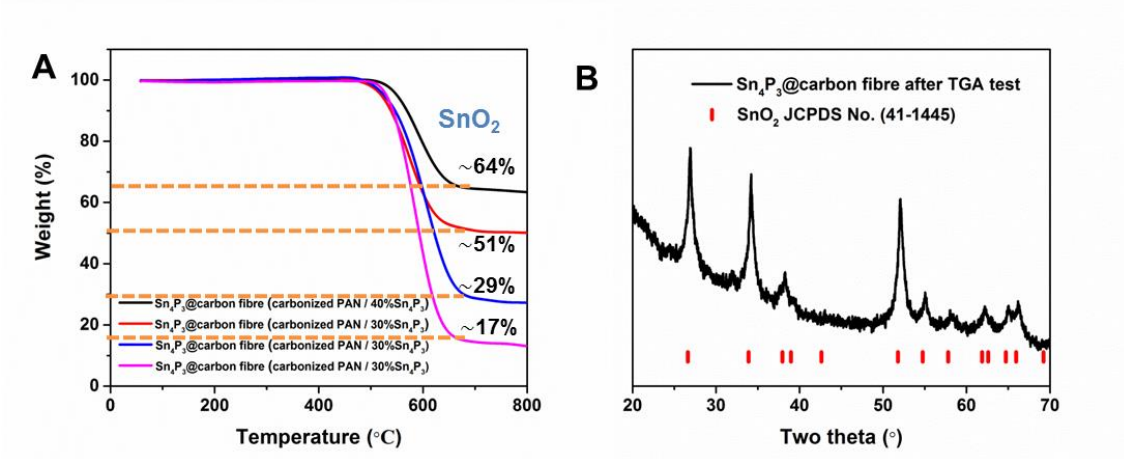

Figure 5.2. Sn_4P_3 contents in Sn_4P_3@carbon fibre samples. (A) TGA test results for Sn_4P_3@carbon fibre. (B) XRD pattern of Sn_4P_3@carbon fibre after TGA test.

The calculated amounts of Sn_4P_3 in the Sn_4P_3@carbon fibres obtained from carbonization of PAN / (40% and 30%) Sn_4P_3, are ～60% and ～47%, respectively. Due to the amorphous nature of the carbon in the fibres, it cannot be observed any peak corresponding to carbon in the XRD patterns. Therefore, Raman spectroscopy

was used to identify the carbon fibres with the corresponding peaks labelled for graphitic (G) ordering at 1590 cm^{-1} and disordered (D) ordering at 1340 cm^{-1}, as shown in Figure 5.3.

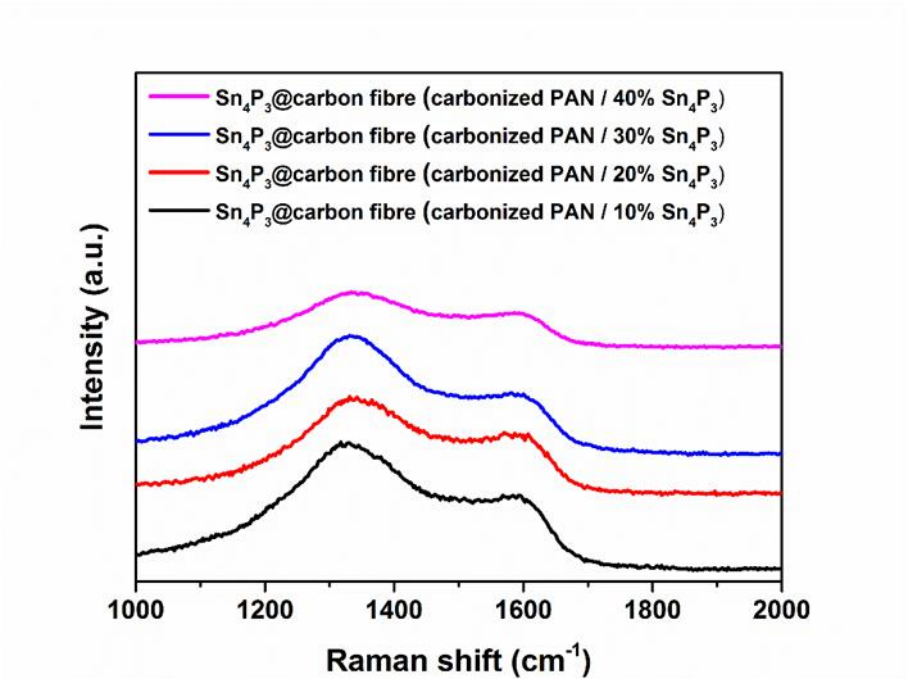

Figure 5.3. Raman spectra of the Sn_4P_3@carbon fibre (carbonized PAN/ *x*% Sn_4P_3).

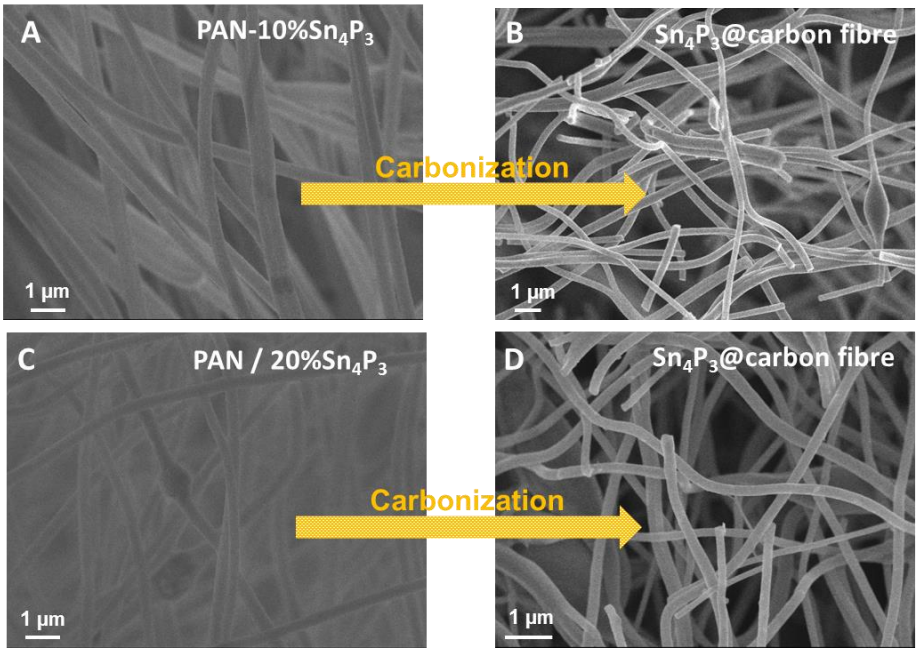

Figure 5.4. Microscopy characterization of polymer fibres and carbon fibres in composites with different amounts of Sn_4P_3. SEM images of (A, C), PAN / *x*% Sn_4P_3 and (B, D) the corresponding Sn_4P_3@carbon fibre composites.

The carbon fibres retain their continuous fibre morphology with smooth surfaces for the samples with low Sn_4P_3 ratios (10 wt. % and 20 wt. % in the starting solution) (Figure 5.4). In contrast, it can be observed that the carbon fibres have fallen apart when the loading amount of Sn_4P_3 (Figure 5.1C) is increased to 40 wt. %. Figure 5.1D-5.1H shows a scanning transmission electron microscope (STEM) image and its corresponding energy dispersive X-ray spectrometry (EDS) mapping of Sn_4P_3@carbon fibre. It was observed that the Sn_4P_3 particles are embedded in the carbon fibres, which have diameters of 400−500 nm. The porous structure formed by the one-dimensional Sn_4P_3@carbon fibres could provide sufficient room to effectively buffer the large volume changes of Sn_4P_3 during potassiation and depotassiation. The inclusion of nitrogen doping in the carbon fibres also enhances the electronic conductivity[18]. EDS mapping (Figure 5.5) and quantitative analysis by X-ray photoelectron spectroscopy (XPS) (Figure 5.6) demonstrate the successful doping of nitrogen into the carbon fibres. The N 1s spectrum can be deconvoluted into three peaks at 398.0, 399.3, and 402.6 eV, which are consistent with pyridinic, pyrrolic, and quaternary N (Figure 5.6B), respectively.

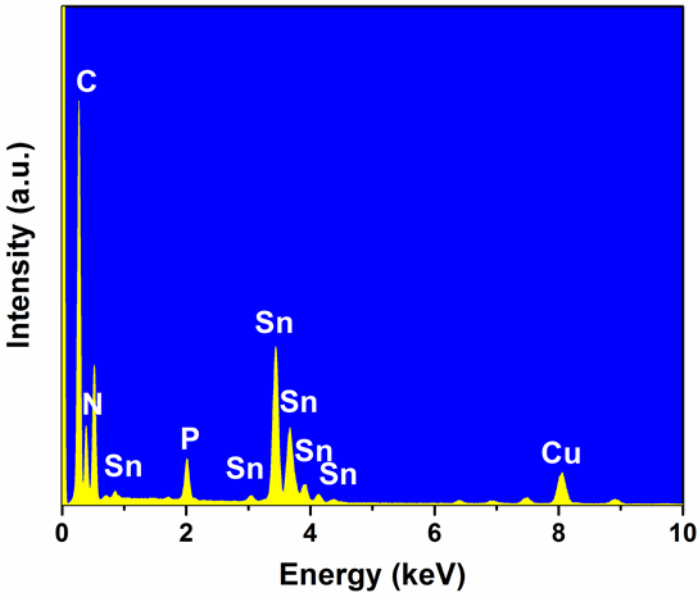

Figure 5.5. STEM-EDS elemental mapping spectrum of Sn_4P_3@carbon fibre (carbonized PAN/ 40% Sn_4P_3).

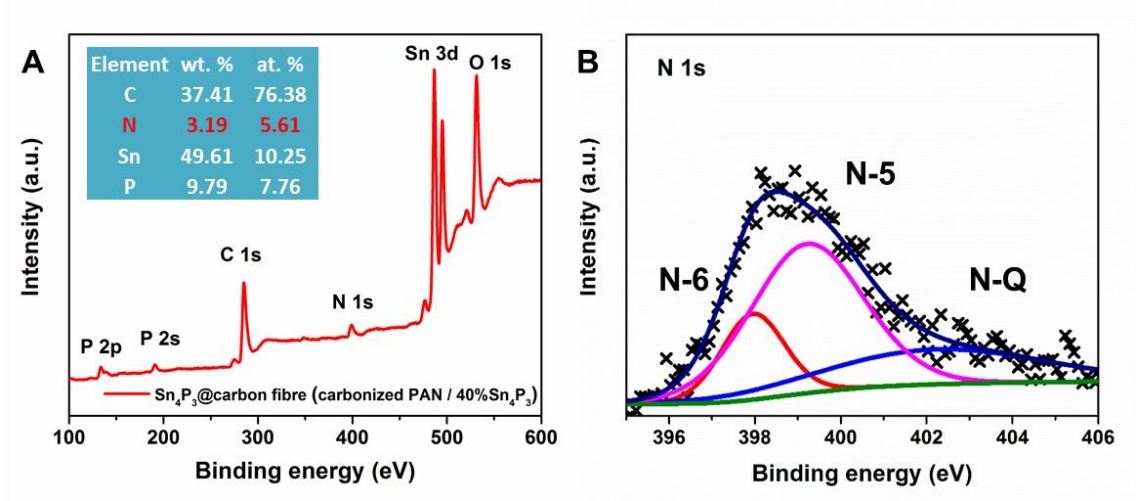

Figure 5.6. XPS spectra of Sn_4P_3@carbon fibre (carbonized PAN/ 40% Sn_4P_3). (A) Full survey spectrum (quantitative analysis of the elements in inset) and (B) N 1s peaks.

5.3.2. Electrochemical performance of 60 % Sn_4P_3@carbon fibre

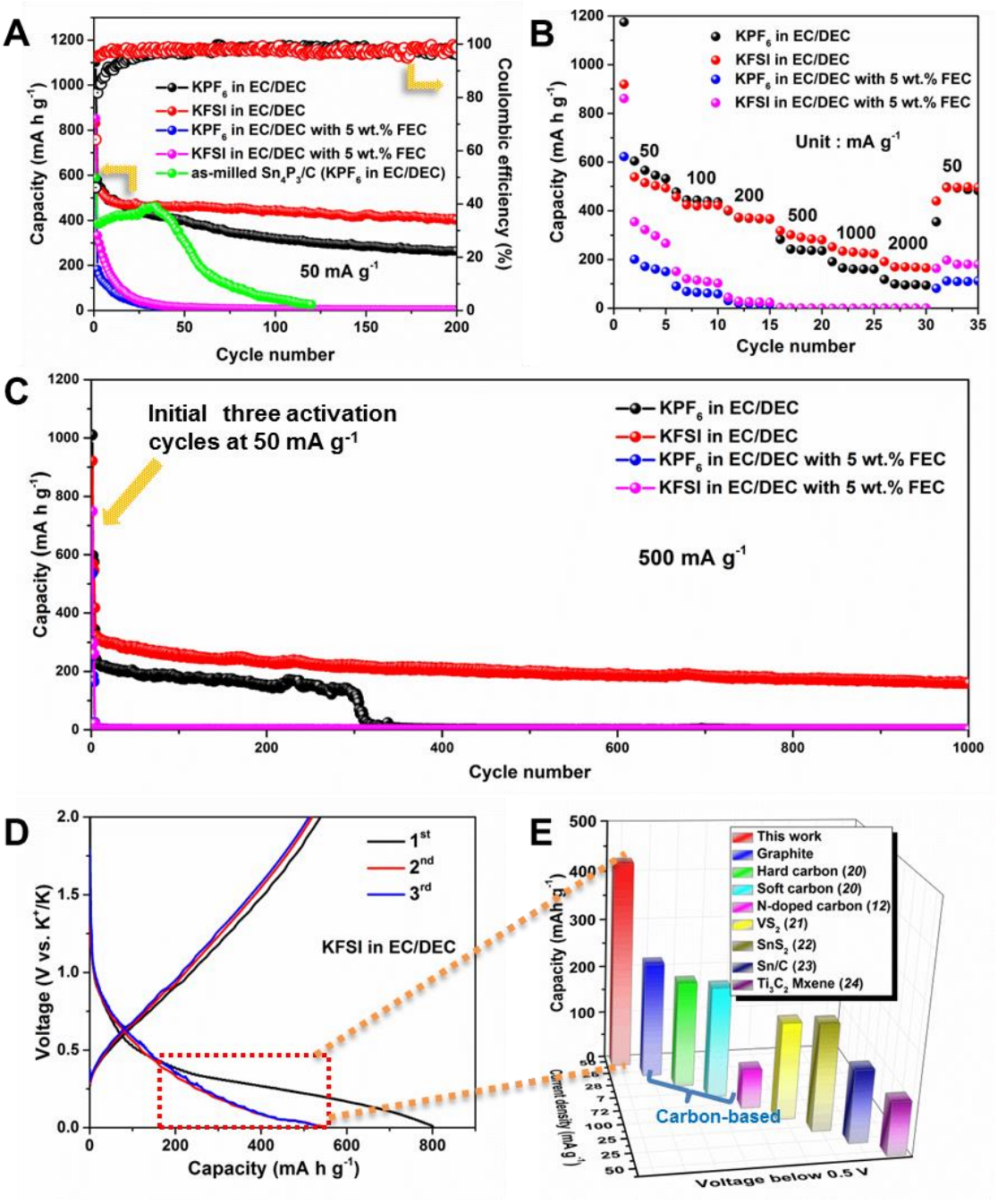

Figure 5.7. Electrochemical performance of 60 % Sn_4P_3@ carbon fibre (carbonized PAN / 40% Sn_4P_3) as anode for PIBs. (A) Cycling performance of cells with various electrolytes at 50 mA g^{-1}. (B) Rate capabilities of cells at various current densities. (C) Long-term cycling performance of the cells with various electrolytes at 500 mA g^{-1}.

(D) Galvanostatic discharge and charge profiles for the first 3 cycles of the electrode in KFSI electrolyte at 50 mA g^{-1}. (E) Comparison of the specific capacity of Sn_4P_3@ carbon fibre with other reported anodes in the voltage range of 0.01-0.5 V.

By confining Sn_4P_3 nanoparticles in carbon fibre, the cycling performance of Sn_4P_3@carbon fibre is remarkably improved (Figure 5.7A) compared to as-milled Sn_4P_3/C particles, with capacity of 400.8 mA h g^{-1} retained after 50 cycles in KPF_6 electrolyte at 50 mA g^{-1}. The initial coulombic efficiency (CE) in KPF_6 electrolyte is only 46.14%, however, which is possibly due to the high irreversible capacity caused by the SEI layer formation. To address the problems of low initial CE and the unsatisfactory cycling performance, a low-fluoride-content potassium salt was adopted, KFSI. As shown in Figure 5.7A, the Sn_4P_3@carbon fibre electrode with KFSI electrolyte presents a relatively high initial CE of 64.17% and very stable cycling performance, with retained capacity of 403.1 mA h g^{-1} even after 200 cycles at 50 mA g^{-1}. It also shows superior rate performance (Figure 5.7B), delivering 514.7, 424.3, 372.9, 301.4, 233.8, and 169.6 mA h g^{-1} at the current densities of 50, 100, 200, 500, 1000, and 2000 mA g^{-1}, respectively. In order to further improve the electrochemical performance of the Sn_4P_3@carbon fibre electrodes, FEC was adopted as an additive, inspired by its application in sodium ion batteries (SIBs) [19]. With the addition of 5 wt. % FEC to both KFSI-EC/DEC and KPF_6-EC/DEC electrolytes, however, the specific capacity dropped quickly after a few cycles at 50 mA g^{-1}, and the capacity was almost zero at high current densities. Figure 5.8 compares the

electrochemical impedance spectroscopy (EIS) results for the Sn_4P_3@carbon fibre in various electrolytes. The EIS spectra of cells in various electrolytes after 5 cycles are composed of one small semicircle in the high-frequency range and a second large semicircle in the relatively low-frequency range, which can be distinguished by enlarging the high frequency range (inset of Figure 5.8F-I). The first intercept with the Z'-axis represents the ohmic resistance, which is mainly affected by the electrolyte. The small semicircle at high frequency is regarded as due to the impedance of the solid-electrolyte interphase (SEI) layer (R_f), and the large semicircle at relatively lower frequency is assigned to the impedance generated by R_{ct} and the electrical double-layer capacitance. The linear increase in impedance after the semicircles is caused by K^+ diffusion inside the particles, referred to as the Warburg impedance[20]. Based on this interpretation, equivalent circuit models for fresh electrodes and electrodes after 5 cycles are shown in Figure 5.8 E and J, respectively. As shown in Table 5.1, it is obvious that the values of R_{ct} and R_f of the cell in KFSI with EC/DEC electrolyte are the smallest after 5 cycles compared to electrodes in other electrolytes, indicating that the cell has relatively low resistance from the SEI layer and charge transfer in KFSI with EC/DEC electrolyte.

Figure 5.9 A and B display cyclic voltammograms (CV) of the Sn_4P_3@carbon fibre in KPF_6-EC/DEC and KFSI-EC/DEC electrolytes. Based on the in operando XRD results, the detailed reaction processes can be illustrated below. During the first cathodic scan, the broad peaks (0.01-1 V) are attributed to the potassiation reaction of

K-P (where P initially reacts with K and forms an amorphous state starting at 1 V, K_3P_{11} first emerges at ~0.21 V, and K_3P is formed from ~0.17 V) and K-Sn alloy (KSn formed from ~0.4 V) processes, and the formation of the solid electrolyte interphase (SEI) layer. In the second and subsequent cathodic scans, this large reduction band has obviously become shrunken, and another new reduction peak has appeared at around 0.1 V, which is attributed to the formation of K_3P and KSn. During the anodic scans, the oxidation peaks at around 0.75 and 0.96 V are mainly attributed to depotassiation reactions from the K-Sn and K-P, respectively. The data in Figure 5.10 enable us to determine the relative contributions associated with both diffusion and capacitive processes. The current response at a fixed potential could be expressed as being the combination of two separate mechanisms, surface capacitive effects and diffusion-controlled insertion processes:

$$i(V) = k_1 v + k_2 v^{1/2} \quad (1)$$

In Equation (1), $k_1 v$ and $k_2 v^{1/2}$ correspond to the current contributions from the surface capacitive effects and the diffusion-controlled intercalation process, respectively. Thus, by determining k_1 and k_2, we are able to quantify, at specific potentials, the fraction of the current due to each of these contributions.

It can be found that capacitive effects contributed 35%, 43%, 55%, 73%, and 88% of the total potassium ion storage at the scan rates of 0.1, 0.2, 0.3, 0.5, and 1 mV s^{-1}, respectively. The disparity in charge storage for the two different mechanisms becomes more pronounced at high sweep rates because of the rapid charge/discharge

characteristics associated with capacitive processes. Clearly, the capacitive contributions from the low scanning rates are significantly smaller than those from the high scan rates. Therefore, the above analysis indicates that a capacitive storage mechanism is involved, especially at high sweep rates, while the potassium ion storage is dominated by the diffusion processes at a relatively slow sweep rate (0.1 and 0.2 mV s^{-1}).

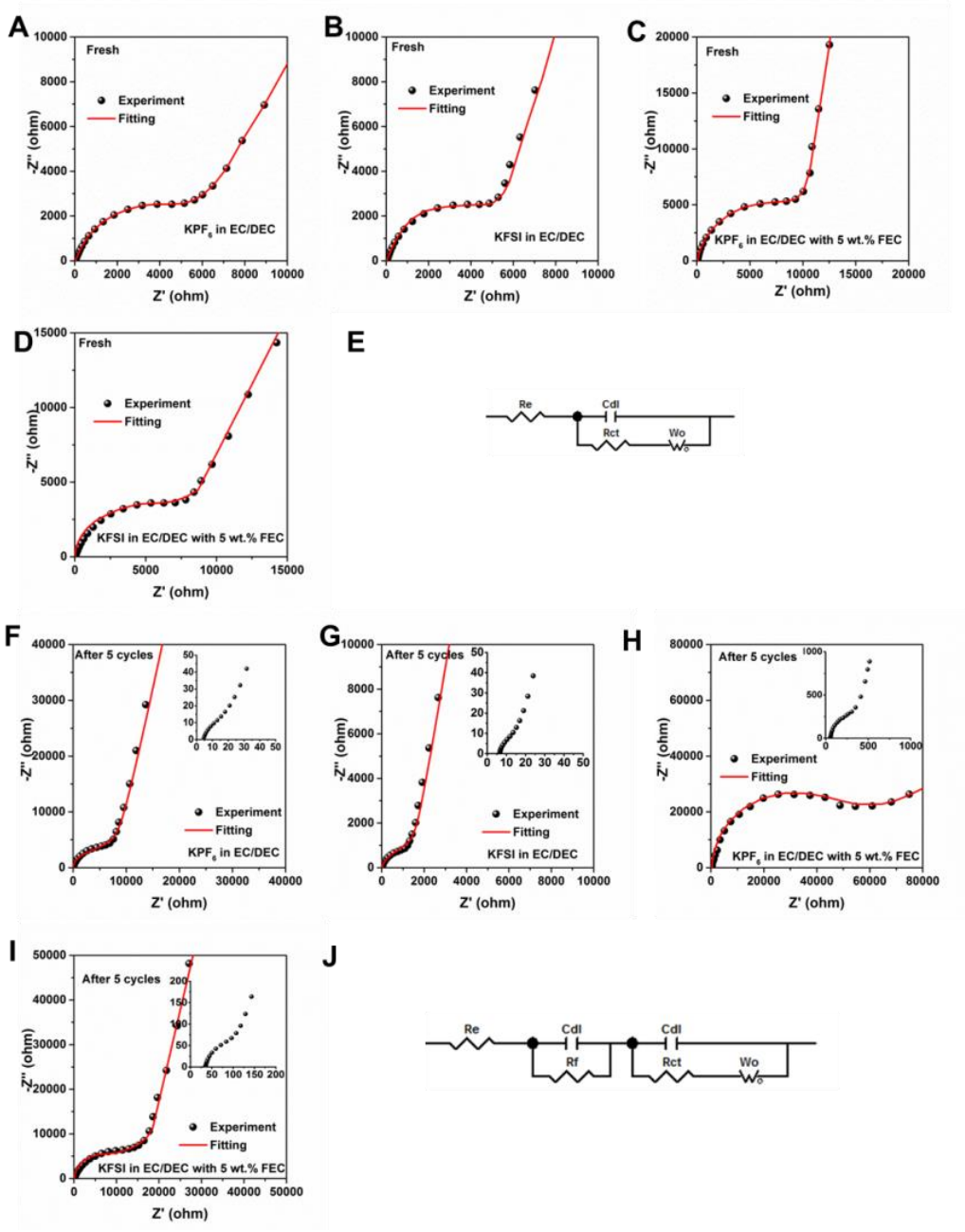

Figure 5.8. Nyquist plots of the cells in various electrolytes (A-D) before cycling and (F-I) after 5 cycles. Equivalent circuits for the cells in various electrolytes (E) before cycling and (J) after 5 cycles (R_e: ohmic resistance, R_f: resistance from the SEI layer, C_{dl}: electrical double-layer capacitance, R_{ct}: charge-transfer resistance, W_0: Warburg impedance).

Table 5.1. Electrical parameters of the cells in various electrolytes before cycling and after 5 cycles, determined from the fitting of the impedance spectra to the equivalent circuits presented in Figure 5.8.

Electrolyte used	Fresh (R_{ct}: Ω)	After 5 cycles (R_f: Ω)	After 5 cycles (R_{ct}: Ω)
KPF_6 in EC/DEC	6110	23	6443
KFSI in EC/DEC	7452	18	1297
KPF_6 in EC/DEC with 5 wt. % FEC	9831	455	29857
KFSI in EC/DEC with 5 wt. % FEC	7753	154	7500

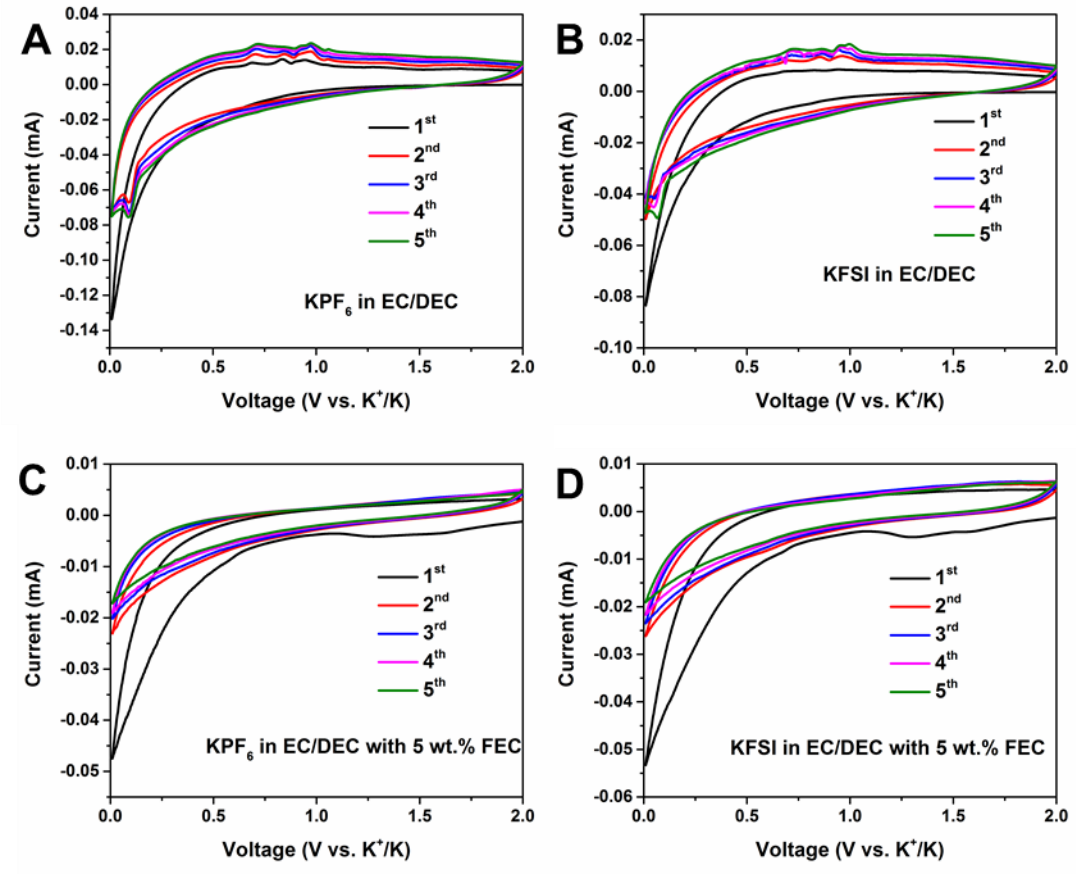

Figure 5.9. Cyclic voltammograms of Sn_4P_3@carbon fibre electrode in various electrolytes at the scanning rate of 0.05 mV s^{-1}.

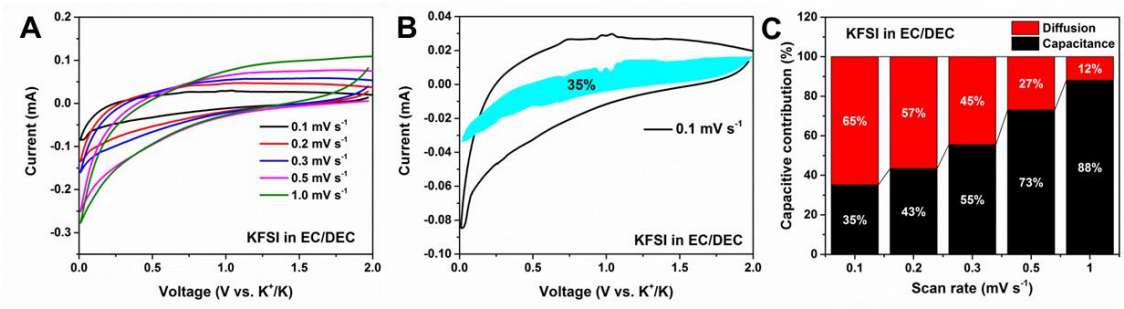

Figure 5.10. (A) Cyclic voltammograms of Sn_4P_3@carbon fibre electrode at various scanning rate from 0.1 to 1.0 mV s^{-1}. The electrolyte was KFSI in EC/DEC, (B) Separation of the capacitive and diffusion-controlled charges at 0.1 mV s^{-1}, (C)

Comparison of the contribution ratio of the capacitive and diffusion-controlled charge versus scan rate.

To better understand the long-term electrochemical behaviour of Sn_4P_3@carbon fibre electrodes, the cells were cycled in four electrolytes at a current density of 500 mA g^{-1} (Figure 5.7C). After activation during the initial three cycles at the current density of 50 mA g^{-1}, the Sn_4P_3@carbon fibre electrode in KFSI electrolyte exhibited superior stable cycling performance and still maintained 160.7 mA h g^{-1} after 1000 cycles. In the KPF_6 electrolyte, however, the capacity was relatively stable in the first 300 cycles, but it dropped significantly to nearly zero afterwards. To understand the reason for the capacity fading, the cells were cycled in KPF_6 electrolyte in different voltage ranges with low cut-off potentials of 0.05 V, 0.1 V, and 0.2 V, respectively. As can be observed in Figure 5.11, the electrode suffered from severe capacity fading after around 650 cycles in the voltage range of 0.05-2 V. In contrast, by slightly increasing the low cut-off voltage to 0.1 or 0.2 V, excellent cycling performance could be obtained, even after 1000 cycles, but there is a sacrifice, relatively low specific capacity due to the higher cut-off potential. The discharge/charge profiles of the electrodes in KPF_6 electrolyte at 500 mA g^{-1} with various low cut-off voltages are shown in Figure 5.12. The electrodes can maintain relatively stable cycling performance for the voltage ranges of 0.1-2 V and 0.2-2 V, although the electrodes suffered severe capacity fading after the 350^{th} cycle and 720^{th} cycle for the voltage ranges of 0.01-2 V and 0.05-2 V, respectively. As shown in Figure 5.13 and Figure

5.14, cells cycled to a lower cut-off voltage exhibit relatively lower initial coulombic efficiency, indicating that more side reactions occur at lower cut-off voltage. The capacity fading may be due to the extensive consumption and drying up of the electrolyte caused by various side reactions, structural/phase instability, and dendrite formation.

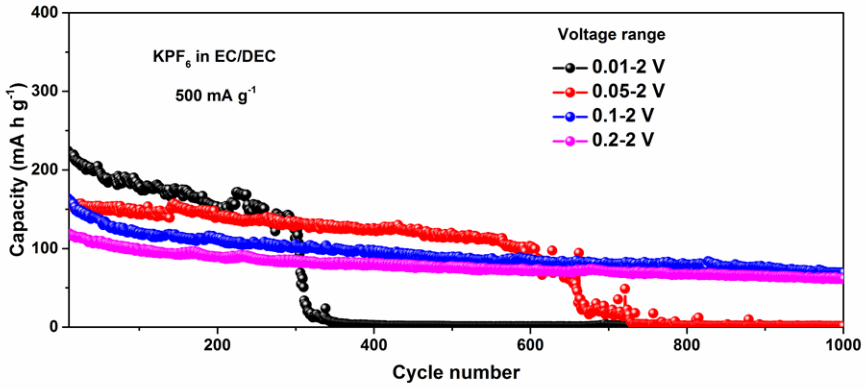

Figure 5.11. Long-term cycling tests of the cells in various voltage ranges at 500 mA g^{-1} in KPF_6 electrolyte.

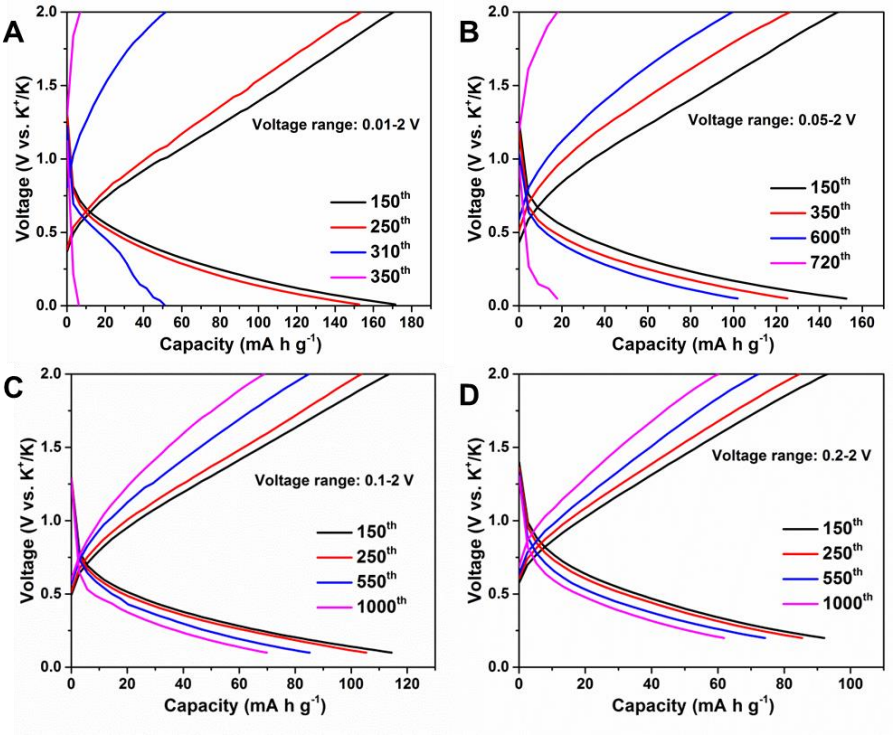

Figure 5.12. Galvanostatic discharge and charge profiles for selected cycles of the electrodes in KPF_6 electrolyte at 500 mA g^{-1} with various lower cut-off voltages.

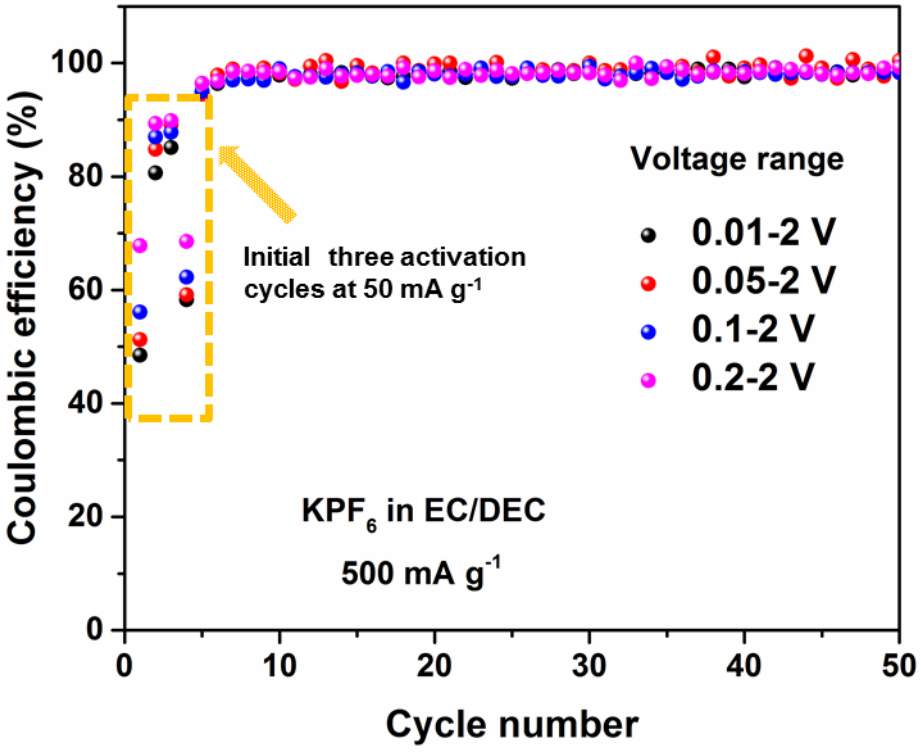

Figure 5.13. Coulombic efficiency of the electrode in KPF_6 electrolyte for various voltage ranges. Note that the cells were cycled at 50 mA g^{-1} in the first 3 cycles and cycled at 500 mA g^{-1} in the following cycles.

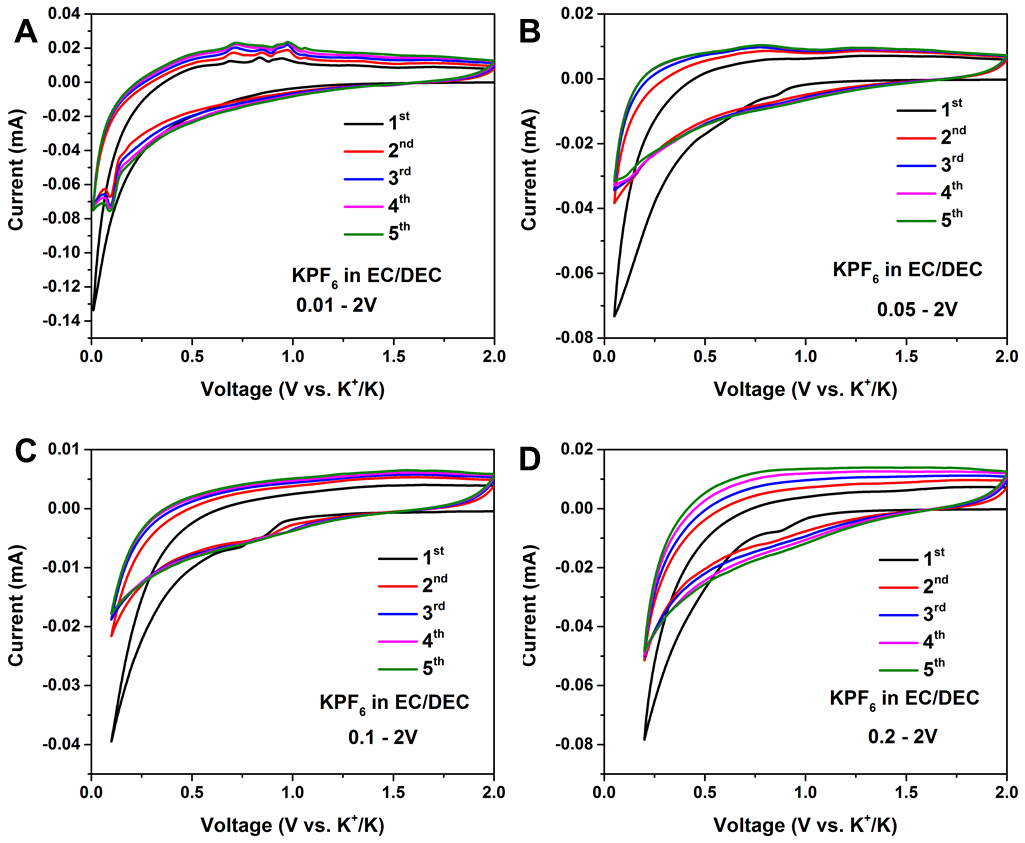

Figure 5.14. Cyclic voltammograms of Sn_4P_3@carbon fibre electrode in KPF_6 electrolyte with various lower cut-off voltages.

It is well known that energy density is a crucial parameter for real applications [21-23]. The energy density is the product of the capacity and the working potential of the battery, in which the working potential is determined by the voltage gap (ΔV) between the anode and the cathode during electrochemical cycling. Carbon-based electrode materials, especially amorphous carbon, have been reported recently with superior

cycling performance, but it was noticed that the carbon has a sloping discharge curves with the majority of the capacity in the high voltage range (Figure 5.15), which will lead to a low energy density for the full cells [10]. Compared to the amorphous carbon anodes, the Sn_4P_3@carbon fibre electrode exhibits reasonable cycling stability, with only 0.064% capacity fading per cycle. As shown in Figure 5.7D, however, the capacity below 0.5 V is ~428 mA h g^{-1}, which is 80.75% of the total capacity. Given that the high-voltage contribution of the anode to the energy density of battery is less significant, I only compare the portion of capacity in the low voltage range (< 0.5 V) with that of previously reported anode materials (Figure 5.7E). It is obvious that the Sn_4P_3@carbon fibre electrode delivers the highest reversible capacity under 0.5 V compared with the carbon-based [7, 10, 24], sulphide [25-26], and other alloy-based materials [27-28]. Therefore, there should be great interest in and potential for developing Sn_4P_3 as a high-energy-density anode material for PIBs.

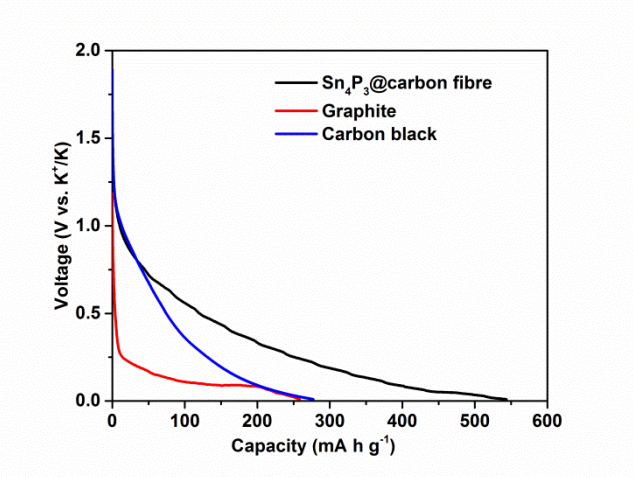

Figure 5.15. Galvanostatic discharge profiles of Sn_4P_3@carbon fibre, graphite, and carbon black as anode for PIBs.

5.3.3. Effect of the electrolyte on electrode polarization

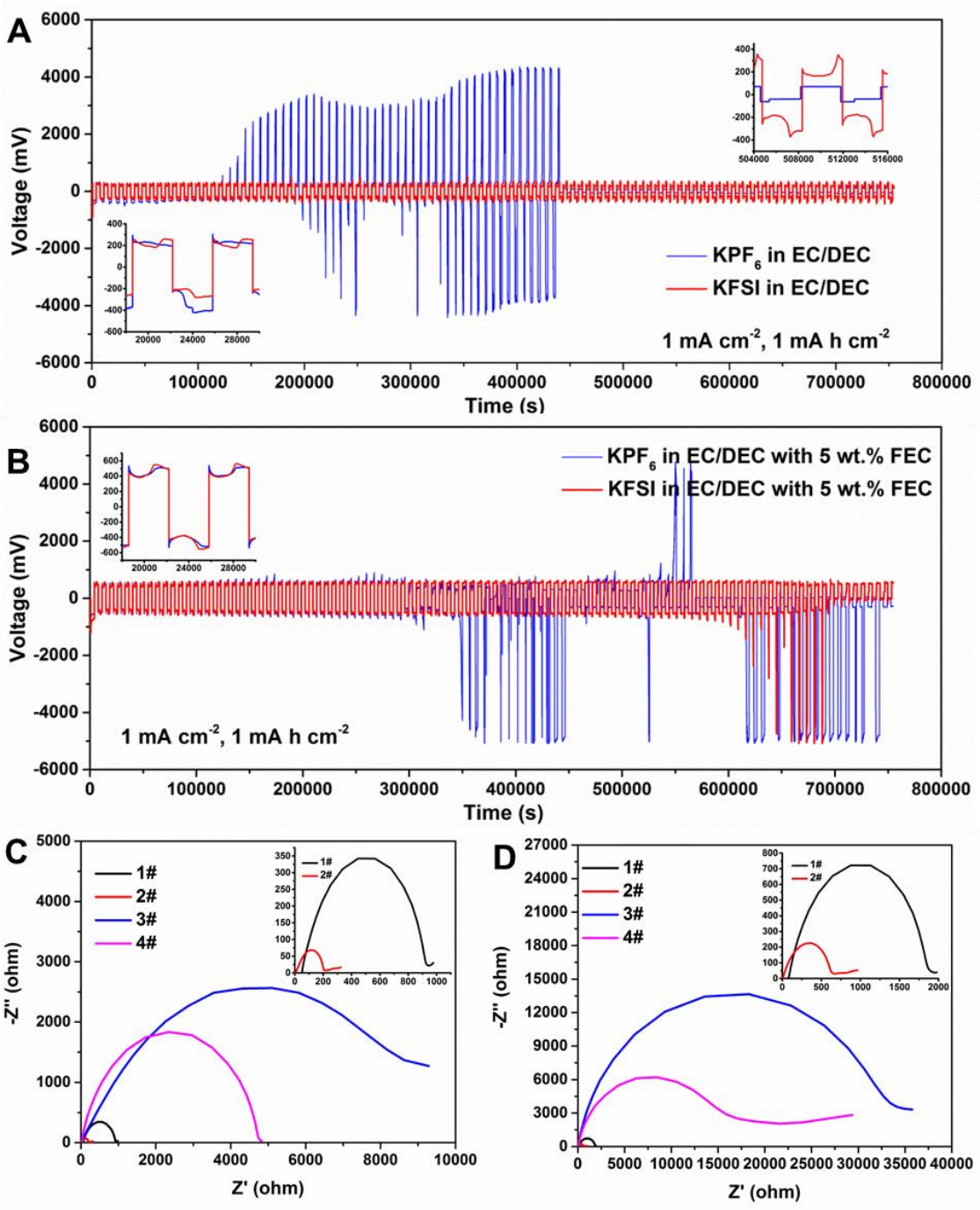

Figure 5.16. Electrochemical characterization of K metal in various electrolytes. Galvanostatic cycling of a symmetric K foil cell, without (A) and with (B) FEC at the current density of 1 mA cm^{-2} with a stripping/plating capacity of 1 mA h cm^{-2}. Insets:

detailed voltage profiles for the corresponding times. Nyquist plots of the symmetric cells after (C) 10 and (D) 100 galvanostatic cycles, respectively. Insets: enlarged plots of the corresponding curves. (Electrolytes denoted by symbols: 1# KPF_6, 2# KFSI, 3# KPF_6 with FEC, and 4# KFSI with FEC, respectively.)

Inspired by the use of symmetric lithium foil cells to study the polarization and dendrite growth in lithium metal anode research [29], the electrochemical behaviour of K plating/stripping was examined in order to understand the effects of the various potassium-based electrolytes on polarization and potassium dendrite formation. Figure 5.16A and 5.16B compares the voltage profiles of symmetric potassium foil cells with the four electrolytes over 100 cycles at 1 mA cm^{-2}. Potassium foil in KFSI electrolyte exhibited exceptional cycling stability. In contrast, severe fluctuations in voltage profiles was observed in the KPF_6 electrolyte, which is ascribed to the effect of the polarization caused by the continuous formation of SEI layers on the fast growth of dendrites.

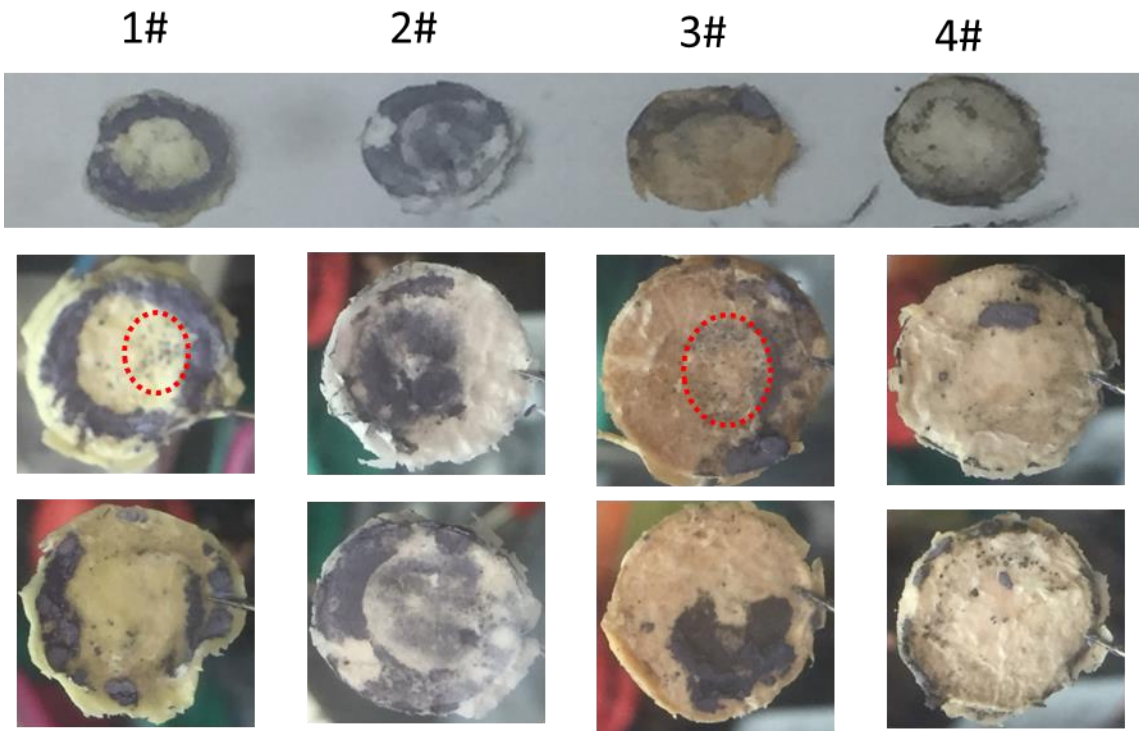

Figure 5.17. Ex-situ digital photographs of the separators from symmetric K foil cells after 100 cycles in various electrolytes. (Electrolytes denoted by symbols: 1# KPF_6, 2# KFSI, 3# KPF_6 with 5 wt. % FEC, 4# KFSI with 5 wt. % FEC, respectively.)

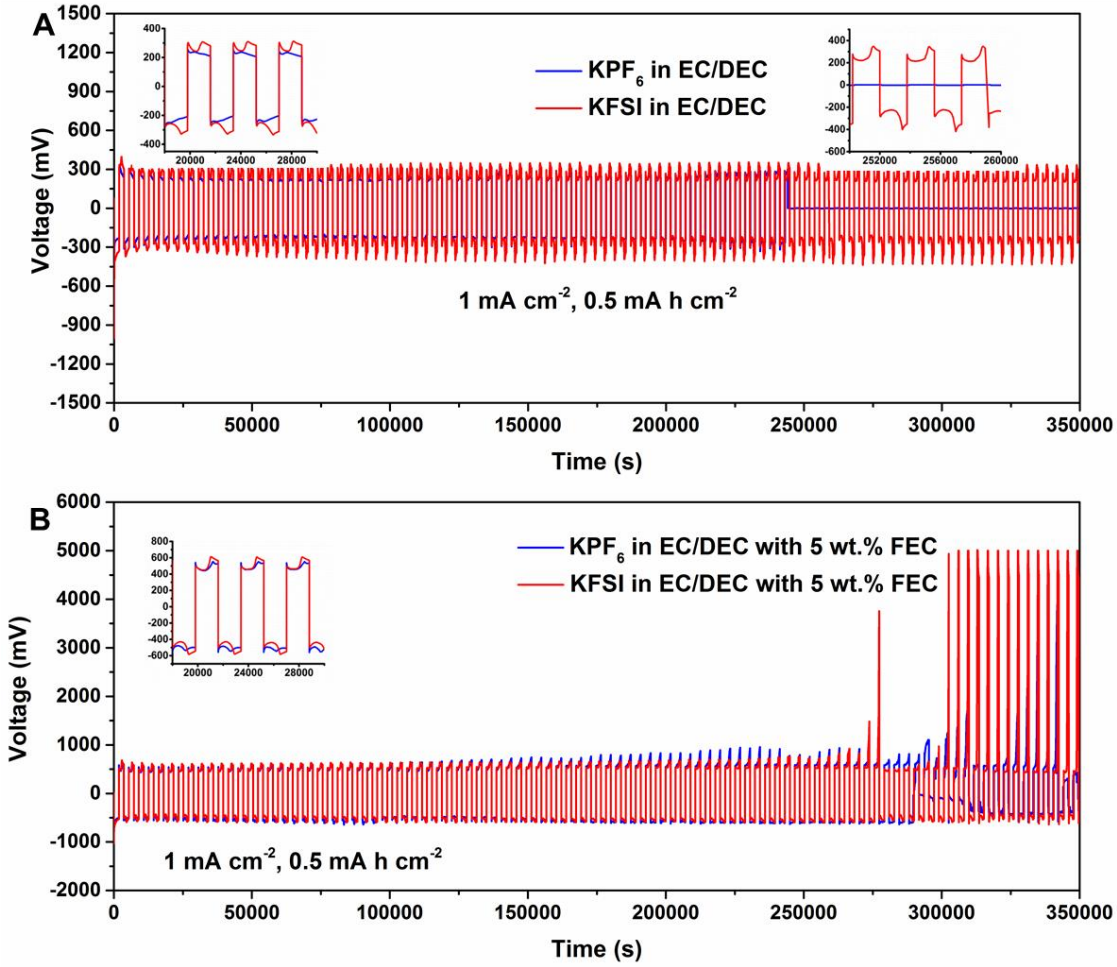

Figure 5.18. Galvanostatic cycling of symmetric K foil cells with various electrolytes at the current density of 1 mA cm^{-2} with a stripping/plating capacity of 0.5 mA h cm^{-2}. Insets: detailed voltage profiles for the corresponding times.

Additionally, a sudden potential drop was detected for potassium foil in KPF_6 electrolyte with fluctuating voltage in the later cycles, which may be due to an internal short-circuit caused by K dendrite penetration. It can be observed that potassium foil electrodes in the electrolyte with FEC additive have a higher hysteresis

(±500 mV) than without FEC (±200 mV) (insets of Figure 5.16A and 5.16B), indicating large polarization due to the introduction of FEC. Small pores can be observed in the red circles labelled on the digital photographs of the separators cycled with KPF_6 electrolyte after 100 cycles (Figure 5.17), suggesting that potassium dendrites have possibly stabbed into the separators. At the same current density, but with a lower areal capacity of 0.5 mA h cm^{-2} (Figure 5.18), stable cycling can still be achieved with K foil in KFSI electrolyte, whereas the K foil in KPF_6 electrolyte exhibited short-circuiting after a certain time. A similar tendency with high hysteresis can also be observed due to the addition of FEC.

The effect of electrolyte on the polarization and cycling performance is further evidenced by the EIS analysis conducted on symmetric cells. On comparing the corresponding Nyquist plots (Figure 5.16C and D), the K foil electrodes in KFSI electrolyte show the smallest interfacial resistance among the four electrolytes after 10 and 100 cycles, which is in good agreement with their stable cycling performance in symmetric tests. These results illustrate that KFSI electrolyte without FEC suppresses the dendrite growth in K stripping/plating kinetics and exhibits better cycling stability.

5.3.4. SEI layer composition in various electrolytes (60 % Sn_4P_3@carbon fibre)

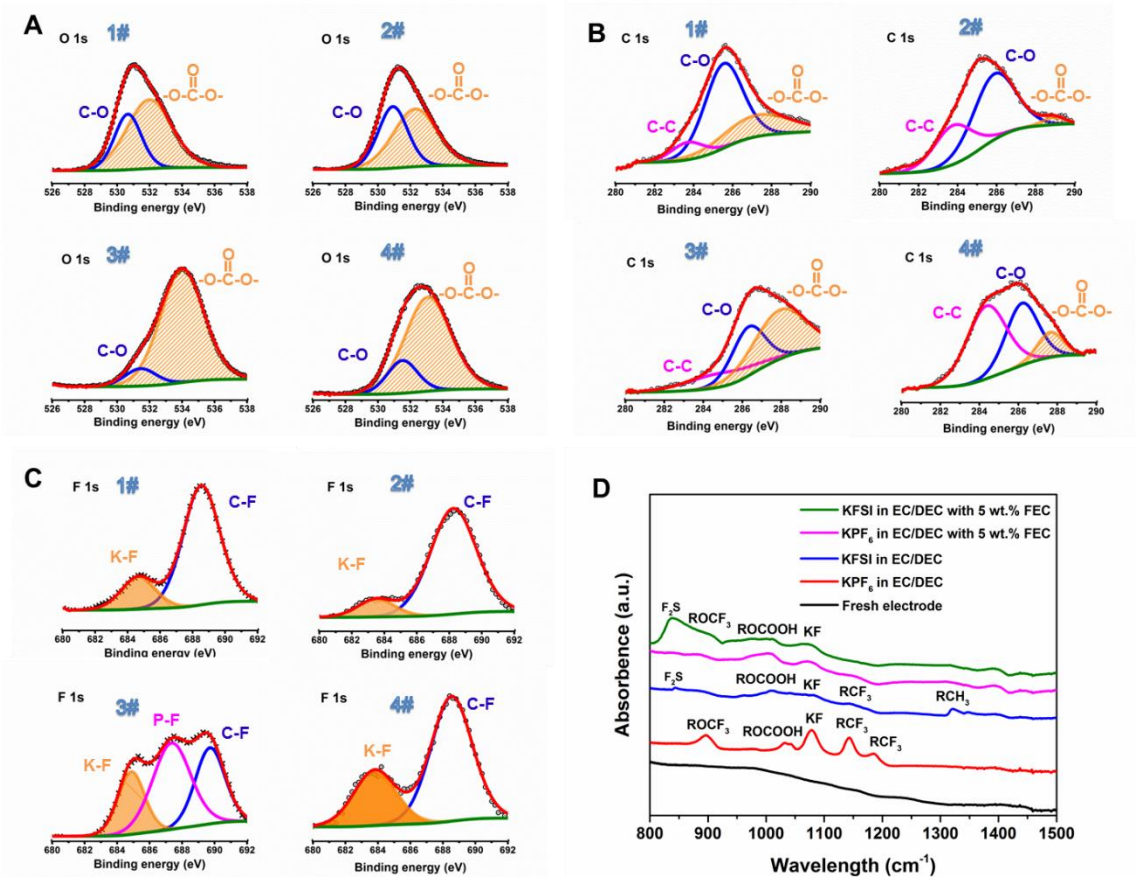

Figure 5.19. Characterization of the components of SEI formed during cycling. XPS spectra of (A) O 1s, (B) C 1s, and (C) F 1s for the cells containing various electrolytes after 350 cycles at 500 mA g^{-1}. (Electrolytes denoted by symbols: 1# KPF_6, 2# KFSI, 3# KPF_6 with FEC, and 4# KFSI with FEC, respectively.) (D) FTIR spectra of the electrode surfaces in various electrolytes after one cycle.

The dendrite growth can be suppressed to some extent via reversible K metal plating/stripping, forming an even SEI layer [30]. In order to study the roles of KPF_6, KFSI, and FEC additive in the SEI formation, the morphology of electrode surfaces

that were cycled for 350 cycles at 500 mA g^{-1} were investigated through scanning electron microscopy (SEM). The electrodes in electrolytes without FEC exhibited a smooth surface, as shown in Figure 5.20A-F. With FEC additive, however, small particles can be found on the surface (Figure 5.20G-L), indicating an inhomogeneous SEI layer. As evidenced by EDS (Figure 5.21), the content of elemental F in the electrolyte with FEC is higher than that in electrolyte without FEC. The high P losses shown in the EDS analysis after 350 cycles are possibly due to the roughness of the electrode surfaces. The typical escape depth of X-rays (Z = Si-Zn) in EDS analysis is around 1−2 μm. The model used in quantitative EDS analysis is predicated on a flat polished surface, with a well-defined take-off angle to the detector. In this case the surface of the electrode was very rough without any polishing treatments, and the results are, at best, qualitative. Low energy x-rays from lighter elements ($Z \leq F$) are strongly absorbed. The intensities for F are therefore highly localised to the surface. Even for ideal flat specimens, this skews the quantitative results, which are normalised to 100%, making them not very precise. For comparison purposes, SEM mapping (Figure 5.22) of the original electrode surface and the electrode after the 1st cycle were also conducted. The measured molar ratio of the elemental Sn to P (59 ± 5: 41 ± 2 = 4.3: 3) is in reasonable agreement with that expected for the Sn_4P_3 phase (4: 3), despite the uncertainties mentioned above. After the 1st cycle, the molar ratio of Sn to P increases to around 6.6:3. This suggests that the P loss may be due to signal interference by absorption in various elemental components. There is considerable

uncertainty in this type of qualitative EDS, which is due to the surface roughness and the highly localised nature of analysis.

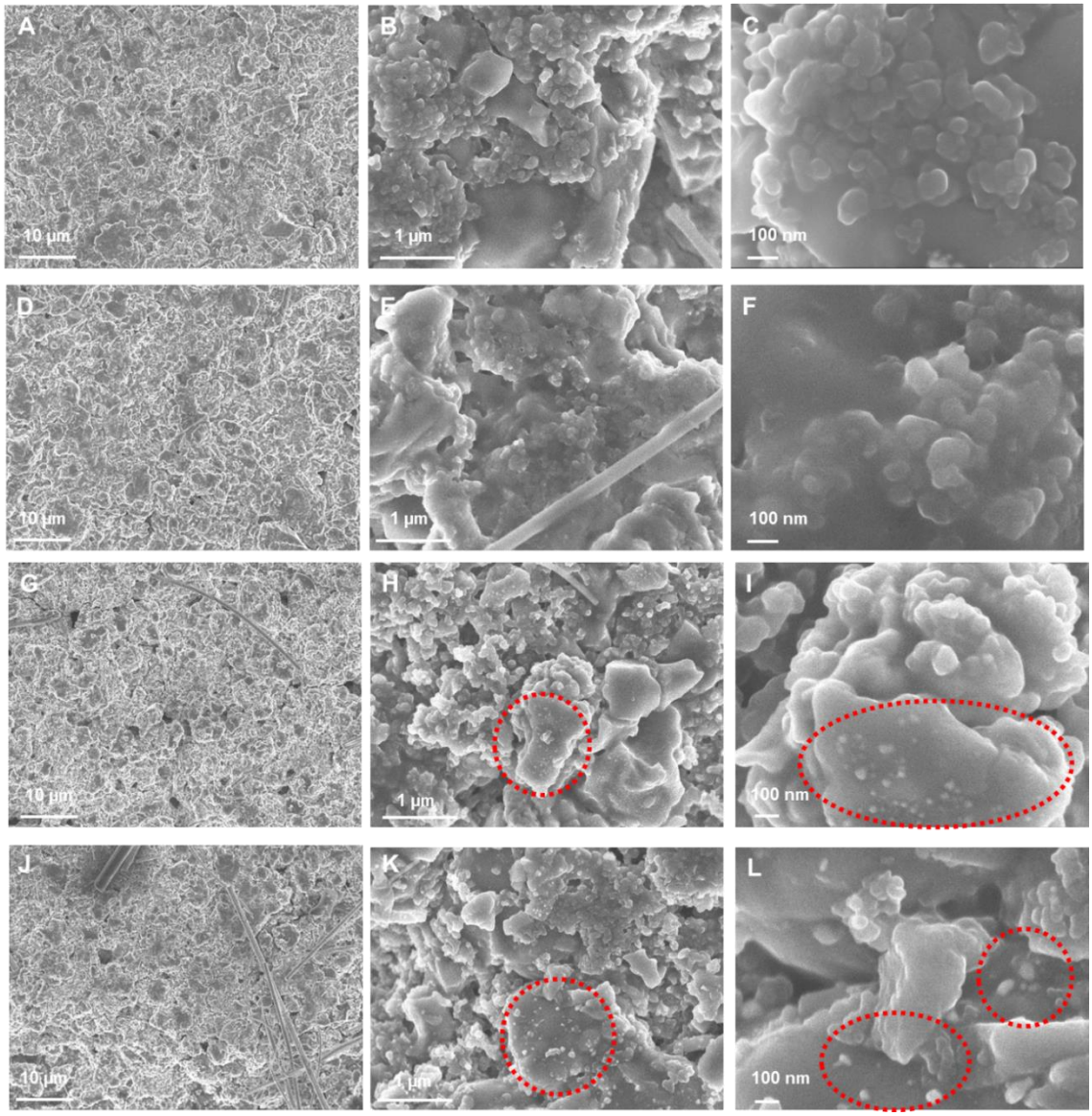

Figure 5.20. Ex situ SEM images of the electrodes after 350 cycles at 500 mA g^{-1} in various electrolytes. (A-C) KPF_6, (D-F) KFSI, (G-I) KPF_6 with 5 wt. % FEC, (J-L) KFSI with 5 wt. % FEC. (The covered fibre on the electrodes are from glass fibres.)

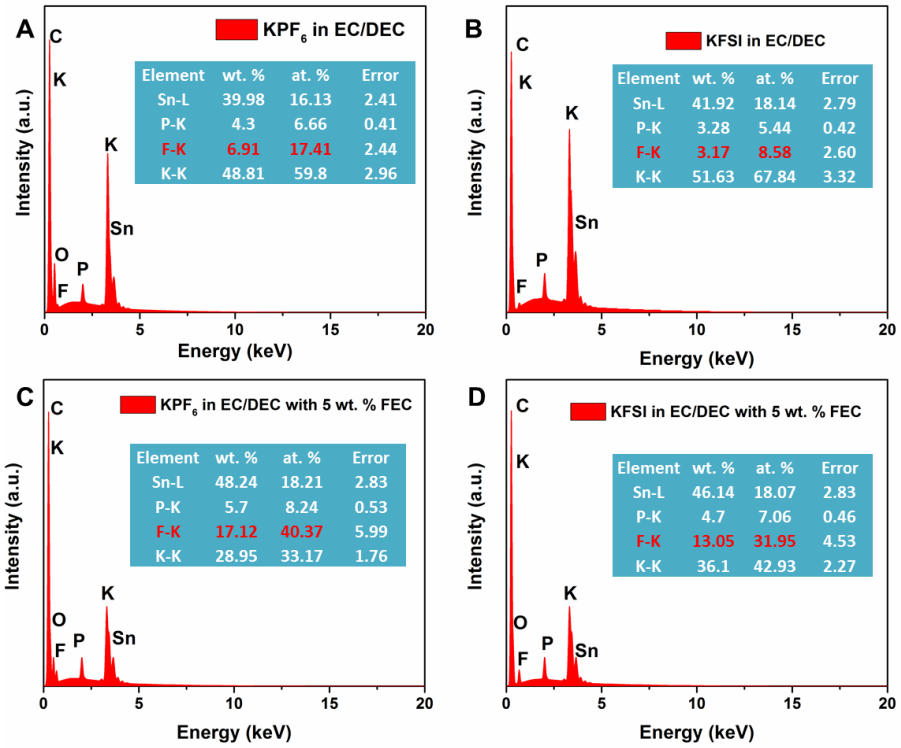

Figure 5.21. EDS elemental analysis of the electrodes after 350 cycles at 500 mA g^{-1} in various electrolytes: (A) KPF_6, (B) KFSI, (C) KPF_6 with 5 wt. % FEC, (D) KFSI with 5 wt. % FEC.

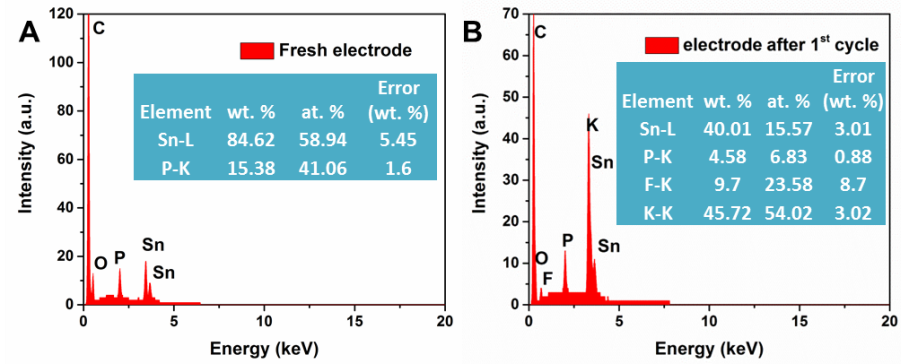

Figure 5.22. EDS elemental analysis of the A) fresh electrode and B) after the 1st cycle in KPF_6 electrolyte.

Figure 5.23 exhibits the morphology and the uniformity of the SEI layer in various electrolytes. The electrodes in electrolytes without FEC exhibited a smooth surface, as shown in Figure 5.23A-D. With FEC additive, however, small particles can be found on the surface (Figure 5.23E-H). As further investigated by STEM-EDS (Figure 5.24), the content of elemental tin in these small particles was obviously higher than in the other areas, indicating an inhomogeneous SEI layer.

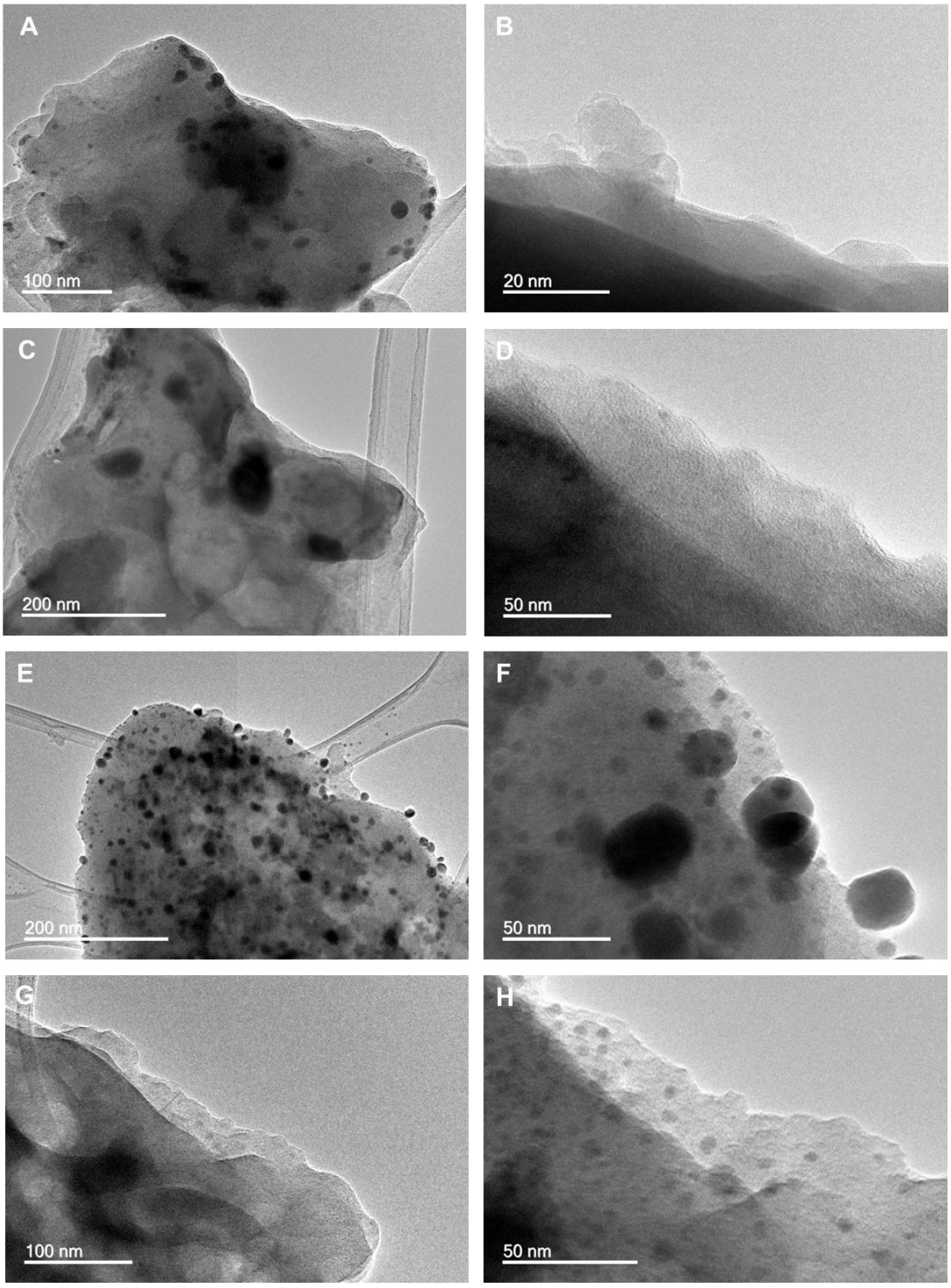

Figure 5.23. Ex situ TEM images of the electrodes after 350 cycles at 500 mA g^{-1} in various electrolytes. (A, B) KPF_6, (C, D) KFSI, (E, F) KPF_6 with 5 wt. % FEC, (G, H) KFSI with 5 wt. % FEC.

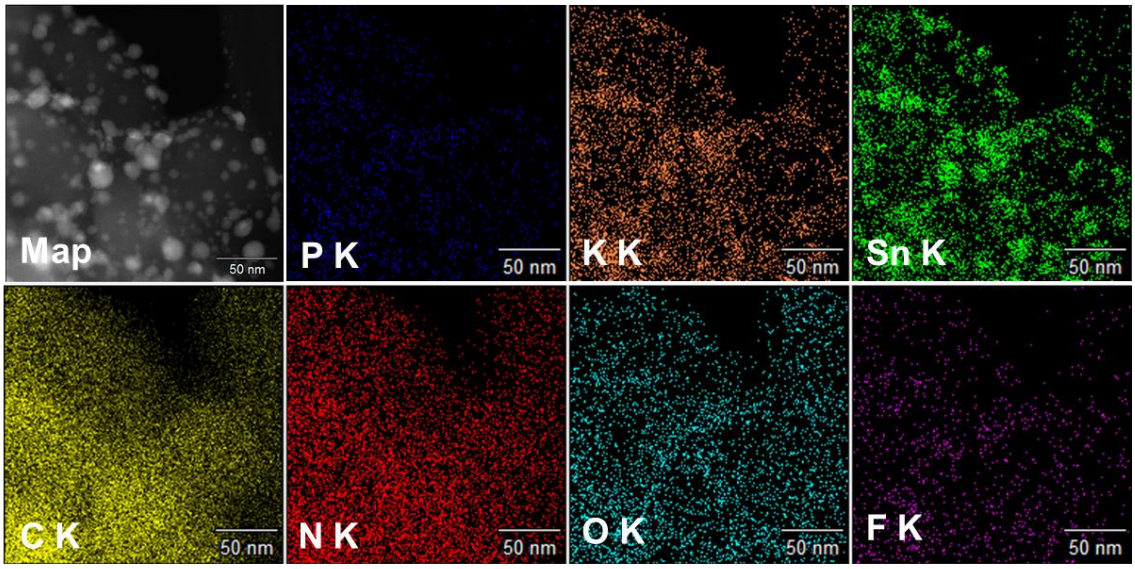

Figure 5.24. STEM-EDS mapping of the electrode after 350 cycles at 500 mA g^{-1} in KPF_6 with 5 wt. % FEC electrolyte

Ex-situ XPS tests were employed to study the composition of the SEI layer. As shown in Figure 5.19A and 5.19B, C-O and carbonyl group (CO_3) bonds were observed in the O 1s spectra, while C-C, C-O, and CO_3 bonds can be identified in the C 1s spectra. The dominant carbonyl groups can be assigned to the decomposition and reduction of carbonate solvents (EC and DEC) and FEC. In the F 1s spectra (Figure 5.19C), C-F and K-F bonds can be observed in the four electrolytes, while an extra P-F bond is observed in the KPF_6 with FEC. By detailed comparison of the peak intensities of the XPS spectra, it was found that the intensities of carbonyl group (CO_3) and K-F bonds in the electrolytes with FEC are higher than in electrolytes without FEC. Also, the

intensities of the two peaks are much stronger in KPF_6 than in KFSI electrolyte. Fourier transform infrared (FTIR) spectra of the cycled electrodes in the four electrolytes are shown in Figure 5.19D. $ROCF_3$, ROCOOH, KF, and RCF_3 can be identified for the electrodes in all of the electrolytes, and F_2S and RCH_3 can be observed for the electrodes in KFSI electrolyte. The results show that KPF_6 and FEC can increase the carbonyl group (CO_3) content and the proportion of K-F bonds, thus boosting the electrolyte decomposition and stimulating excessive side-reactions during cycling.

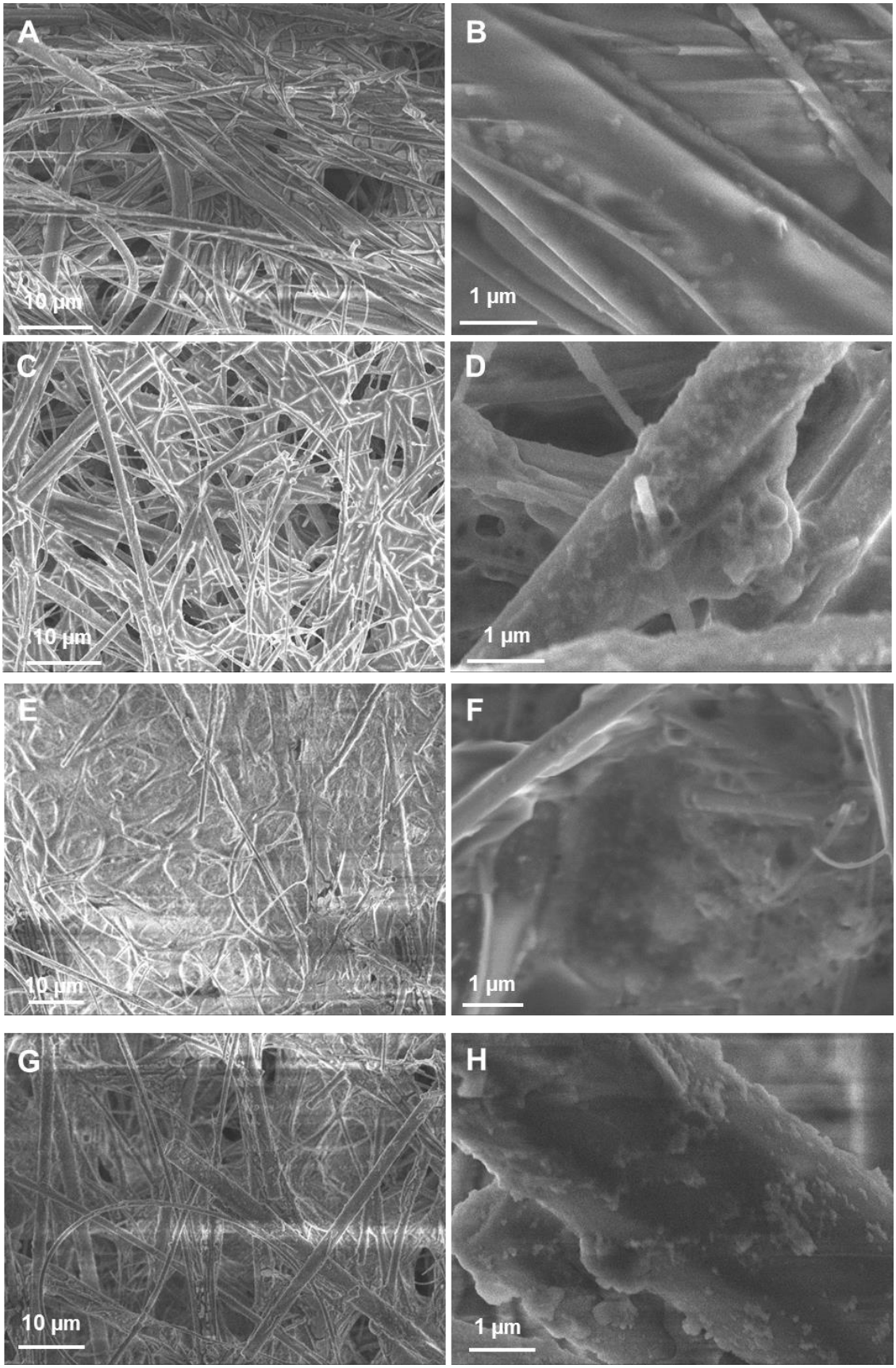
A
10 µm
B
1 µm
C
10 µm
D
1 µm
E
10 µm
F
1 µm
G
10 µm
H
1 µm

Figure 5.25. Ex-situ SEM images of the separators after 350 cycles at 500 mA g^{-1} in various electrolytes. (A-B) KPF_6, (C-D) KFSI, (E-F) KPF_6 with 5 wt. % FEC, (G-H) KFSI with 5 wt. % FEC.

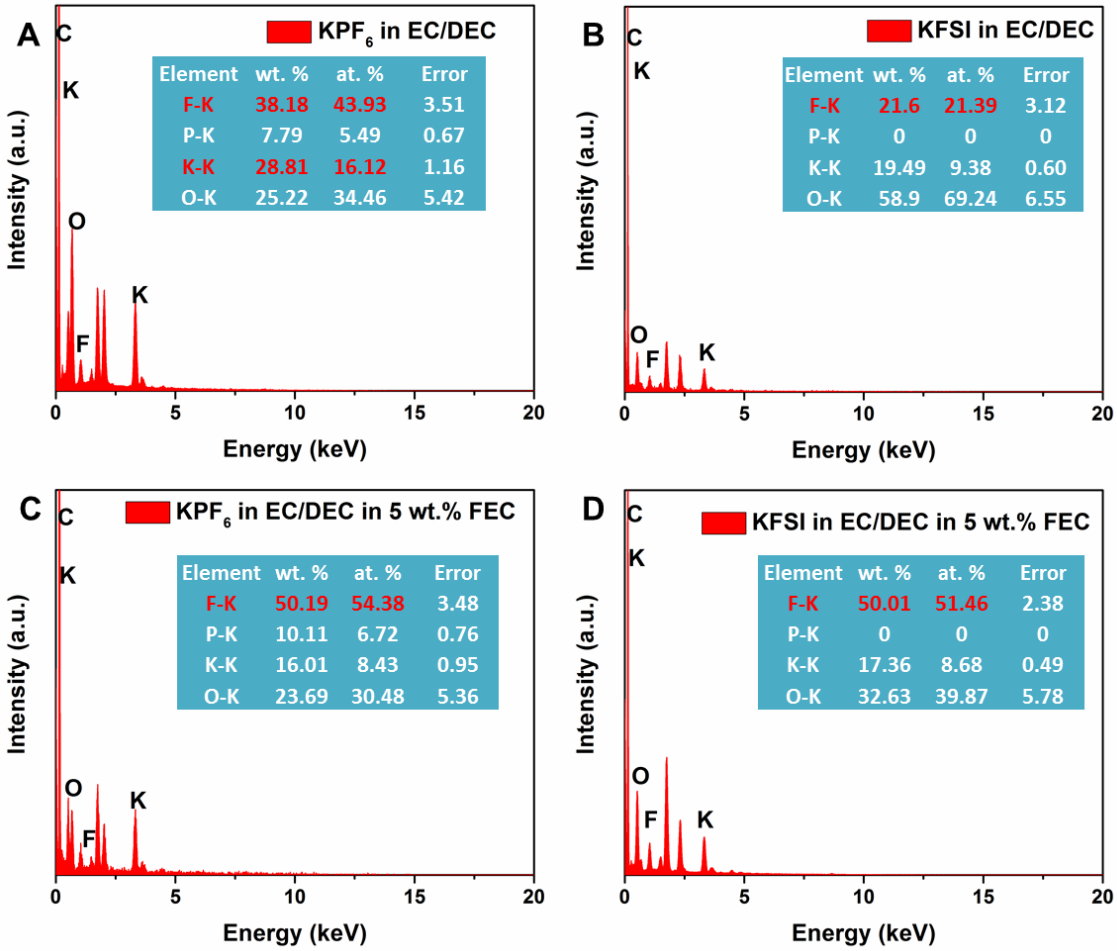

Figure 5.26. EDS elemental analysis of the separators after 350 cycles at 500 mA g^{-1} in various electrolytes. (A) KPF_6, (B) KFSI, (C) KPF_6 with 5 wt. % FEC, (D) KFSI with 5 wt. % FEC.

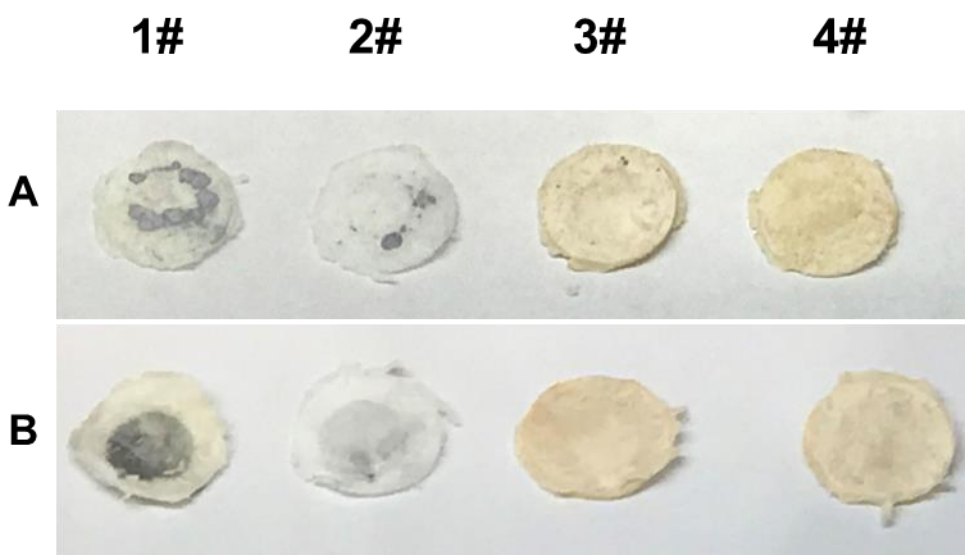

Figure 5.27. Digital photographs of the separators after 350 cycles at 500 mA g^{-1} in various electrolytes. (A) K foil side. (B) Electrode side. (Electrolytes denoted by symbols: 1# KPF_6, 2# KFSI, 3# KPF_6 with 5 wt. % FEC, 4# KFSI with 5 wt. % FEC, respectively.)

Besides the electrode surface, the separators from cells cycled for 350 cycles were also investigated. The SEM images (Figure 5.25) of the separators in electrolytes with FEC show that a layer of thin film has covered the glass fibres and that there are voids between the fibres, which may block the K ion transportation during charge/discharge cycling. For the separators cycled in electrolytes without FEC, the glass fibres maintain their morphology, with holes that can ensure the transportation of K ions. Furthermore, the EDS results (Figure 5.26) show a high content of F for the separators in the electrolyte with FEC, which is consistent with the EDS results on the surface of

the electrode. From the digital photographs of the separators cycled in electrolytes with FEC, a change from white to yellow was noticed, indicating that the electrolyte decomposition was aggravated in electrolytes with FEC. Interestingly, in KPF_6 electrolyte without FEC, the digital photographs of the separator (Figure 5.27) demonstrate that some potassium has accumulated on the surface. Some densely packed potassium, as evidenced by the EDS results, can be found in the SEM images of the separators (Figure 5.28), indicating that microscale short-circuits may have already occurred at this stage.

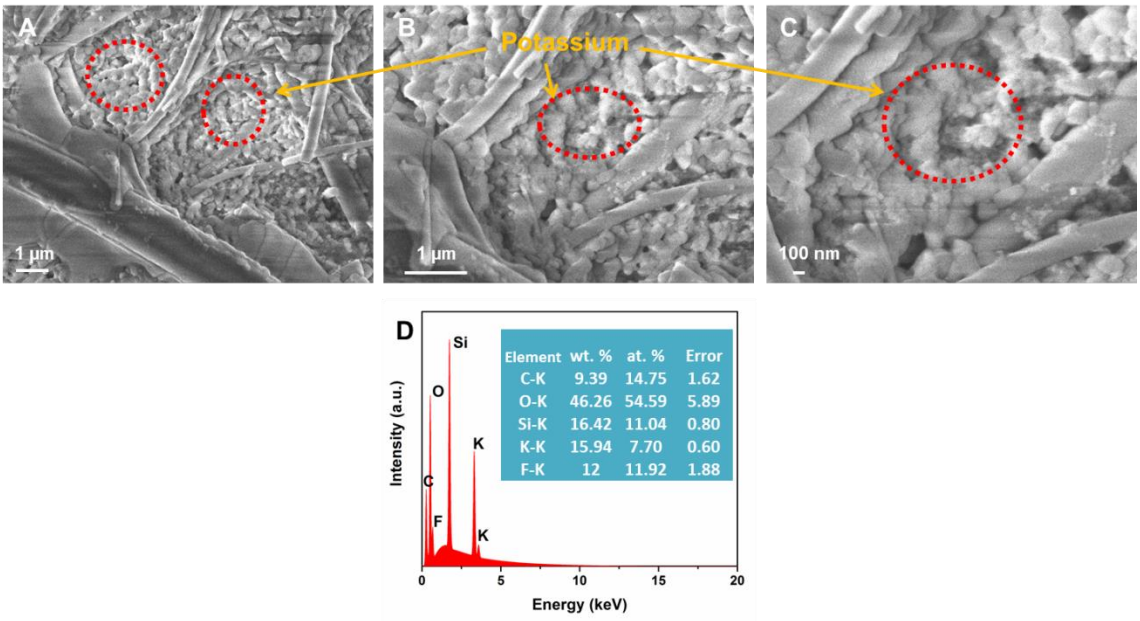

Figure 5.28. A-C) Ex-situ SEM images and D) the corresponding EDS spectrum of the separator after 350 cycles at 500 mA g^{-1} in KPF_6 electrolyte.

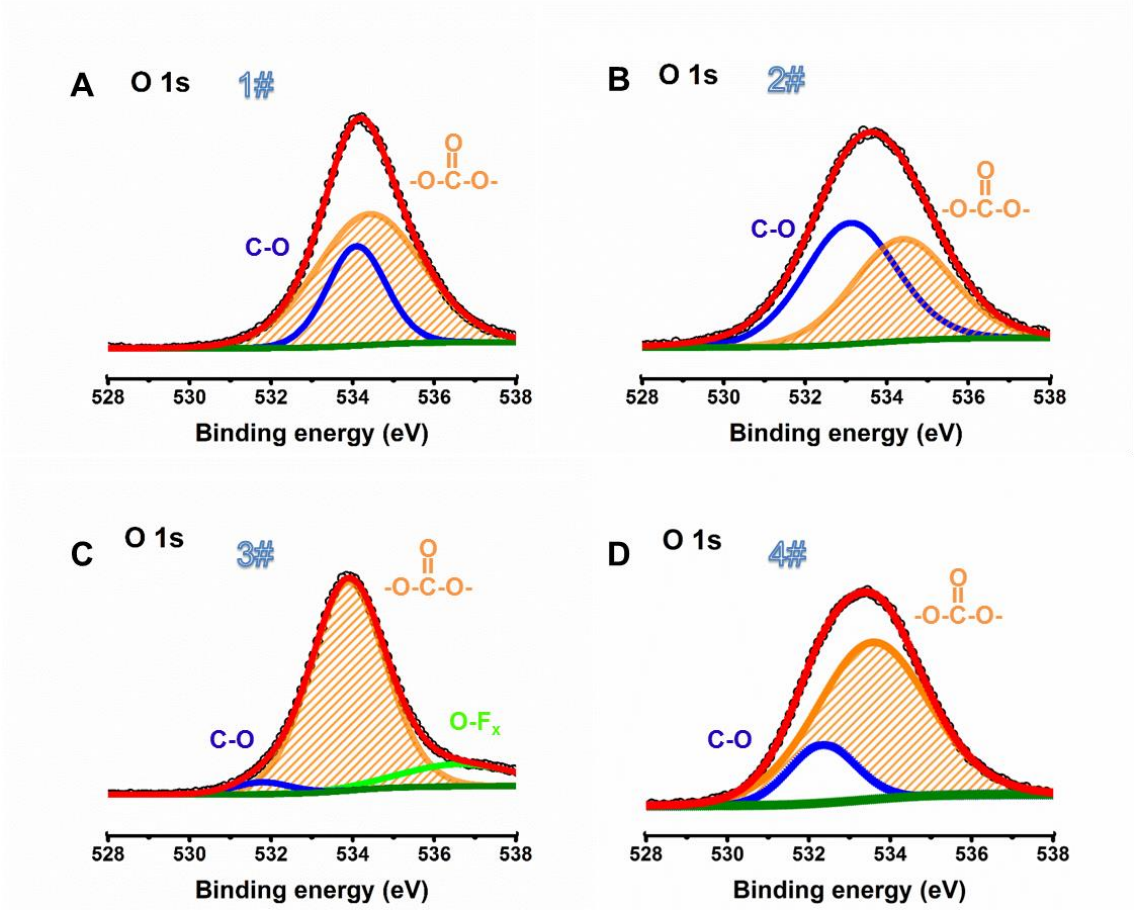

Figure 5.29. XPS spectra of O 1s for the separators in various electrolytes after 350 cycles at 500 mA g^{-1}. (Electrolytes denoted by symbols: A) 1# KPF_6, B) 2# KFSI, C) 3# KPF_6 with 5 wt. % FEC, D) 4# KFSI with 5 wt. % FEC, respectively)

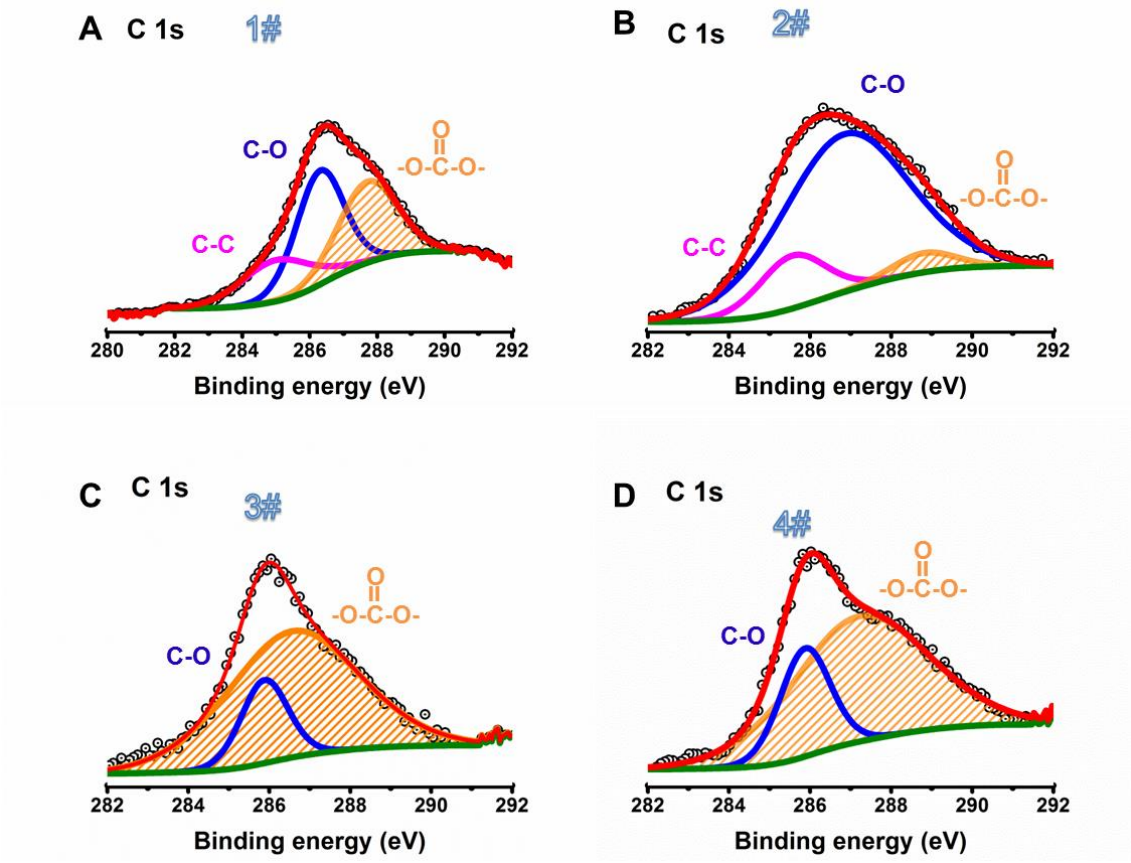

Figure 5.30. XPS spectra of C 1s for the separators in various electrolytes after 350 cycles at 500 mA g^{-1}. (Electrolytes denoted by symbols: A) 1# KPF_6, B) 2# KFSI, C) 3# KPF_6 with 5 wt. % FEC, D) 4# KFSI with 5 wt. % FEC, respectively)

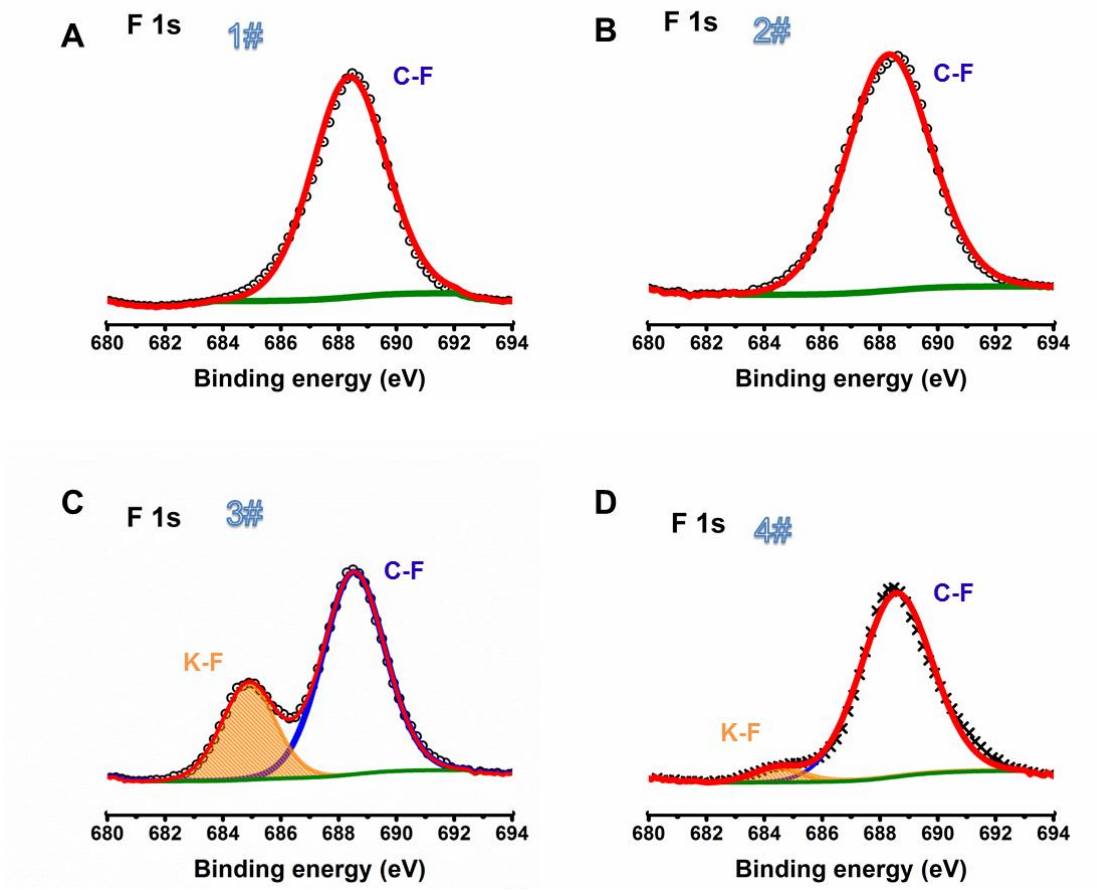

Figure 5.31. XPS spectra of F 1s for the separators in various electrolytes after 350 cycles at 500 mA g^{-1}. (Electrolytes denoted by symbols: A) 1# KPF_6, B) 2# KFSI, C) 3# KPF_6 with 5 wt. % FEC, D) 4# KFSI with 5 wt. % FEC, respectively)

As evidenced by the XPS tests (Figure 5.29 to 5.31), a similar tendency exists for carbonyl group (CO_3) and KF contents to be higher with FEC than without FEC in the electrolyte, as can be demonstrated by comparing the results after cycling in the four electrolytes, which is in good agreement with the XPS analysis of the surfaces of the electrodes.

All these observations suggest that KPF_6 and FEC additive can boost the side-reactions due to the electrolyte decomposition and produce KF, K_xPF_y, ROCOOK, F_xO, and K_2CO_3, which could significantly affect the chemical composition and stability of the SEI layer, thus influencing the cycling performance of the electrodes. In contrast, KFSI as an alternative salt could effectively help the electrode to form an even and stable SEI layer and also avoid excessive side-reactions related to electrolyte decomposition. Therefore, the KFSI electrolyte shows great advantages for constructing stable and suitable SEI films and enhancing the stability of the electrodes in PIBs.

5.3.5. *In-operando* XRD mechanistic study of Sn_4P_3 as anode for PIBs

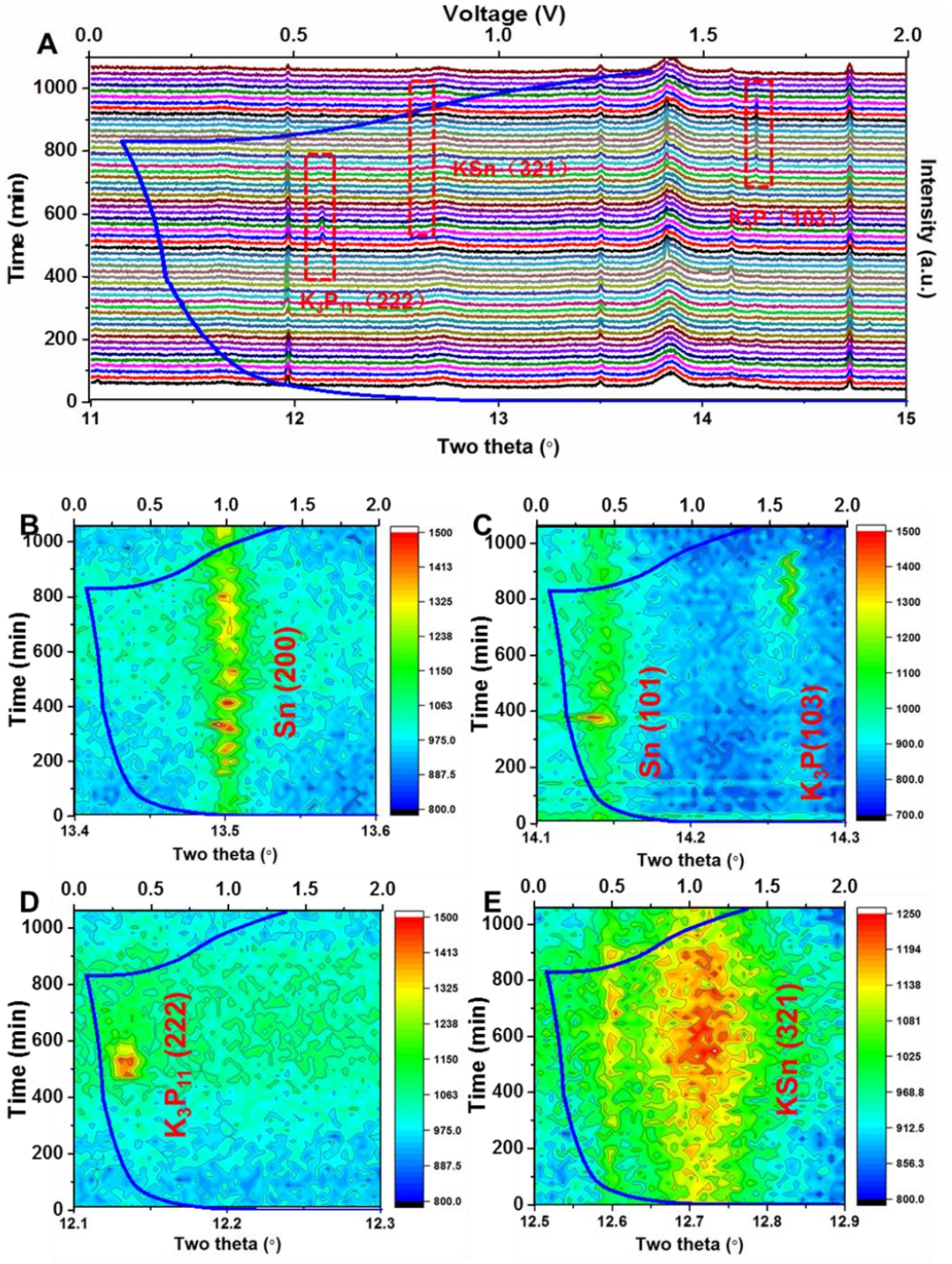

Figure 5.32. Electrochemical reaction mechanism study of Sn_4P_3 as anode for PIBs.

(A) *In-operando* synchrotron XRD patterns of Sn_4P_3 as anode for PIBs. (B-E) Contour plots of *in-operando* synchrotron X-ray powder diffraction with superimposed voltage profiles shown for selected 2θ ranges.

To understand the electrochemical reaction mechanism of Sn_4P_3 as anode for PIBs, *in-operando* synchrotron XRD (λ = 0.688273 Å) data were collected via the Powder Diffraction Beamline at the Australian Synchrotron. The *in-operando* diffraction data for the Sn_4P_3 cell in the first cycle are stacked along with the charge-discharge profile and presented in Figure 5.32A. During the discharge (potassiation) process, a reflection at 12.14 °, corresponding to K_3P_{11} (222), first emerges at ~0.21 V and disappears at ~0.17 V. Following this, the K_3P_{11} (222) reflection disappears, and two new reflections at 12.71 and 14.27 °, assigned to KSn (321) and K_3P (103), were observed, showing good agreement with the previously reported ex-situ studies [16]. During the charging (depotassiation) process, the KSn (321) and K_3P (103) reflections disappear with increasing potential, supporting the reversibility of the reactions for potassiation and depotassiation.

To further investigate the phase transition behaviour from the initial stage until the appearance of K_3P_{11} phase, contour plots of the operando data corresponding to each main phase are presented in Figure 5.32B-E. The peak intensities of Sn (200) at 2θ = 13.51° and Sn (101) at 2θ = 14.15° increased with the decreasing voltage until around 0.4 V, which indicates that P initially precipitates from Sn_4P_3 and reacts with potassium to form P-K_x phase in an amorphous state. Upon further discharge, the peak

intensities of the Sn (200) and Sn (101) reflections are weakened, while the intensities of the K_3P_{11} (222) and KSn (321) peaks increase. In addition, the intensity of the KSn (321) peak appears to be the highest when the peak intensity of Sn (101) is significantly reduced.

According to these results, it is believed that the potassiation process could be described by the following equations:

$$Sn_4P_3 + 3K_x \leftrightarrow 4Sn + 3(P\text{-}K_x) \text{ (amorphous)} \quad (1)$$

$$11(P\text{-}K_x) + yK \leftrightarrow K_3P_{11} \ (11x + y = 3) \quad (2)$$

$$K_3P_{11} + Sn + 31K \leftrightarrow KSn + 11K_3P \quad (3)$$

In the initial discharged stage, Sn_4P_3 breaks into Sn particles, and the P component precipitates in amorphous form to react with potassium (Reaction (1)). Upon potassiation, a conversion reaction occurs, where P reacts with potassium to form K_3P_{11} (Reaction (2)). In the following Reaction (3), Sn is alloyed completely with K to form KSn phase, and K_3P_{11} is further potassiated to form K_3P phase. Therefore, the synergistic K-storage reactions of K-P phases (K_3P_{11}, K_3P) and K-Sn (KSn) alloys during the discharge process create mutual buffers to alleviate the volume changes during cycling.

5.4. Conclusion

Sn_4P_3 as a promising high capacity electrode material for PIBs was synthesized through a scalable ball-milling method and further modified by confining the as-milled particles in carbon fibre through the electrospinning technique. This design not only offers a feasible avenue for the large-scale fabrication of phosphorus-based electrode materials with a relatively simple synthesis strategy, but also takes advantage of the one-dimensional carbon fibre, addressing the volume expansion problem to improve electrochemical performance. *In-operando* synchrotron XRD studies were first carried out to reveal the electrochemical reaction mechanism of Sn_4P_3 as anode for PIBs. The investigations suggest that K-P (K_3P_{11} and K_3P) and K-Sn (KSn) phases are formed during the discharge process, with these phases acting as mutual buffers to alleviate the volume changes during cycling.

The effects of an alternative potassium salt (KFSI) and FEC additive in the electrolyte for PIBs were also investigated. A stable SEI layer is crucial for enhancing the cycling performance of batteries, and FEC has been demonstrated to improve the electrochemical performance of SIBs. In this work, however, FEC stimulates excessive side reactions and accelerates the consumption of the electrolyte, resulting in uneven SEI layer formation and electron distribution, which boost the potassium dendrite growth. Therefore, it greatly increases the polarization and slows down the reaction dynamics during cycling of PIBs. In contrast, KFSI plays a critical role in suppressing the growth of potassium dendrites and reducing the effects of polarization,

so it can effectively generate a uniform SEI layer and allow stable cyclability at high current density.

This work reports scalable and low-cost production method for Sn_4P_3@C fibres with excellent anodic performance for the K-ion battery. It is believed that these key findings offer deep insights to inspire robust developments in exploring phosphorus-based anode materials in PIBs through materials design and manipulation of the salt/additive chemistry of the electrolytes.

5.5. References

[1] B. Dunn, H. Kamath, J.-M. Tarascon, *Science* **2011**, 334, 928.

[2] L. Liu, Y.-X. Yin, J.-Y. Li, N.-W. Li, X.-X. Zeng, H. Ye, Y.-G. Guo, L.-J. Wan, *Joule* **2017**, 1, 563.

[3] C. Yang, J. Chen, T. Qing, X. Fan, W. Sun, A. von Cresce, M. S. Ding, O. Borodin, J. Vatamanu, M. A. Schroeder, *Joule* **2017**, 1, 122.

[4] J. Sun, H.-W. Lee, M. Pasta, H. Yuan, G. Zheng, Y. Sun, Y. Li, Y. Cui, *Nature nanotechnology* **2015**, 10, 980.

[5] D.-S. Bin, Z.-X. Chi, Y. Li, K. Zhang, X. Yang, Y.-G. Sun, J.-Y. Piao, A.-M. Cao, L.-J. Wan, *Journal of the American Chemical Society* **2017**, 139, 13492.

[6] N. Yabuuchi, K. Kubota, M. Dahbi, S. Komaba, *Chemical reviews* **2014**, 114, 11636.

[7] Z. Jian, W. Luo, X. Ji, *Journal of the American Chemical Society* **2015**, 137, 11566.

[8] H. Gao, T. Zhou, Y. Zheng, Q. Zhang, Y. Liu, J. Chen, H. Liu, Z. Guo, *Advanced Functional Materials* **2017**, 27, 1702634.

[9] X. Wu, D. P. Leonard, X. Ji, *Chemistry of Materials* **2017**, 29, 5031.

[10] C. Chen, Z. Wang, B. Zhang, L. Miao, J. Cai, L. Peng, Y. Huang, J. Jiang, Y. Huang, L. Zhang, *Energy Storage Materials* **2017**, 8, 161.

[11] Y. Liu, Z. Tai, Q. Zhang, H. Wang, W. K. Pang, H. K. Liu, K. Konstantinov, Z. Guo, *Nano Energy* **2017**, 35, 36.

[12] Y. Kim, Y. Park, A. Choi, N. S. Choi, J. Kim, J. Lee, J. H. Ryu, S. M. Oh, K. T. Lee, *Advanced materials* **2013**, 25, 3045.

[13] Y. Kim, Y. Kim, A. Choi, S. Woo, D. Mok, N. S. Choi, Y. S. Jung, J. H. Ryu, S. M. Oh, K. T. Lee, *Advanced Materials* **2014**, 26, 4139.

[14] J. Liu, P. Kopold, C. Wu, P. A. van Aken, J. Maier, Y. Yu, *Energy & Environmental Science* **2015**, 8, 3531.

[15] J. Fullenwarth, A. Darwiche, A. Soares, B. Donnadieu, L. Monconduit, *Journal of Materials Chemistry A* **2014**, 2, 2050.

[16] W. Zhang, J. Mao, S. Li, Z. Chen, Z. Guo, *Journal of the American Chemical Society* **2017**, 139, 3316.

[17] W. K. Pang, S. Kalluri, V. K. Peterson, N. Sharma, J. Kimpton, B. Johannessen, H. K. Liu, S. X. Dou, Z. Guo, *Chemistry of Materials* **2015**, 27, 3150.

[18] K. Gong, F. Du, Z. Xia, M. Durstock, L. Dai, *science* **2009**, 323, 760.

[19] M. D. Slater, D. Kim, E. Lee, C. S. Johnson, *Advanced Functional Materials* **2013**, 23, 947.

[20] H.-M. Cho, W.-S. Choi, J.-Y. Go, S.-E. Bae, H.-C. Shin, *Journal of Power Sources* **2012**, 198, 273.

[21] M. R. Palacin, *Chemical Society Reviews* **2009**, 38, 2565.

[22] P. Simon, Y. Gogotsi, B. Dunn, *Science* **2014**, 343, 1210.

[23] N. Singh, T. S. Arthur, C. Ling, M. Matsui, F. Mizuno, *Chemical Communications* **2013**, 49, 149.

[24] Z. Jian, Z. Xing, C. Bommier, Z. Li, X. Ji, *Advanced Energy Materials* **2016**, 6, 1501874.

[25] J. Zhou, L. Wang, M. Yang, J. Wu, F. Chen, W. Huang, N. Han, H. Ye, F. Zhao, Y. Li, *Advanced Materials* **2017**, 29, 1702061.

[26] V. Lakshmi, Y. Chen, A. A. Mikhaylov, A. G. Medvedev, I. Sultana, M. M. Rahman, O. Lev, P. Prikhodchenko, A. M. Glushenkov, *Chemical Communications* **2017**, 53, 8272.

[27] I. Sultana, T. Ramireddy, M. M. Rahman, Y. Chen, A. M. Glushenkov, *Chemical Communications* **2016**, 52, 9279.

[28] Y. Dong, Z.-S. Wu, S. Zheng, X. Wang, J. Qin, S. Wang, X. Shi, X. Bao, *ACS nano* **2017**, 11, 4792.

[29] H. Wang, D. Lin, Y. Liu, Y. Li, Y. Cui, *Science Advances* **2017**, 3, e1701301.

[30] C.-P. Yang, Y.-X. Yin, S.-F. Zhang, N.-W. Li, Y.-G. Guo, *Nature communications* **2015**, 6, 8058.

Chapter 6

6. Unraveling the effect of salt chemistry on long-durability high-phosphorus-concentration anode for potassium ion batteries

6.1. Introduction

With the increased demands of electric cars and large-scale energy storage devices, high-energy density and low-cost batteries have been of great interest for the past few years [1-7]. While lithium ion batteries (LIBs) have dominated in portable devices and electric vehicles for decades, there is still considerable debate as to whether our limited lithium resources can meet the requirements for scalable application in grid-level storage [8-11]. Hence, it is necessary to broaden our research interest to consider cost-effective alternatives. Due to this concern, the other group-I elements (Na and K) have attracted the focus of attention because of their similar properties to Li and greater abundance in the Earth's crust[12-15]. The standard hydrogen potential (-2.71 V vs. E ⁰) of Na, however, usually translates into a lower working voltage than that of Li in full cells, indicating that lower energy density is achieved in sodium ion batteries (SIBs)[16-17]. Potassium, with abundant resources and a low standard hydrogen potential (-2.93 V vs. E^0), close to that of lithium (-3.04 V vs. E^0), makes potassium ion batteries (PIBs) a good candidate to replace LIBs[18-20].

Carbon-based anode materials have been extensively studied for reversible K-ion storage with excellent cycling performance[21-22], although their low volumetric capacity and energy density due to their low theoretical capacity are still obstacles for industrial applications[23]. Phosphorus as an alternative anode material has attracted numerous studies because of its high theoretical capacity (2594 mA h g^{-1})[24]. In order to overcome the drawbacks of the low electrical conductivity of phosphorus and large volume changes during cycling, alloy-based phosphides (NiP_2, Se_4P_4, Sn_4P_3, SnP_3, etc. [25-29]) have been introduced because of the metallic feature in these compounds and their synergistic reaction mechanisms[27, 30]. Although these phosphides have demonstrated promising cycling performance, their low P atomic percentages still limit their capacity. Recently, GeP_5 has been reported as a potential anode with the highest P atomic percentage among all the binary phosphides. Although Ge may have high costs compared with other metal such as Sn, GeP_5 possess not only comparable low costs (only 16.7% atomic percentage of Ge in the compound) but also exhibits a very large specific gravimetric capacity. Combined with a density of 3.65 g cm^{-3}, a high volumetric capacity of 6865 mA h cm^{-3} could be obtained, which would be beneficial for its application. In addition, GeP_5 exhibits a layered structure similar to those of black P and graphite, and its electronic conductivity is 4 orders of magnitude higher than that of black P and similar to that of graphite, being favourable for potassium ion storage [31].

Herein, layered phosphorus-like GeP_5 compound was prepared and evaluated its

electrochemical performance as an anode for PIBs. Moreover, to further improve the coulombic efficiency (CE) and cycling stability, an alternative potassium salt, potassium bis(fluorosulfonyl)imide (KFSI), was employed to help the electrode form an even solid electrolyte interphase (SEI) layer and suppress the excessive side reactions. The GeP_5 electrode in KFSI-ethylene carbonate/ diethyl carbonate (EC/DEC) electrolyte exhibited outstanding long-term cyclability (213.7 mA h g^{-1} over 2000 cycles) at the current density of 500 mA g^{-1}. To the best of the knowledge, the obtained anodic cycling performance in K storage exceeds those of all the alloy-based anodes. The reaction mechanism of GeP_5 as anode in PIBs was first investigated by *in-operando* synchrotron X-ray diffraction (XRD). The suggested conversion-type ($P \rightarrow K_4P_3$) and alloy-type ($Ge \rightarrow KGe$) reactions synergistically buffer the volume changes during cycling, thus enhancing the integrity of the electrodes.

.

6.2. Experimental Section

6.2.1. Preparation of GeP_5 powder:

GeP_5 powder was obtained by a high-energy ball-milling (HEBM, Fritsch Pulverisette-6. Germany) process using commercial Ge and red phosphorus as the raw materials in the mole ratio of Ge: P = 1: 5. The HEBM was conducted at 500 rpm for 10 h, and the elemental mixture was milled using ball-mill beads 10 mm in diameter with a powder-to-ball weight ratio of 1:20. All sample storage and handling were

performed in an Ar filled glove box (MBraun Unilab).

6.2.2. Materials characterization

The crystal structures of the as-prepared powders were characterized by powder X-ray diffraction (XRD) on a GBC MMA diffractometer with a Cu Kα source at a scanning rate of 1 °min^{-1}. The morphology of the as-synthesized powders was characterized on a JEOL JSM-7500FA field-emission scanning electron microscope (FESEM) and a JEOL ARM-200F aberration-corrected transmission electron microscope (TEM). A customized CR2032 coin cell was made for use in synchrotron X-ray powder diffraction (SXRPD) experiments, and the details of cell assembly can be found elsewhere[32]. The cell was galvanostatically discharged and charged over 0.01–3 V vs. K^+/K. Synchrotron X-ray powder diffraction (SXRPD) experiments were conducted on the Powder Diffraction beamline at the Australian Synchrotron, where the collection time for each data point was 180 seconds and the time gap between each collection was ~7.5 minutes during discharging and charging using a MYTHEN microstrip detector. The wavelength of synchrotron radiation was determined to be 0.68899 Å using LaB_6 (Standard Reference Material SRM 660b).

Fourier-transform infrared (FTIR) maps were collected using a PerkinElmer Spotlight 400 equipped with a mercury cadmium tellurium (MCT) detector, which consists of single point (point mode) and 16-array (image mode) detectors all in one. Maps of 2 × 8 points (~200 × 100 μm^2 area) in reflectance mode were acquired at 4 cm^{-1} resolution with 16 scans per pixel from 4000 to 400 cm^{-1}. The drop down

average true range (ATR) is a Ge crystal 100 μm in diameter. Principal component analysis (PCA) is one of the most widely used methods for data reduction and exploratory analysis. In this work, PCA analyses of the selected FTIR regions corresponding to the 400 - 4000 cm^{-1} range were obtained to reveal the uniformity of the functional groups and solid electrolyte interphase (SEI) layer.

6.2.3. Theoretical calculations

The calculations were performed based on the density functional theory (DFT) approach [33] using the $DMol^3$ package. The effects of exchange correlation interaction were treated according to the Perdew-Burke-Ernzerhof generalized-gradient approximation (GGA-PBE) [34]. All-electron Kohn-Sham wave functions were expanded in a double numerical basis with polarized orbital (DNP) [35]. Sampling of the irreducible wedge of the Brillouin zone was performed with a regular Monkhorst-Pack grid of special k-points [36]. The convergence criteria for relaxation were 1.0×10^{-5} Ha, 0.002 Ha/Å, and 0.005 Å for the energy, gradient, and atomic displacement, respectively.

The ion solvation is directly related to the strength of the ion-solvent interaction that governs the solvation structure. In addition, it plays an important role in determining the energetics of ion intercalation from the liquid electrolyte into the battery electrodes, since the desolvation is required for intercalation[37-38]. The ion solvation energies were approximated from the binding energy of the $X^+(Y)$ clusters,

where X = K^+ or Na^+, and Y = EC + DEC or EC + DEC + FEC. In particular

$$\Delta E_{sol} = E_{X^+} + E_{(Y)} - E_{X^+(Y)} \quad \text{(I)}$$

where E_{X^+}, $E_{(Y)}$, and $E_{X^+(Y)}$ are the energies of the X^+ in vacuum, and the (Y) and X^+(Y) clusters, respectively [39].

6.2.4. TXM characterization

In-operando transmission X-ray microscopy (TXM) measurements of the GeP_5 used as anode in LIBs were carried out at the 01B1 beamline of the National Synchrotron Radiation Research Center (NSRRC) in Hsinchu City, Taiwan. The light source operates with photon energy ranging between 8 and 11 keV. The X-rays passing through the tested coin cell go through a zone plate optical system and then a phase ring to form the image.

The electrochemical testing was carried out by using a 2032-type coin cell with a hole in the stainless steel disk, top, and bottom cap. The working electrode consisted of GeP_5, conductive additives, and binder in the weight ratio of 40:40:20. The conductive additives included graphitic flakes (KS6, 3 lm, Timcal) and carbon black (Super P, 40 nm, Timcal). Lithium polyacrylate was chosen as binder because of its multifunctional nature and good properties for high-voltage Li-ion batteries. The GeP_5 electrode was prepared by coating the slurry on a disk. Once the film dried, the layer was removed from the substrate, creating a free-standing film. The free-standing electrode was further dried under vacuum overnight to remove residual solvent. The

counter electrode was Li foil, which is mostly transparent to X-rays. The electrolyte was a 1 M solution of $LiPF_6$ in ethylene carbonate/ethyl methyl carbonate (1:2 vol. %). The covers of both sides of the cell were sealed with Kapton tapes in order to allow the X-ray beam to pass through the cell. The cell-assembly processes were conducted in a glove box, where oxygen and water levels were kept lower than 1 ppm.

The charge/discharge tests were carried out in constant current (CC) mode within the voltage window from 3 V down to 0.005 V under the current density of 0.3 A g^{-1}. All the potentials reported herein are referenced to Li/Li^+.

6.2.5. Electrochemical measurements

Electrodes were fabricated using a slurry-coating method. The synthesized materials (GeP_5) were mixed with Super P carbon black and poly(acrylic acid) (PAA) in the weight ratio of 3:5:2, respectively. Deionized (DI) water was used as the dispersing agent. Then, the slurry was coated on copper foil and dried in a vacuum oven at 80 ℃ overnight. Coin-type (CR2032) cells were assembled in an argon-filled glove box with oxygen and water content lower than 0.1 ppm. K half-cells were assembled with potassium metal and 0.8 M KPF_6 or 1 M KFSI in an EC/DEC solution (EC: DEC = 1:1, v/v) as electrolyte. FEC (5 wt. %) as an additive was added into the electrolyte for comparison purposes. The cells were galvanostatically charged-discharged between 0.01 and 3.0 V versus K/K^+ at various current densities on a Neware tester.

6.3. Results and Discussion

6.3.1. Characterization of GeP_5

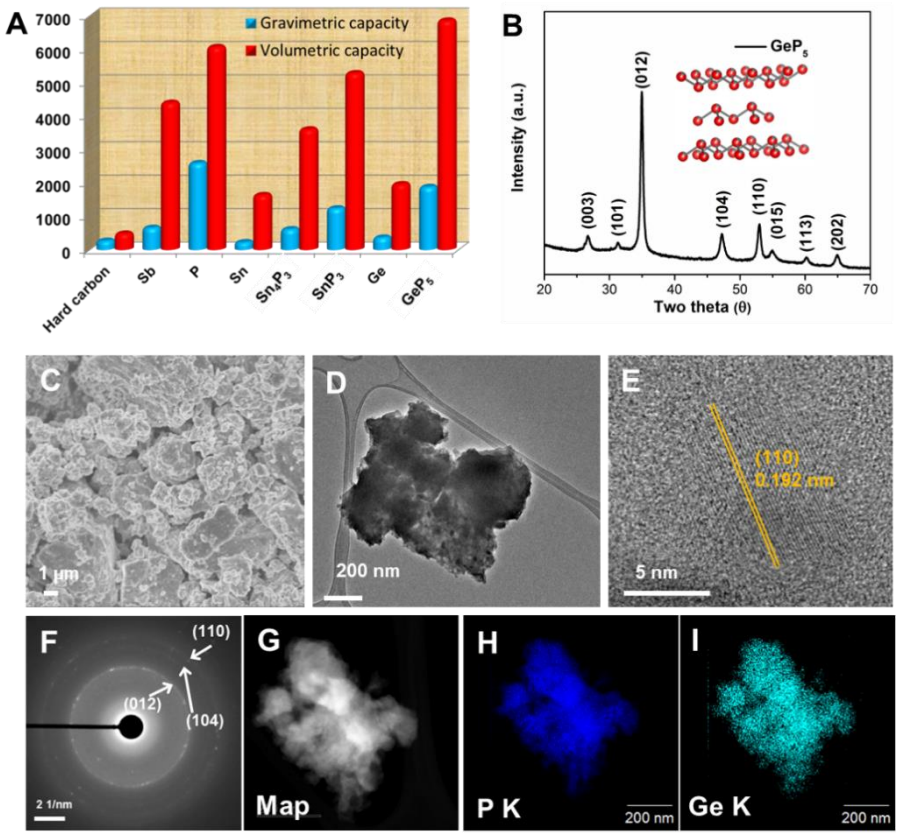

Figure 6.1. Characterization of GeP_5. **(**A) Theoretical gravimetric and volumetric capacities for various anode materials in K-ion batteries. (B) XRD pattern of the GeP_5 powder (with the inset showing the crystal model for GeP_5). (C) SEM image, (D) TEM image, (E) HRTEM image, (F) selected area diffraction pattern, and (G-I) the STEM-EDS mapping of GeP_5 powder.

P can react with K to form K_3P, leading to a high capacity (2596 mA h g^{-1}), which is

the highest theoretical capacity among the anodes for PIBs reported so far. The low conductivity of red phosphorus, however, and the large volume variation during cycling are blocking its application as anode material. By the introduction of Ge metal with high electrical conductivity, GeP_5 with its high phosphorus concentration has a high theoretical gravimetric capacity. As shown in Figure 6.1A, GeP_5 also exhibits the highest theoretical volumetric capacity among the alloy-based anodes. The GeP_5 compounds were obtained by high-energy ball-milling of Ge and red phosphorus mixtures. All of the diffraction peaks in the XRD pattern of the as-milled sample (Figure 6.2B) can be assigned to GeP_5 ($R\bar{3}m$, PDF No.00-024-0455) with a layered structure (inset of Figure 6.2B). No impurities were detected, implying that Ge and P were completely reacted and transformed to GeP_5 phase. The broadened diffraction peaks indicate that the GeP_5 is in nanocrystalline form. The field-emission scanning electron microscope (FESEM) image (Figure 6.2C) shows the morphology, consisting of irregular agglomerated microsized particles, and the transmission electron microscope (TEM) image (Figure 6.2D) presents the secondary particles, which appear as agglomerations of nanoparticles. Figure 6.2E shows that the spacing of the fringes is 0.283 nm, which matches the d_{110} spacing of GeP_5. The corresponding selected area diffraction (SAED) pattern (Figure 6.2F) can be indexed to the (012), (104), and (110) planes of GeP_5. The scanning TEM − energy dispersive spectroscopy (STEM-EDS) elemental mapping images exhibit the uniform distributions of the Ge and P in the as-prepared particles, as shown in Figure 6.2G-I.

6.3.2. Electrochemical characterization and analysis of GeP_5 anode

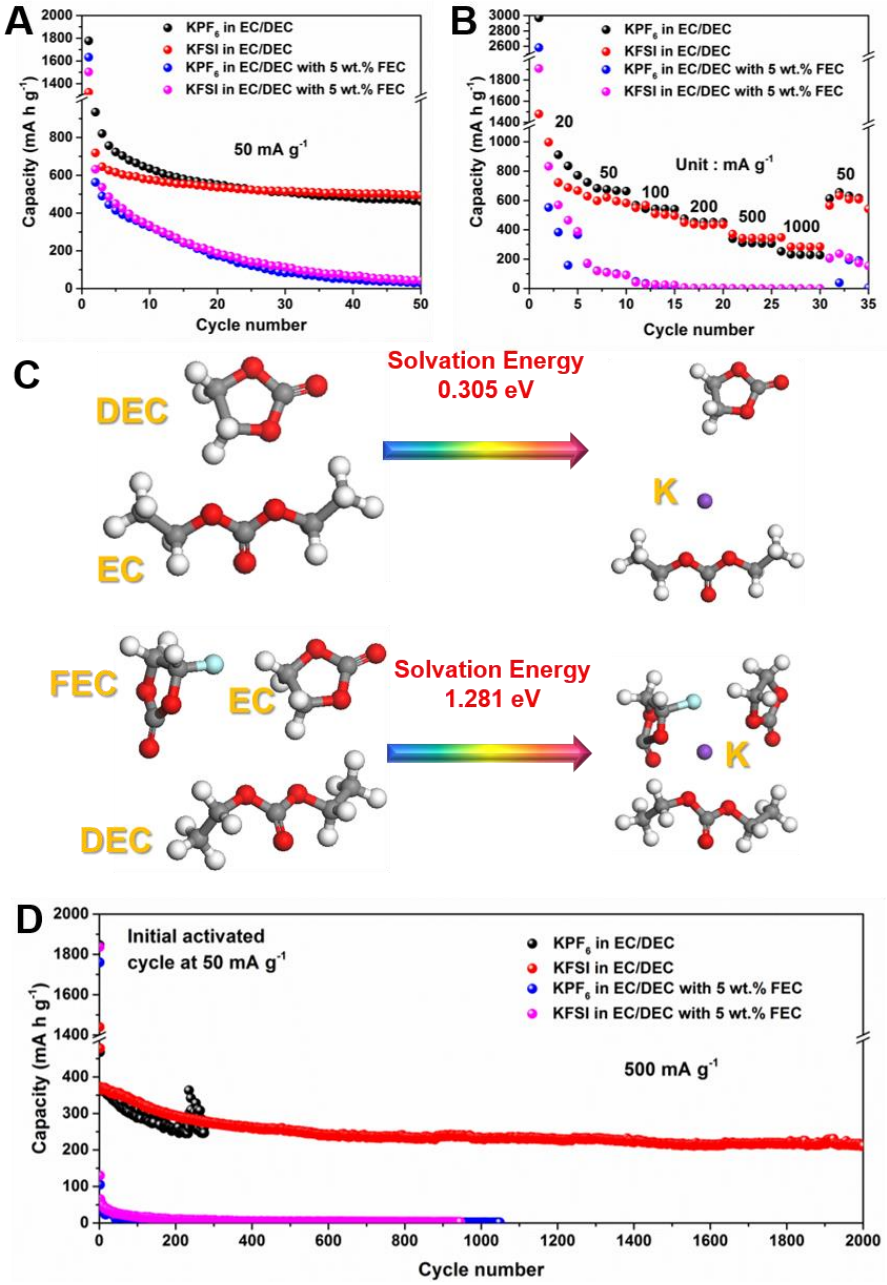

Figure 6.2. Electrochemical performance of GeP_5 as anode for PIBs. (A) Cycling performances of cells with various electrolytes at 50 mA g^{-1}. (B) Rate capabilities of cells at various current densities.(C) Solvation energies estimated from the binding

energy of the K^+(Y) clusters, where Y = EC + DEC or EC + DEC + FEC. (D) Long-term cycling performance of the cells with various electrolytes at 500 mA g^{-1}.

As shown in Figure 6.2A, the GeP_5 electrode exhibited an attractive reversible specific capacity (934.5 mA h g^{-1}) at the second cycle with a slow drop afterwards in KPF_6 electrolyte. The initial CE is only 45.81%, however, which is possibly due to the high irreversible capacity caused by the SEI layer formation and the possible side reactions caused by the highly-reactive potassium metal[40]. To address the problem of low initial CE and suppress the side reactions during cycling, an alternative potassium salt (KFSI) was adopted[40-41]. The GeP_5 electrode in KFSI electrolyte presents a relatively high initial CE of 58.57% and stable cycling performance, with retained capacity of 495.1 mA h g^{-1} after 50 cycles at 50 mA g^{-1}. The GeP_5 electrode in KFSI electrolyte also shows superior rate performance (Figure 6.2B), delivering 721.8, 595.2, 503.7, 438.5, 343.9, and 284.2 mA h g^{-1} at the current densities of 20, 50, 100, 200, 500, and 1000 mA g^{-1}, respectively. In order to further improve the electrochemical performance of the GeP_5 electrodes, fluoroethylene carbonate (FEC) was adopted as an additive, inspired by its application in sodium ion batteries (SIBs)[17, 42-44]. With the addition of 5 wt. % FEC to both KFSI-EC/DEC and KPF_6-EC/DEC electrolytes, however, the specific capacity dropped quickly after a few cycles at 50 mA g^{-1}, and the capacity was almost zero at high current densities. To further investigate the effect of FEC additive in the electrolyte, density functional

theory (DFT) calculations were employed to obtain the solvation energies in order to understand the interaction between Na^+/K^+ and the solvent in the electrolyte. The solvation energy in the electrolyte without FEC is notably smaller (0.305 eV) than that in the electrolyte with FEC (1.281 eV) for PIBs (Figure 6.2C), indicating that the interaction between K^+ and the solvent is weaker in the electrolyte without FEC, and therefore, the K ion diffusion in the electrolyte and the desolvation could be easier, which makes the following reaction with GeP_5 easier than in the electrolyte with FEC. Based on the DFT calculations (solvation energy), it is apparent that FEC as an additive in PIBs has a negative effect on the electrochemical performance. This seems to be in conflict with the reported effect of FEC as additive in SIBs. The solvation energies in electrolyte for sodium ion batteries were also calculated. As can be seen in Figure 6.3, the solvation energy increased from 0.395 eV to 0.632 eV with the addition of FEC, although the solvation energy in SIBs with FEC (0.632 eV) is much smaller than that in PIBs with FEC (1.281 eV). Also, the FEC, based on reported data[17, 45-47], can help to form a uniform and stable SEI layer on the surface of the electrode, which leads to enhanced cycling performance.

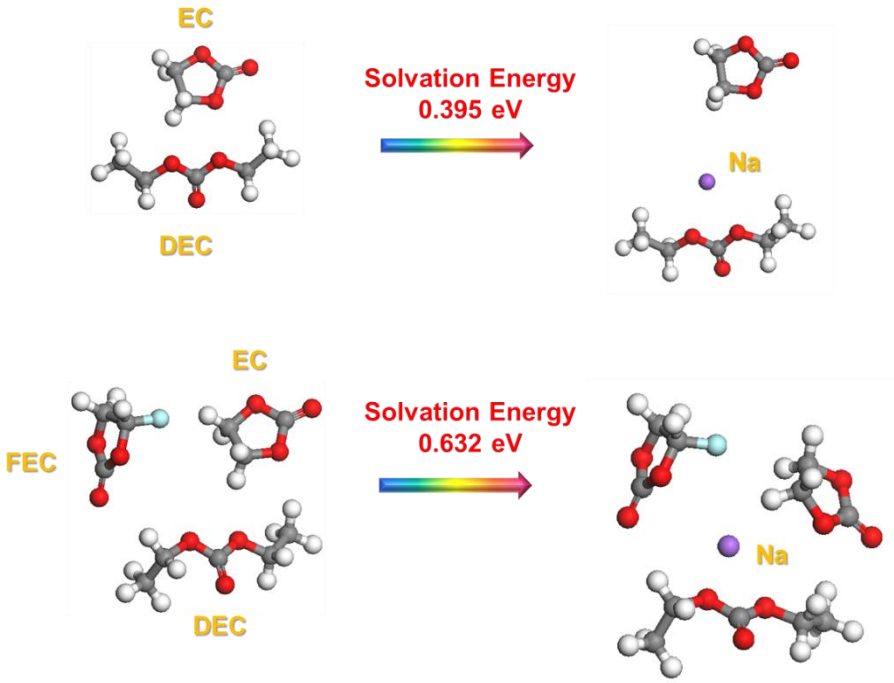

Figure 6.3. Solvation energies estimated from the binding energy of the $Na^{+}(Y)$ clusters, where Y = EC + DEC or EC + DEC + FEC.

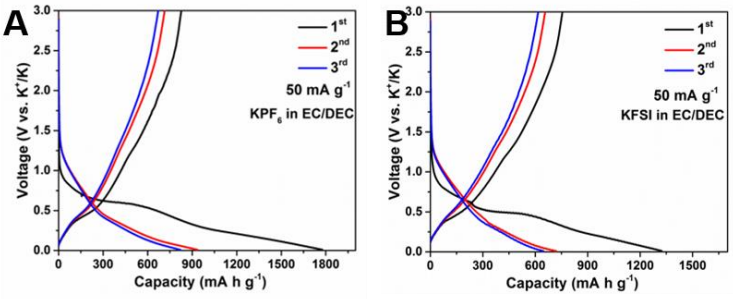

Figure 6.4. Galvanostatic discharge and charge profiles for the first 3 cycles of the electrode in (A) KPF_6 and (B) KFSI electrolyte at 50 mA g^{-1}.

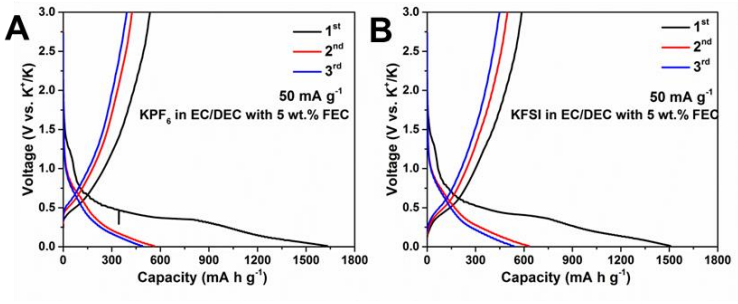

Figure 6.5. Galvanostatic discharge and charge profiles for the first 3 cycles of the electrode in (A) KPF_6 and (B) KFSI electrolyte with 5 wt. % FEC at 50 mA g^{-1}.

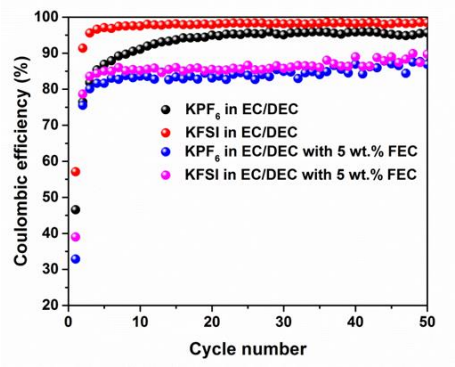

Figure 6.6. Coulombic efficiency of the GeP_5 electrode in various electrolytes.

The galvanostatic discharge/charge profiles of GeP_5 electrodes for the first three cycles in KPF_6 and KFSI electrolytes at 50 mA g^{-1} are shown in Figure 6.4. A large irreversible capacity can be found in the first cycle, especially in KPF_6 electrolyte, leading to a lower initial CE than that in KFSI electrolyte. After the addition of FEC (Figure 6.5), the GeP_5 electrode also exhibited a similar large irreversible capacity in the initial discharge process. This is probably due to greater reduction of the electrolyte to form the SEI, or the excess fluoride may have reacted with the electrode

or the potassium metal in the KPF_6 electrolyte[40]. To further demonstrate the possible side reactions, the CEs of the GeP_5 electrodes in various electrolytes are presented in Figure 6.6. In the following cycles, the CE for KFSI electrolyte stabilized at around 98.5%, but the CE in KPF_6 electrolyte was maintained at ~95% after 50 cycles. With the FEC additive, the CE of the GeP_5 electrodes was below 85%. These results further suggest that the excess side reactions may have occurred due to the high fluoride concentration in the electrolyte, which may stimulate side reactions during the potassiation process.

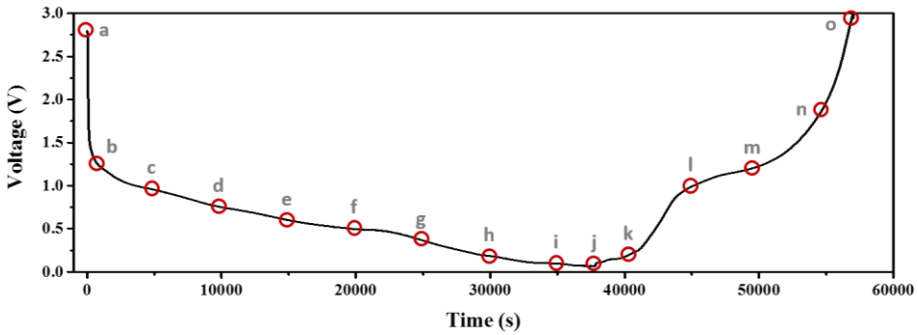

Figure 6.7. The first lithiation/de-lithiation process in GeP_5 electrode.

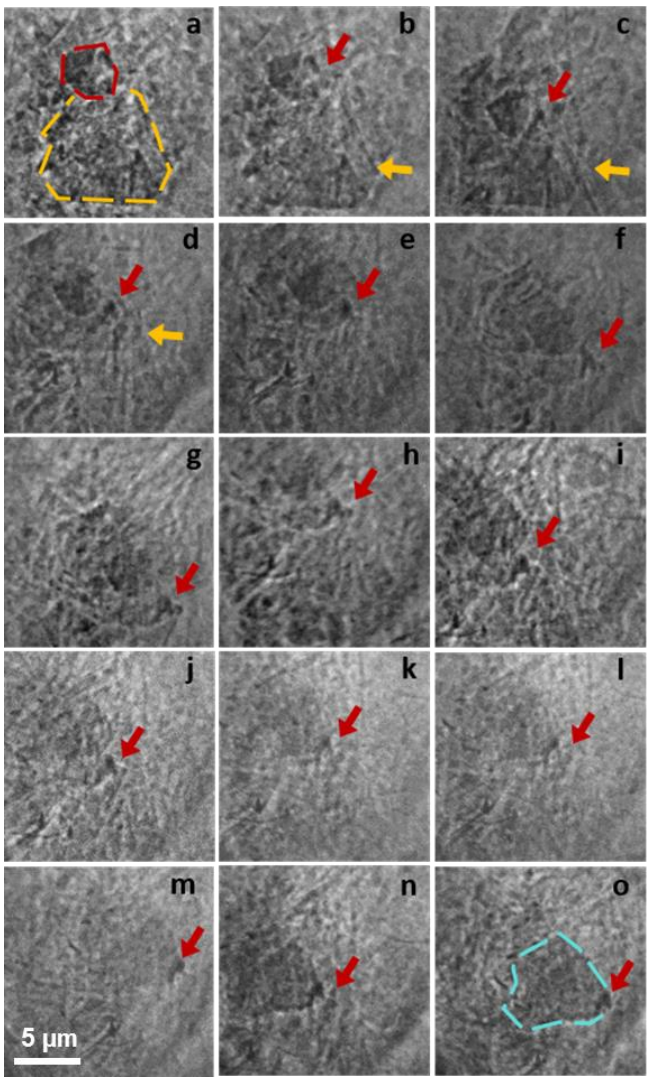

Figure 6.8. TXM micrographs of selected particles. (a-o is corresponding to the relevant points in Figure 6.7)

In-operando transmission X-ray microscopy (TXM) measurements of the GeP_5 used as anode in LIBs were also carried out to reveal the morphological changes induced by the Li storage reactions during cycling. It can be observed that, during lithiation and delithiation processes (Figure 6.7), the GeP_5 particle undergoes a similar two-stage mechanism[31], with this leading to partial particle pulverisation (Figure 6.8). It can be imagined that more severe pulverisation and irreversible volume variations

will occur when the GeP_5 is reacting with K, which has a much larger ionic radius (1.38 Å for K^+ vs. 0.76 Å for Li^+). In order to achieve stable cyclability of the electrodes, besides employing KFSI salt to regulate the formation of the SEI layer, a conductive matrix or void space (porous structure) must be introduced to buffer the mechanical stress induced by the vigorous volume variation of GeP_5 during potassiation/depotassiation in order to avoid pulverisation and maintain the integrity of the electrode,. Herein, ball-milled GeP_5 with carbon black were mixed, and long-term cycling was conducted at a current density of 500 mA g^{-1} with suitable amounts of carbon (Figure 6.2D). After activation during the initial cycle at a current density of 50 mA g^{-1}, the GeP_5 electrode in KFSI electrolyte exhibited superior stable cycling performance and still maintained 213.7 mA h g^{-1} after 2000 cycles. In KPF_6 electrolyte, however, the capacity was relatively stable in the first 220 cycles, but it showed severe fluctuations afterwards. Figure 6.9 presents representative time-voltage profiles corresponding to certain cycles. The GeP_5 electrode in KPF_6 electrolyte maintained a stable round-trip performance up to 220 cycles. Afterwards, the voltage fluctuated and required a relatively longer time than normal discharge/charge time intervals. To understand the problem and to optimize the performance of the battery, the cells were cycled in KPF_6 electrolyte in different voltage ranges with low cut-off potentials of 0.1 V and 0.2 V, respectively. As can be observed in Figure 6.10, the electrode suffered from capacity fluctuations after around 600 cycles in the voltage range of 0.1-3 V. In contrast, by slightly increasing the low voltage cut-off to 0.2 V,

excellent cycling performance could be obtained, even after 1500 cycles, but there is a sacrifice, relatively low specific capacity due to the higher cut-off potential. It can be observed that the voltage fluctuated and was retained for a relatively longer time than normal discharge/charge time intervals for the cells in KPF_6 electrolyte between 360-380 cycles within the voltage range of 0.1-3 V (Figure 6.11). These results suggest that the cycling performance of the electrode can be improved by either using a higher cut-off voltage or employing a suitable electrolyte.

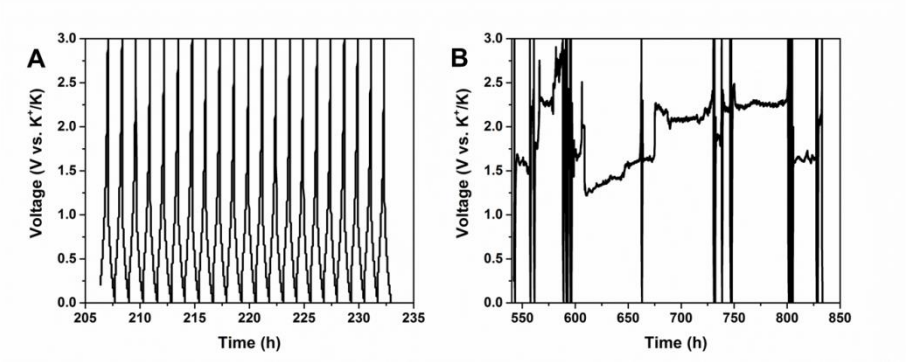

Figure 6.9. Time-voltage profiles of the electrode in KPF_6 electrolyte between a) 50-70 and b) 250-270 cycles within the voltage range of 0.01-3 V.

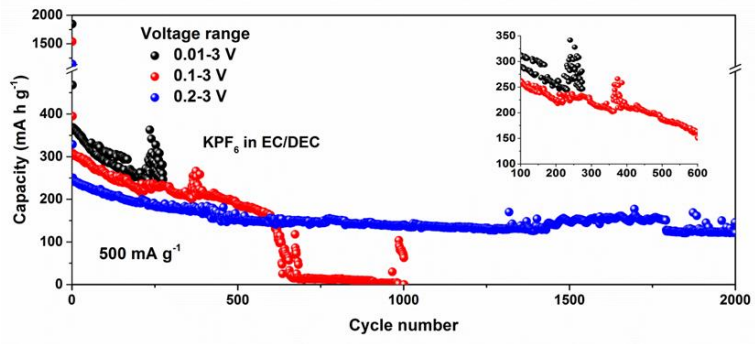

Figure 6.10. Long-term cycling tests of the cells in various voltage ranges at 500 mA g^{-1} in KPF_6 electrolyte, with the inset showing an enlargement of the indicated range.

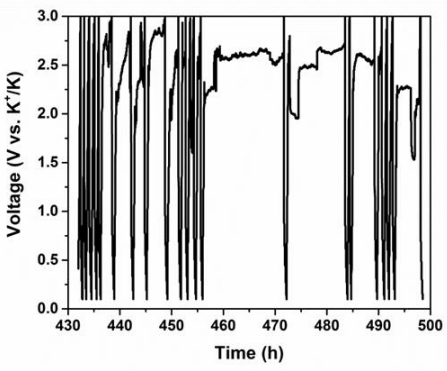

Figure 6.11. Time-voltage profiles of the cells in KPF_6 electrolyte between 360-380 cycles within the voltage range of 0.1-3 V.

Uniformity and thickness of SEI layer in various electrolytes

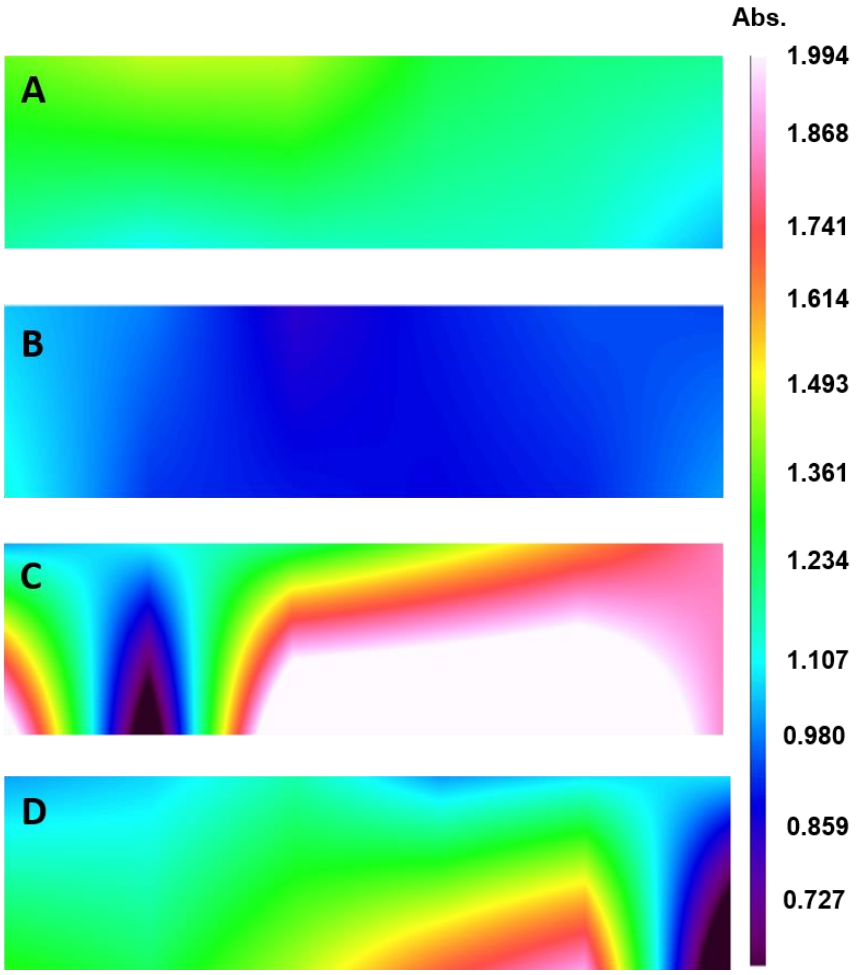

Figure 6.12. FTIR mapping of the surfaces of the cycled electrodes. In electrolytes consisting of (A) KPF_6-EC/DEC, (B) KFSI-EC/DEC, (C) KPF_6-EC/DEC with FEC, and (D) KFSI-EC/DEC with FEC. (Absorbance (Abs.) ranges were limited from 0.6 to 2.0, with the colour scale based on the corrected absorbance adjusted to the same range.)

Fourier transform infrared (FTIR) spectroscopic mapping was carried out to study the side reactions and distributions of the SEI layer formed in various electrolytes during cycling. The FTIR images were mapped from a set area on the surface of the fresh electrode and the electrode after the 1st cycle, as shown in Figure 6.12. The FTIR mapping of the pristine electrode surface is shown in Figure 6.13. The GeP_5 electrodes in KPF_6 and KFSI electrolyte all exhibited brighter colours (higher Abs. values) than the pristine electrodes, which indicates that the SEI layer could be effectively formed on the surface of the electrode after the 1st cycle. To compare these images, the colour scale based on the corrected absorbance has been adjusted to the same ranges from 0.6 to 2.0. By the semi-quantitative method, areas of contrast can be used to identify the homogeneity and thickness of the SEI layers on the surfaces of the electrodes, with areas of high and low amounts of the imaged chemical entity colour coded as white and black, respectively. As shown in Figure 6.12A and 6.12B, green and blue colour distributions are visible on the surfaces of the electrodes, indicating that uniform SEI layers formed during cycling in KPF_6 and KFSI electrolytes.

Additionally, the blue colour contrast in KFSI electrolyte suggests that a thinner SEI layer was formed than in the KPF_6 electrolyte. To further enhance the image contrast to compare the SEI layers formed in KPF_6 and KFSI electrolytes, the detailed colour scale was limited to the range from 0.9 to 1.5 (Figure 6.14). The colour mapping reveals that the SEI layer in KFSI electrolyte is more homogeneous than that in KPF_6 electrolyte. With the addition of FEC to the electrolytes (Figure 6.12C and 6.12D), the non-uniform colour distributions with white and red contrast reveal the formation of thick and inhomogeneous SEI layers on the surfaces of electrodes in electrolytes with FEC.

These results suggest that KFSI as an alternative potassium salt in carbonate electrolytes can effectively help to generate an even and stable SEI layer and possibly avoid excessive side-reactions, resulting in an improved CE, as shown in Figure 6.6. In contrast, KPF_6 and FEC additive will stimulate the formation of a relatively thick and uneven SEI layer, leading to low CE and poor cycling performance of the electrodes. Hence, it is proposed that the KFSI electrolyte is beneficial for constructing a uniform and stable SEI film, thus enhancing the cycling stability of the electrodes for PIBs.

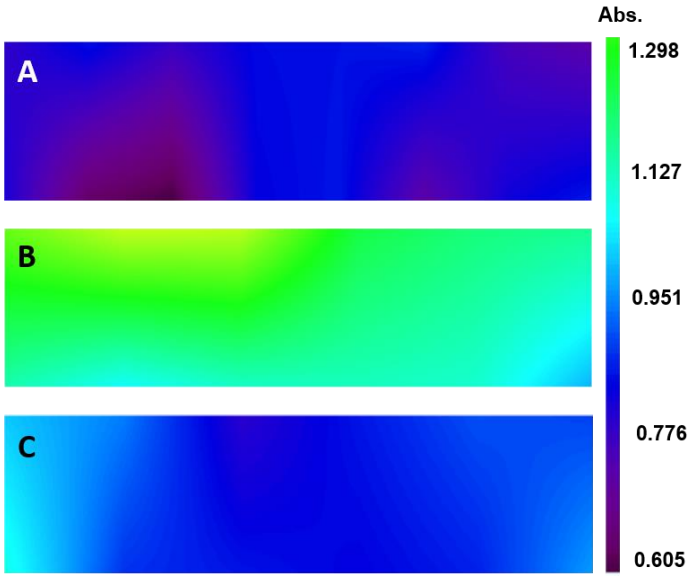

Figure 6.13. FTIR mapping images of the selected areas on the surfaces of the electrodes: (A) pristine electrode, (B) KPF_6 with EC/DEC electrolyte, and (C) KFSI with EC/DEC electrolyte. (Absorbance (Abs.) ranges were limited to the range from 0.6 to 1.3, with the colour scale based on the corrected absorbance adjusted to the same range.)

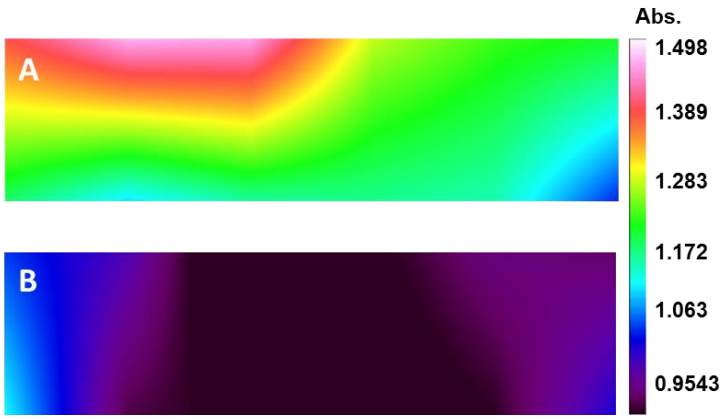

Figure 6.14. FTIR mapping images of the selected areas on the surfaces of the electrodes: (A) KPF_6 with EC/DEC electrolyte, and (B) KFSI with EC/DEC

electrolyte. (Absorbance (Abs.) ranges were limited to the range from 0.9 to 1.5, with the colour scale based on the corrected absorbance adjusted to the same range.)

In-operando XRD mechanistic study of GeP_5 as anode for PIBs

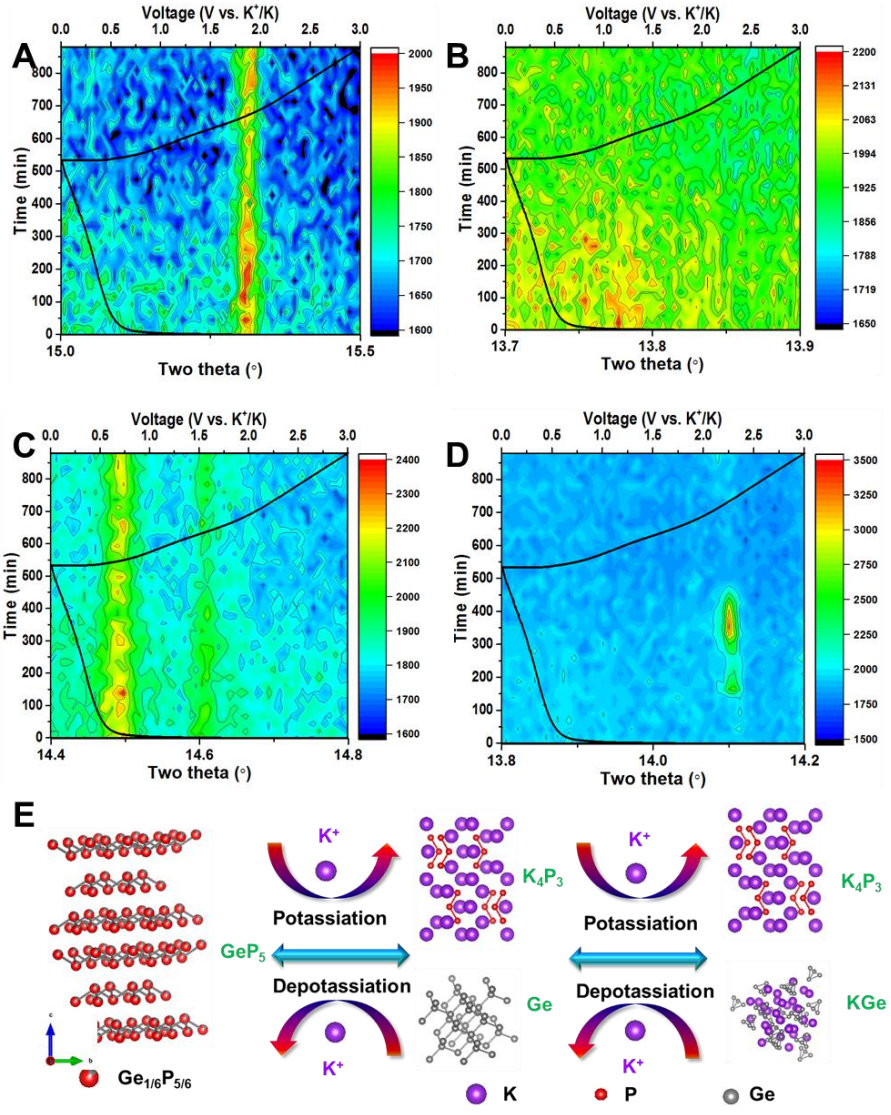

Figure 6.15. Electrochemical reaction mechanistic study of GeP_5 as anode for PIBs. (A to D) Contour plots of *in-operando* synchrotron X-ray powder diffraction with superimposed voltage profiles shown for selected 2θ ranges of GeP_5 as anode for

PIBs: (A) GeP_5 (012), (B) K_4P_3 (114), (C) Ge (201), (D) KGe (215), and (E) schematic illustration of the potassiation/depotassiation process in GeP_5 electrode.

To understand the electrochemical reaction mechanism of GeP_5 as anode for PIBs, the mechanistic response of GeP_5 anode during cycling within a potential window of 0.01 – 3.0 V (vs. K^+/K) was characterised using *in-operando* synchrotron XRD (λ = 0.68899 Å). The measurements were carried out at the Powder Diffraction Beamline, Australian Synchrotron. The *in-operando* diffraction data for the GeP_5 cell in the first cycle are represented by the contour plots of the *operando* data in selected 2θ ranges in Figure 6.15A-D. The intensity of the GeP_5 (012) reflection at $2\theta = 15.31^\circ$ decreased with the discharge process down to 0.01 V and afterwards increased with the charge process (Figure 6.15A), which indicates the consumption of GeP_5 phase during discharging (potassiation) and its reversibility during charging (depotassiation). The insufficient reaction of GeP_5 is possibly due to the relatively large current density and high loading amount for synchrotron experiments. In the initial discharge process, a peak for the K_4P_3 nanoparticle (114) reflection at $2\theta = 13.78^\circ$ (Figure 6.15B) appears, and its intensity increases. Upon further discharge, the intensity of the Ge reflection at $2\theta = 14.49^\circ$ (Figure 6.15C) increases to its maximum after discharging to ~0.45 V and then decreases. After further discharge, the peak for the KGe (04-007-1643) reflection at $2\theta = 14.07^\circ$ (Figure 6.15D) appears at around 0.4 V and remains until full discharge.

According to these results, it can be concluded that the potassiation process for GeP_5 could be divided into two stages and described by the following equations:

$$GeP_5 + \frac{20}{3}K \leftrightarrow \frac{5}{3}K_4P_3 + Ge \quad (I)$$

$$Ge + K \leftrightarrow KGe \quad (II)$$

The reaction mechanism for GeP_5 during potassiation/depotassiation is schematically shown in Figure 6.15E. In stage I, a conversion reaction occurs, GeP_5 decomposes into Ge and P particles, and the P component reacts with K to form K_4P_3. In stage II, Ge alloys with K to form KGe. Consequently, the synergistic K-storage reactions of K-P phases (K_4P_3) and K-Ge (KGe) alloys during the discharge process can create a mutual buffer mechanism. This buffering effect can alleviate the volume changes during cycling, thus helping to maintain the integrity of the electrode and improve the cycling stability.

.

6.4. Conclusion

In summary, a layered alloy compound, GeP_5, with high phosphorus concentration was reported as anode material for PIBs. The GeP_5 electrode can deliver a high reversible specific capacity over 500 mA h g^{-1} and exhibits excellent rate capability (230 mA h g^{-1} at 1 A g^{-1}) for K ion storage. The superior electrochemical performance is attributable to the synergistic reaction mechanism (alloying and conversion reactions) during the discharge/charge processes, which greatly buffers volume

changes in the electrode. An alternative potassium salt (KFSI) has been demonstrated to promote a uniform, stable SEI layer and allow long cyclability for PIBs. This work suggests the great potential of GeP_5 as anode for PIBs and is likely to attract more interest in exploring alloy-based electrode materials with high volumetric capacity in electrochemical energy storage.

6.5. References

[1] D. Larcher, J.-M. Tarascon, *Nature chemistry* **2015**, 7, 19.

[2] B. Kang, G. Ceder, *Nature* **2009**, 458, 190.

[3] C. Chen, Z. Wang, B. Zhang, L. Miao, J. Cai, L. Peng, Y. Huang, J. Jiang, Y. Huang, L. Zhang, J. Xie, *Energy Storage Materials* **2017**, 8, 161.

[4] A. S. Arico, P. Bruce, B. Scrosati, J.-M. Tarascon, W. Van Schalkwijk, *Nature materials* **2005**, 4, 366.

[5] M. Li, J. Lu, Z. Chen, K. Amine, *Advanced Materials* **2018**, 1800561.

[6] C. Hu, X. Chen, Q. Dai, M. Wang, L. Qu, L. Dai, *Nano Energy* **2017**, 41, 367.

[7] C. Hu, L. Dai, *Advanced Materials* **2017**, 29, 1604942.

[8] H. B. Wu, X. W. D. Lou, *Science Advances* **2017**, 3, eaap9252.

[9] J. B. Goodenough, K.-S. Park, *J. Am. Chem. Soc.* **2013**, 135, 1167.

[10] J. Xie, L. Liao, Y. Gong, Y. Li, F. Shi, A. Pei, J. Sun, R. Zhang, B. Kong, R. Subbaraman, *Science advances* **2017**, 3, eaao3170.

[11] Y. Wang, R. Zhang, Y.-c. Pang, X. Chen, J. Lang, J. Xu, C. Xiao, H. Li, K. Xi, S. Ding, *Energy Storage Materials* **2019**, 16, 228.

[12] Y. Liu, X.-Y. Yu, Y. Fang, X. Zhu, J. Bao, X. Zhou, X. W. D. Lou, *Joule* **2018**, 2, 725.

[13] I. Sultana, M. M. Rahman, Y. Chen, A. M. Glushenkov, *Advanced Functional Materials* **2017**, 28, 1703857.

[14] A. Eftekhari, Z. Jian, X. Ji, *ACS Appl. Mater. Interfaces* **2016**, 9, 4404.

[15] P.-F. Wang, H.-R. Yao, X.-Y. Liu, Y.-X. Yin, J.-N. Zhang, Y. Wen, X. Yu, L. Gu, Y.-G. Guo, *Science advances* **2018**, 4, eaar6018.

[16] N. Yabuuchi, K. Kubota, M. Dahbi, S. Komaba, *Chem. Rev.* **2014**, 114, 11636.

[17] M. D. Slater, D. Kim, E. Lee, C. S. Johnson, *Adv. Funct. Mater.* **2013**, 23, 947.

[18] Z. Jian, W. Luo, X. Ji, *J. Am. Chem. Soc.* **2015**, 137, 11566.

[19] K. Lei, C. Wang, L. Liu, Y. Luo, C. Mu, F. Li, J. Chen, *Angewandte Chemie* **2018**, 130, 4777.

[20] Q. Zhang, J. Mao, W. K. Pang, T. Zheng, V. Sencadas, Y. Chen, Y. Liu, Z. Guo, *Advanced Energy Materials* **2018**, 1703288.

[21] J. Zhao, X. Zou, Y. Zhu, Y. Xu, C. Wang, *Adv. Funct. Mater.* **2016**, 26, 8103.

[22] J. Yang, Z. Ju, Y. Jiang, Z. Xing, B. Xi, J. Feng, S. Xiong, *Advanced Materials* **2017**, 30, 1700104.

[23] C. Chen, Z. Wang, B. Zhang, L. Miao, J. Cai, L. Peng, Y. Huang, J. Jiang, Y. Huang, L. Zhang, *Energy Storage Materials* **2017**, 8, 161.

[24] W. Zhang, J. Mao, S. Li, Z. Chen, Z. Guo, *J. Am. Chem. Soc.* **2017**, 139, 3316.

[25] P. Lou, Z. Cui, Z. Jia, J. Sun, Y. Tan, X. Guo, *ACS nano* **2017**, 11, 3705.

[26] Y. Lu, P. Zhou, K. Lei, Q. Zhao, Z. Tao, J. Chen, *Advanced Energy Materials* **2017**, 7, 1601973.

[27] Y. Kim, Y. Kim, A. Choi, S. Woo, D. Mok, N. S. Choi, Y. S. Jung, J. H. Ryu, S. M. Oh, K. T. Lee, *Adv. Mater.* **2014**, 26, 4139.

[28] X. Fan, J. Mao, Y. Zhu, C. Luo, L. Suo, T. Gao, F. Han, S. C. Liou, C. Wang, *Advanced Energy Materials* **2015**, 5, 1500174.

[29] W. Zhang, J. Mao, W. K. Pang, Z. Guo, Z. Chen, *Electrochim. Acta* **2017**, 235, 107.

[30] J. Qian, Y. Xiong, Y. Cao, X. Ai, H. Yang, *Nano Lett.* **2014**, 14, 1865.

[31] W. Li, H. Li, Z. Lu, L. Gan, L. Ke, T. Zhai, H. Zhou, *Energy & Environmental Science* **2015**, 8, 3629.

[32] W. K. Pang, S. Kalluri, V. K. Peterson, N. Sharma, J. Kimpton, B. Johannessen, H. K. Liu, S. X. Dou, Z. Guo, *Chem. Mater.* **2015**, 27, 3150.

[33] P. Hohenberg, W. Kohn, *Physical review* **1964**, 136, B864.

[34] J. P. Perdew, K. Burke, M. Ernzerhof, *Phys. Rev. Lett.* **1996**, 77, 3865.

[35] B. Delley, *The Journal of chemical physics* **1991**, 94, 7245.

[36] H. J. Monkhorst, J. D. Pack, *Physical review B* **1976**, 13, 5188.

[37] K. Xu, A. von Cresce, U. Lee, *Langmuir* **2010**, 26, 11538.

[38] K. Xu, A. von Cresce, *Journal of Materials Chemistry* **2011**, 21, 9849.

[39] T. A. Pham, K. E. Kweon, A. Samanta, V. Lordi, J. E. Pask, *The Journal of Physical Chemistry C* **2017**, 121, 21913.

[40] N. Xiao, W. D. McCulloch, Y. Wu, *J. Am. Chem. Soc.* **2017**, 139, 9475.

[41] W. Zhang, W. K. Pang, V. Sencadas, Z. Guo, *Joule* **2018**, 2, 1534.

[42] J. Qian, X. Wu, Y. Cao, X. Ai, H. Yang, *Angew. Chem.* **2013**, 125, 4731.

[43] Y. Kim, Y. Park, A. Choi, N. S. Choi, J. Kim, J. Lee, J. H. Ryu, S. M. Oh, K. T. Lee, *Adv. Mater.* **2013**, 25, 3045.

[44] L. Zhou, M. Zhang, Y. Wang, Y. Zhu, L. Fu, X. Liu, Y. Wu, W. Huang, *Electrochimica Acta* **2017**, 232, 106.

[45] Q. Wang, W. Zhang, C. Guo, Y. Liu, C. Wang, Z. Guo, *Adv. Funct. Mater.* **2017**, 27, 1703390.

[46] W. Zhang, J. Mao, W. K. Pang, X. Wang, Z. Guo, *Nano Energy* **2018**, 49, 549.

[47] Z. Tu, S. Choudhury, M. J. Zachman, S. Wei, K. Zhang, L. F. Kourkoutis, L. A. Archer, *Joule* **2017**, 1, 394.

Chapter 7

7. General Conclusions and Outlook

7.1. General Conclusions

In this doctoral thesis work, recent advanced developments in electrode materials, especially carbon-based and alloy-based anode materials, were summarized. In addition, electrolyte engineering for improving the electrochemical performance of PIBs was introduced.

This doctoral thesis included three works related to phosphorus-based anode for PIBs. In the first work, Sn_4P_3/C composite was synthesized by a simple ball-milling method and was used as anode for PIBs for the first time. Although the cycling performance was not satisfactory, the obtained specific capacity was the highest among reported anodes to date. In addition, Sn_4P_3/C anode in PIBs could deliver a discharge voltage plateau (0.1 V) that is low enough for an anode, but slightly higher than the plating potential of the corresponding metal (0.01 V), thus avoiding the formation of dendrites and improving the safety of the battery. The investigation of the reaction mechanisms of the Sn_4P_3 indicates that K-Sn (K_4Sn_{23}, KSn) and K-P alloy ($K_{3-x}P$) phases are formed during the discharge process, with these phases acting as mutual buffers to alleviate the volume changes during cycling. The conductive carbon matrix enhances the electrical conductivity of the electrode and works as a buffer matrix to accommodate the volume changes in the active materials during cycling, maintaining the integrity of the electrode and the cycle life.

In the second work, Sn_4P_3 as a promising high capacity electrode material for PIBs

was synthesized through a scalable ball-milling method and further modified by confining the as-milled particles in carbon fibre through the electrospinning technique. This design not only offers a feasible avenue for the large-scale fabrication of phosphorus-based electrode materials with a relatively simple synthesis strategy, but also takes advantage of the one-dimensional carbon fibre, addressing the volume expansion problem to improve electrochemical performance. *In-operando* synchrotron XRD studies were first carried out to reveal the electrochemical reaction mechanism of Sn_4P_3 as anode for PIBs. The investigations suggest that K-P (K_3P_{11} and K_3P) and K-Sn (KSn) phases are formed during the discharge process, with these phases acting as mutual buffers to alleviate the volume changes during cycling. The effects of an alternative potassium salt (KFSI) and FEC additive in the electrolyte for PIBs were also investigated. A stable SEI layer is crucial for enhancing the cycling performance of batteries, and FEC has been demonstrated to improve the electrochemical performance of SIBs. In this work, however, FEC stimulates excessive side reactions and accelerates the consumption of the electrolyte, resulting in uneven SEI layer formation and electron distribution, which boost the potassium dendrite growth. Therefore, it greatly increases the polarization and slows down the reaction dynamics during cycling of PIBs. In contrast, KFSI plays a critical role in suppressing the growth of potassium dendrites and reducing the effects of polarization, so it can effectively generate a uniform SEI layer and allow stable cyclability at high current density.

In the third work, a layered alloy compound, GeP_5, with a high phosphorus concentration was reported as anode material for PIBs. The GeP_5 electrode can deliver a high reversible specific capacity over 500 mA h g^{-1} and exhibits excellent

rate capability (230 mA h g^{-1} at 1 A g^{-1}) for K ion storage. The superior electrochemical performance is attributable to the synergistic reaction mechanism (alloying and conversion reactions) during the discharge/charge processes, which greatly buffers volume changes in the electrode. An alternative potassium salt (KFSI) has been demonstrated to promote a uniform, stable SEI layer and allow long cyclability for PIBs.

As a general conclusion, Sn_4P_3 and GeP_5 anode materials were investigated, and it was found that they could be used as potential high-energy-density and high-volumetric-capacity electrodes for future practical applications. The use of a carbon matrix was demonstrated to be an effective strategy to improve the electrical conductivity and buffer the volume variations during cycling. In addition, electrolyte engineering by introducing the alternative KFSI salt was also evidenced by various advanced characterization techniques to be effective for enhancing the cycling stability and suppressing the growth of potassium dendrites.

7.2. Outlook

The research on phosphorus-based anode materials for PIBs is still in its infancy at this stage, so there is still plenty of room for future commercial applications.

Most importantly, from the aspect of electrode materials, the preparation methods might not be limited to the ball-milling methods. Although ball-milling methods are the most facile way to produce scalable nanosized materials, agglomeration could still be the main obstacle to long-term cyclability. In the future, the extended large-

scale preparation methods should be involved. For instance, electrospinning in this work has demonstrated its efficiency for enhancing the electrochemical performance. Hence, it is meaningful to use the electrospinning method to directly produce uniform phosphide particles. Solid-phase methods deserve attention because they can produce scalable phosphides with relatively uniform morphology. Therefore, it is necessary to study how to avoid or reduce the production of white phosphorus during the high-temperature procedure. Secondly, using a carbon matrix was demonstrated to be an effective strategy to enhance the electrical conductivity and accommodate the volume variations. How to involve a suitable carbon matrix and what sort of carbon could be introduced are the main problems for the next stage of research. Synergistic effects are also necessary to improve the cycling performance. In this doctoral work, Sn and Ge were successfully alloyed with P to form binary compounds. Therefore, it is promising to involve other metallic components and extend these to ternary alloy compounds to enhance the synergistic effects, thus improving the electrochemical performance.

In addition to considering electrode materials, more attention should be paid to electrolyte optimization. Based on the successful case of the introduction of alternative KFSI salt in this doctoral work, it would be promising to introduce other potassium salts to help form uniform SEI layers. Alternative potassium salts with low-fluoride content may be worth developing for use in PIB systems. Although FEC additive may be incompatible with the construction of stable and thin SEI layers to facilitate ion transportation, other additives could be adopted and deeply studied in order to improve the coulombic efficiency and enhance the reaction kinetics.

To meet the requirements of future commercial applications, full cells should be

taken into consideration in terms of suitable matched cathode materials. There have been very few reports to date where researchers tried to match cathodes with the phosphorus-based anode materials to study the full-cell performance of PIBs. Hence, it is necessary to start the relevant research to explore the energy density, cycling stability, and rate capability of phosphorus-based anodes used in PIBs.

Finally, owing to the staggering developments in advanced characterization tools such as *in-operando* XRD, in-situ Raman spectrometers, in-situ TEM, and other related equipment, detailed structural information and reaction mechanisms could be easily observed and analyzed to strengthen and deepen the understanding of the electrode materials themselves and their reaction kinetics. DFT calculations could also provide a deeper understanding of the electronic structure and molecular level. Combining the above fundamental analysis results would certainly help us to design the best electrode materials and optimize the electrolyte and cell architectures, thus accelerating the steps towards future commercialization of PIBs for energy storage devices.

Appendix A: Publications

1. **Wenchao Zhang**, Yajie Liu, Zaiping Guo. "Approaching high-performance potassium-ion batteries via advanced design strategies and engineering." ***Science Advances*** (Accepted, In press).
2. **Wenchao Zhang**, Wei Kong Pang, Vitor Sencadas, and Zaiping Guo. "Understanding High-Energy-Density Sn_4P_3 Anodes for Potassium-Ion Batteries." ***Joule*** 2(8), (2018): 1534-1547.
3. **Wenchao Zhang**, Zhibin Wu, Jian Zhang, Guoping Liu, Nai-Hsuan Yang, Ru-Shi Liu, Wei Kong Pang, Wenwu Li, and Zaiping Guo. "Unraveling the effect of salt chemistry on long-durability high-phosphorus-concentration anode for potassium ion batteries." ***Nano Energy*** 53 (2018): 967-974.
4. **Wenchao Zhang**, Jianfeng Mao, Wei Kong Pang, Xing Wang, and Zaiping Guo. "Creating fast ion conducting composites via in-situ introduction of titanium as oxygen getter." ***Nano Energy*** 49 (2018): 549-554.
5. **Wenchao Zhang**, Jianfeng Mao, Sean Li, Zhixin Chen, and Zaiping Guo. "Phosphorus-Based Alloy Materials for Advanced Potassium-Ion Battery Anode." ***Journal of the American Chemical Society*** 139, (2017): 3316-3319.
6. **Wenchao Zhang**, Jianfeng Mao, Wei Kong Pang, Zaiping Guo, and Zhixin Chen. "Large-scale synthesis of ternary Sn_5SbP_3/C composite by ball milling for superior stable sodium-ion battery anode." ***Electrochimica Acta*** 235 (2017): 107-113.
7. Qinghong Wang*, **Wenchao Zhang*(Co-First)**, Can Guo, Yajie Liu, Chao Wang, and Zaiping Guo. "In Situ Construction of 3D Interconnected FeS@

Fe3C@ Graphitic Carbon Networks for High‐Performance Sodium‐Ion Batteries." ***Advanced Functional Materials*** 27.41 (2017): 1703390.

8. Hongqiang Wang, **Wenchao Zhang**, Huakun Liu, and Zaiping Guo. "A Strategy for Configuration of an Integrated Flexible Sulfur Cathode for High‐Performance Lithium–Sulfur Batteries." ***Angewandte Chemie International Edition*** 55(12) (2016): 3992-3996.
9. Hongqiang Wang, **Wenchao Zhang**, Jianzhong Xu, and Zaiping Guo. "Advances in Polar Materials for Lithium–Sulfur Batteries." ***Advanced Functional Materials*** (2018): 1707520.
10. Qinghong Wang, Jiantie Xu, **Wenchao Zhang**, Minglei Mao, Zengxi Wei, Lei Wang, Chunyu Cui, Yuxuan Zhu, and Jianmin Ma. "Research progress on vanadium-based cathode materials for sodium ion batteries." ***Journal of Materials Chemistry A*** 6, no. 19 (2018): 8815-8838.
11. Jing Chen, Anqiang Pan, Yaping Wang, Xinxin Cao, **Wenchao Zhang**, Xiangzhong Kong, Qiong Su, Jiande Lin, Guozhong Cao, and Shuquan Liang. "Hierarchical Mesoporous $MoSe_2$@ CoSe/N-doped Carbon Nanocomposite for Sodium Ion Batteries and Hydrogen Evolution Reaction Applications." ***Energy Storage Materials*** (2018).
12. Junnan Hao, Jian Zhang, Guanglin Xia, Yajie Liu, Yang Zheng, **Wenchao Zhang**, Yongbing Tang, Wei Kong Pang, and Zaiping Guo. "Heterostructure Manipulation via In-Situ Localized Phase Transformation for High-Rate and Highly Durable Lithium Ion Storage." ***ACS Nano*** 12.10 (2018): 10430-10438.
13. Dan Li, Hongqiang Wang, Tengfei Zhou, **Wenchao Zhang**, Hua Kun Liu, and Zaiping Guo. "Unique Structural Design and Strategies for Germanium‐Based

Anode Materials Toward Enhanced Lithium Storage." ***Advanced Energy Materials*** 7.23 (2017): 1700488.

Appendix B: Conferences & Activities

1. 257th ACS National Meeting and Exposition, Orlando, USA, Apr. 1st to 4th, 2019.
2. The third Energy Future (EF3) Conference, Sydney, Australia, Feb. 5th to 7th, 2018
3. International Conference on Nanoscience and Nanotechnology**,** Wollongong, Australia, Jan. 29th to Feb. 2nd, 2018
4. The 2016 International Symposium on Next-Generation Batteries, North Wollongong, Australia, Aug. 9th to 12th, 2016.

Appendix C: Scholarships & Awards

1. 2015 International Postgraduate Tuition Award.
2. 2015 Matching Scholarship.
3. 2017 Postgraduate Student Best Paper Award, 03/2017
4. 2018 Chinese Government Private Excellent Scholarship award